TECHNISCHE UNIVERSITÄT
BERGAKADEMIE FREIBERG
The University of Resources. Since 1765.

Numerical study of a continuous casting process with electromagnetic brake

By the Faculty of Mechanical, Process and Energy Engineering
of the Technische Universität Bergakademie Freiberg

approved

Thesis

to attain the academic degree of

Doktor-Ingenieur
(Dr.-Ing.)

submitted by **M. Sc. Xincheng Miao**

born on the 11. August 1971 in Liaoning P.R.China

Assessor: Prof. Dr.-Ing. Rüdiger Schwarze
Prof. Dr.-Ing. Egbert Baake

Date of the award:Freiberg, 28th May 2014

Versicherung

Hiermit versichere ich, dass ich die vorliegende Arbeit ohne unzulässige Hilfe Dritter und ohne Benutzung anderer als der angegebenen Hilfsmittel angefertigt habe; die aus fremden Quellen direkt oder indirekt übernommenen Gedanken sind als solche kenntlich gemacht.

Bei der Auswahl und Auswertung des Materials sowie bei der Herstellung des Manuskripts habe ich Unterstützungsleistungen von folgenden Personen erhalten:

- K.Timmel and C.Zhang (Experimental)
- S.Eckert, D.Lucas, R.Schwarze and G.Gerbeth(Literature)

Weitere Personen waren an der Abfassung der vorliegenden Arbeit nicht beteiligt.

Die Hilfe eines Promotionsberaters habe ich nicht in Anspruch genommen. Weitere Personen haben von mir keine geldwerten Leistungen für Arbeiten erhalten, die nicht als solche kenntlich gemacht worden sind. Die Arbeit wurde bisher weder im Inland noch im Ausland in gleicher oder ähnlicher Form einer anderen Prüfungsbehörde vorgelegt.

M. Sc. Xincheng Miao

Declaration

I hereby declare that I completed this work without any improper help from a third party and without using any aids other than those cited. All ideas derived directly or indirectly from other sources are identified as such.

In the selection and use of materials and in the writing of the manuscript I received support from the following persons:

- K.Timmel and C.Zhang (Experimental)
- S.Eckert, D.Lucas, R.Schwarze and G.Gerbeth(Literature)

Persons other than those above did not contribute to the writing of this thesis.

I did not seek the help of a professional doctorate-consultant. Only those persons identified as having done so received any financial payment from me for any work done for me. This thesis has not previously been published in the same or a similar form in Germany or abroad.

28th May 2014 M. Sc. Xincheng Miao

Acknowledgments

This work was conducted at the Magnetohydrodynamic Division in Helmholtz-Zentrum Dresden-Rossendorf. First and foremost, I am deeply indebted to my PhD advisor Dr. Gunter Gerbeth offering me the chance to study in the leading research group. With his consistent support and guidance, it makes my work possible. I am very grateful for his patience, motivation, enthusiasm, and immense knowledge in MHD that, taken together, make him a great mentor.

I will be specially thankful to Dr. Sven Eckert who has been helpful in providing advice from science to scientific writings. He is always happy to have a discussions whenever I turned to him for help.

I would like to thank my advisors Prof. Rüdiger Schwarze for providing me with the opportunity to complete my PhD thesis at the Technische Universität Bergakademie Freiberg as an external student at the Helmholtz-Zentrum Dresden-Rossendorf.

Then I want to express my appreciation to Dr. Dirk Lucas who alway guides me in numerical modeling. I learned many knowledge from him, in particular, the theory of two-phase flow.

I would like to acknowledge my colleague, Mr. Klaus Timmel, who is responsible for the experiment in the project. He always kindly provides measuring data whenever I want to know.

Special thanks will be given to Prof. Zhongming Ren of Shanghai University, P.R. China, who introduced me to Helmholtz-Zemtrum Dresden-Rossendorf. Meanwhile, I would like to take this opportunity to express my gratitude to Dr. Eckhard Krepper, Dr. Viktoriya Shatrova and all of my colleagues

I am very grateful to Deutsche Forschungsgemeinschaft (DFG) for funding my research in frame of the SFB 609 “Electromagnetic Flow Control in Metallurgy, Crystal Growth and Electrochemistry”.

Finally, a great acknowledgment to my wife, Yang Song, for her understanding and support, and my son, Yuntong Miao.

Abstract

This dissertation investigates the effect of electromagnetic braking and gas injection on the fluid flow in a continuous casting slab mold numerically and makes verifications on basis of a small Liquid Metal Model for Continuous Casting of steel (mini-LIMMCAST). Numerical calculations were performed by means of the software package CFX with an implemented RANS-SST turbulence model. The non-isotropic nature of the MHD turbulence was taken into account by specific modifications of the turbulence model. The numerical results were validated by flow measurements at the mini-LIMMCAST facility. Numerical simulations disclose the damping effect on the flow closely depending on the wall conductance ratio. In addition, specific modifications of the turbulence model play a crucial role in reconstructing the peculiar phenomenon of an excitation of nonsteady, nonisotropic, large-scale flow perturbations caused by the application of the DC magnetic field.

Chapter 1 consists of four parts: research objectives; motivation for the thesis; literature review; a short introduction to the research background; a brief view of magnetohydrodynamic fundamentals; as well as description of experimental setup.

Chapter 2 gives a description of the mathematical modelling. By virtue of the introduction to turbulence models, RANS-SST turbulence model is chosen in present work. Considering the influence of magnetic field on the turbulence, a specific modification of the magnetic field on turbulence model is addressed.

Chapter 3 introduces the choice of mathematical models and the implementation of a specific modification of the magnetic field influence on the turbulence model in CFX, and then making two tests for this MHD model.

Chapter 4 is focused on the effect of an electromagnetic brake on the turbulent melt flow in a continuous casting mold. The comparison between our numerical calculations and the experimental results displays a good agreement; in particular, the peculiar phenomenon of an excitation of nonsteady, nonisotropic, large-scale flow perturbations caused by the application of the DC magnetic field is reconstructed successfully. Another important result of our study is the feature that the electrical boundary conditions, namely the wall conductivity ratio, have a serious influence on the mold flow while it is exposed to an external magnetic field.

Chapter 5 is concentrated on the investigation of bubble-driven liquid metal flows with external static magnetic field and the mathematical model verification. The calculations are able to reproduce a striking feature of a horizontal magnetic field found in the range of moderate Hartmann numbers revealing that such a steady transverse magnetic field may destabilize the flow and cause distinct oscillations of the liquid velocity.

Chapter 6 addresses the study of flow field in a slab mold with the applications of magnetic field and gas injection. An Euler-Euler approach has been employed to investigate the effects of argon gas and static magnetic field on the flow pattern in a slab mold.

Chapter 7 summaries and draws some main conclusions from current work.

Contents

Nomenclature **IX**

List of Figures **XIII**

List of Tables **XVII**

1 Introduction **1**
- 1.1 Research Objectives 1
- 1.2 Motivation for the thesis 1
- 1.3 Literature review 6
  - 1.3.1 EMBr effect in a single-phase continuous casting process 6
  - 1.3.2 Bubbly flow with an external magnetic field 6
  - 1.3.3 Effect of EMBr and gas injection in a continuous casting process . . . 8
- 1.4 Research Background 8
- 1.5 Some fundamentals of magnetohydrodynamics 10
- 1.6 Experimental Setup 11

2 State of the Art **15**
- 2.1 Governing equations Continuum Mechanics 15
- 2.2 Turbulence models 17
  - 2.2.1 Zero-equation turbulence model 17
  - 2.2.2 One-equation turbulence model 17
  - 2.2.3 Two-equation turbulence model 18
  - 2.2.4 Discussions and conclusions 20
- 2.3 Mathematical models for multiphase flow 21
  - 2.3.1 Basic equations 21
  - 2.3.2 Bubble-induced turbulence 22
  - 2.3.3 Drag force 23
  - 2.3.4 Lift force 24
  - 2.3.5 Other forces on bubbles 25
  - 2.3.6 MUSIG model 26
- 2.4 Modeling of near-wall turbulence 27
- 2.5 Modeling of magnetic field influence on turbulence 29

3 Implementation of mathematical models **33**
- 3.1 Finite Volume Method 33
- 3.2 Test of MHD model in CFX 36
- 3.3 Grid sensitivity 38
  - 3.3.1 Configuration of an MHD duct flow 38
  - 3.3.2 Results and discussion 38

4 Study of the modified turbulence model in a continuous casting slab liquid metal mold **41**
- 4.1 Computational conditions 41

4.2 Results 42
- 4.2.1 Comparison of the Time-Averaged Flow 42
- 4.2.2 Influence of Magnetic Field Intensity 48
- 4.2.3 Fluctuations of the Mold Flow 53
- 4.2.4 Influence of Wall Conductance Ratio 56

4.3 Summary and discussion 58

5 Study of a bubble-driven flow under the influence of a DC magnetic field 65

5.1 Computational domain and boundary conditions 65

5.2 Results 68
- 5.2.1 Bubbly flow without magnetic field 68
- 5.2.2 Bubbly flow with longitudinal magnetic field 70
- 5.2.3 Bubbly flow with transverse magnetic field 70

5.3 Summary and discussion 77

6 Two-phase flow in a continuous casting slab mold under influence of an external magnetic field 79

6.1 Computational domain and boundary conditions 79

6.2 Numerical Results 80
- 6.2.1 Mono-dispersed particle model 80
- 6.2.2 Poly-dispersed particle model 83
- 6.2.3 Poly-dispersed particle model for varying magnetic field strength . . . 92
- 6.2.4 Influence of the electrical wall conductance ratio 95

6.3 Discussion and summary 95

7 Summary 99

Bibliography 101

Nomenclature

α_G	Void fraction of gas phase
α_k	Void fraction of phase k
α_L	Void fraction of liquid metal
α_μ	Anisotropy parameter
δ	Non-dimensional Hartmann layer thickness
δ_W	Hartmann layer thickness, m
δ_{ij}	Kronecker delta
γ	Surface tension, N/m
κ	Karman constant, ~ 0.41
$\mathbf{B}$	Magnetic flux, T
$\mathbf{f}$	Body force, N
$\mathbf{F}_{D,L}$	Drag force of liquid metal, N
$\mathbf{F}_{I,G}$	Interfacial force of gas phase, N
$\mathbf{F}_{I,k}$	Interfacial force of phase k, N
$\mathbf{F}_{I,L}$	Interfacial force of liquid metal, N
$\mathbf{F}_{L,L}$	Lift force of liquid metal, N
$\mathbf{F}_{LUB,L}$	Wall lubrication force of liquid metal, N
$\mathbf{F}_{TD,L}$	Turbulent dispersion force of liquid metal, N
$\mathbf{F}_{VM,L}$	Virtual mass force of liquid metal, N
$\mathbf{J}$	Induced current density, A
$\mathbf{u}_G$	Velocity of gas phase, $m \cdot s^{-1}$
$\mathbf{u}_L$	Velocity of liquid metal, $m \cdot s^{-1}$
$\mathbf{v}$	Velocity, $m \cdot s^{-1}$
μ	Dynamic viscosity, $Pa \cdot s$
μ_t	Eddy viscosity, $Pa \cdot s$
μ_0	Magnetic permeability, $H \cdot m^{-1}$
μ_{BIT}	Bubble-induced viscosity, $Pa \cdot s$

ν	Kinematic viscosity, $m^2 \cdot s^{-1}$
ν_t	Turbulent kinematic viscosity, $m^2 \cdot s^{-1}$
Ω	Magnitude of vorticity rate, s^{-1}
ω	Specific dissipation rate, s^{-1}
Ω_{ij}	Vorticity tensor, s^{-1}
ρ	Density, $kg \cdot m^{-3}$
ρ_G	Density of gas phase, $kg \cdot m^{-3}$
ρ_L	Density of liquid metal, $kg \cdot m^{-3}$
σ	Electrical conductivity of liquid metal, $S \cdot m^{-1}$
σ_W	Electrical conductivity of wall, $S \cdot m^{-1}$
τ_{ij}	Deviatoric stress tensor, s^{-1}
ε	Turbulent dissipation, $m^2 \cdot s^{-3}$
φ	Electrical potential, V
$\vec{n}$	Unit vector normal to the boundary
$\widetilde{U}_i$	Instantaneous velocity of i-component, $m \cdot s^{-1}$
b	Boundary, subscript
C_W	Wall conductance ratio
Eo	*Eötvös* number
$F1, F2$	Blending functions
F_L	Electromagnetic force or Lorentz force, N
$F_{L,k}$	Electromagnetic force of phase k, N
Ha	Hartmann number
k	Turbulent kinetic energy, $m^2 \cdot s^{-2}$
L	Characteristic length scale, m
l_m	Mixing length, m
M_k	Phase indicator function
N	Magnetic interaction parameter
P	Production term
p	Pressure, Pa
P_k	Production term for turbulent kinetic energy
Re	Reynolds number

Re_m	Magnetic Reynolds number
S	Modulus of strain rate, s^{-1}
S_f	Outward face vector
S_{ij}	Strain rate, s^{-1}
$S_{t,\omega}$	Bubble-induced source term for ω equation
$S_{t,\varepsilon}$	Bubble-induced source term for ε equation
$S_{t,k}$	Bubble-induced source term for k equation
U_i	Time-averaged velocity of i-component, $m \cdot s^{-1}$
u_i	Fluctuating velocity of i-component, $m \cdot s^{-1}$
x, y, z	Spatial coordinates, m
x_i	i-component of Coordinates, m
x_j	j-component of Coordinates, m
x_k	k-component of Coordinates, m
f	face of control volume

List of Figures

1.1 Types of the imposed external static magnetic fields for a continuous casting slab mold (from ABB comany) 2
1.2 Distribution of electric currents in a rectangular duct flow with a homogeneous DC magnetic field (a homogeneous DC magnetic field, B, is applied in z direction; the fluid flow s in x axis with velocity U.) 4
1.3 A schematic of steel slab mold in a center-plane across the wide face (static DC magnetic field B is imposed perpendicular to the wide faces in a slab mold; liquid metal discharged from SEN into the liquid pool crossing B; the corresponding induced electric currents make closure in the mold) 5
1.4 Schematic view of a continuous casting system 9
1.5 Share of continuous casting products in total crude steel in the world [2] . . . 9
1.6 Sketch of a Hartmann boundary layer 11
1.7 Snapshot of mini-LIMMCAST in HZDR 12
1.8 Schematic view of the measuring volume inside the ultrasonic beam transmitted by an ultrasonic transducer into a liquid medium 12

2.1 Reynolds decomposition of velocity 16
2.2 Schematic of flow regime in a vertical pipe [22] 22
2.3 Relationship between drag coefficient and Reynolds number for a sphere [10] . 24
2.4 Schematic of lift force in a vertical pipe flow [85] 24
2.5 Wall function, i.e. horizontal velocity near the wall with mixing length model 27

3.1 Control volume definition 33
3.2 Configuration of test case 36
3.3 Lorentz force density profile along X-axial at half height 37
3.4 Distribution of electrical current in a cross-section at half height, (left: Ha=30, right: Ha=60) 37
3.5 Distribution of Lorentz force in a cross-section at half height, Ha=60 38
3.6 Current distribution at a cross section, electrically insulating wall 39
3.7 Velocity profiles at center lines at half height 40

4.1 Computational domain and mesh based on the geometry of the mini-LIMMCAST facility 41
4.2 Monitoring positions and spatial-averaging regions in which instantaneous vertical velocities are evaluated in the midplane between widefaces. (Dashed lines are boundaries of the cylindrical UDV measurement regions, $x = 0.02\ m$ and $x = 0.045\ m$): p1 ($0.0245\ m$, $0\ m$, $0.25\ m$), p2 ($0.0245\ m$, $0\ m$, $0.23\ m$), p3 ($0.0245\ m$, $0\ m$, $0.21\ m$) 43
4.3 Plots of the imposed external static magnetic fields for calculations in the mold, $B_0 = 0.31\ T$ 43
4.4 Mapping area of UDV and position of transducers in mini-LIMMCAST mold, (a) mapping area from $z = 0.18\ m$ to $z = 0.27\ m$ 44
4.5 Contour plots of the time-averaged horizontal velocity in the midplane parallel to the mold wide face without any applied magnetic field 44

4.6 Contour plots of the time-averaged horizontal velocity in the midplane parallel to the mold wide face with electrically insulating mold walls, $B_0 = 0.31\ T$ (within the dotted lines) 45
4.7 Contour plots of the time-averaged horizontal velocity in the midplane parallel to the mold wide face with electrically conducting mold walls, $B_0 = 0.31\ T$ (within the dotted lines) 46
4.8 Contour plots of the time-averaged α_μ in the midplane parallel to the mold wide face, $B_0 = 0.31\ T$ 46
4.9 Profiles of the time-averaged vertical velocity along a vertical line in the midplane at $x = 0.02\ m$: (a) $B_0 = 0$; (b) $B_0 = 0.31\ T$, insulating mold; and (c) $B_0 = 0.31\ T$, conducting mold (solid line: numerical results; points: experimental data filled in the values of the minimum and maximum) 47
4.10 Profiles of the time-averaged vertical velocity along a vertical line in the midplane at $x = 0.045\ m$: (a) $B_0 = 0\ T$; (b) $B_0 = 0.31\ T$, insulating mold; and (c) $B_0 = 0.31\ T$, conducting mold (solid line: numerical results; points: experimental data filled in the values of the minimum and maximum) 47
4.11 Streamlines of the time-averaged velocity in the midplane parallel to the mold wide face with electrically insulating walls obtained from numerical simulations using a modified turbulence model 49
4.12 Profiles of the time-averaged vertical velocity at different magnetic field intensities in an electrically insulating mold; data were recorded along a horizontal line in the midplane parallel to the mold wide face at $z = 0.018\ m$ 50
4.13 Streamlines of the time-averaged velocity in the midplane parallel to the mold wide face with electrically conducting walls obtained from numerical simulations using a modified turbulence model except for (c) where the common RANS model was used 51
4.14 3-D distribution of the induced electrical currents around the jets discharging from the SEN, EMBr ruler ($B_0 = 0.31\ T$) 52
4.15 2D distribution of the induced electrical currents in a $y - z$ cross-section at $x = 0.0245\ m$, EMBr ruler ($B_0 = 0.31\ T$): (a) insulating mold, $C_W = 0$ and (b) conducting mold, $C_W = 0.133$. Dashed line stands for the interface between the mold and the inserted brass plates. The jet position is indicated by the gray insert represented by a velocity isosurface at $0.4\ m/s$ 52
4.16 Distribution of the electrical potential in the midplane parallel to the wide face, EMBr ruler ($B_0 = 0.31\ T$): (a) insulating mold, $C_W = 0$ and (b) conducting mold, $C_W = 0.133$ 53
4.17 Distribution of the Lorentz force for the case of an electrically insulating mold wall, $B_0 = 0.31\ T$: (a) in the midplane, $y = 0$ and (b) near the wall, $y = 0.0174\ m$ 53
4.18 Distribution of the Lorentz force for the case of an electrically conducting mold wall, $B_0 = 0.31\ T$: (a) in the midplane, $y = 0$ and (b) near the wall, $y = 0.0174\ m$ 54
4.19 Time series of the instantaneous horizontal velocity without magnetic field at the position P2 55
4.20 Time series of the instantaneous horizontal velocity for $B_0 = 0.31\ T$ in the electrically insulating mold at the position P2 55
4.21 FFT of the instantaneous horizontal velocity for $B_0 = 0.31\ T$ in the electrically insulating mold at the position P2 56
4.22 Snapshots of velocity vector field in the midplane of the mold for the case of an electrically insulating wall ($B_0 = 0.31\ T$) 57

4.23 Time series of the instantaneous horizontal velocity for $B_0 = 0.31\ T$ in the electrically conducting mold at the position P1 (top), P2 (middle) and P3 (bottom) 58
4.24 Snapshots of velocity vector field in the midplane of the mold for the case of an electrically conducting wall, $B_0 = 0.31\ T$ 59
4.25 Streamlines of the time-averaged velocity in the midplane parallel to the mold wide face with different electrical conductivities of the wall ($B_0 = 0.31\ T$) . . 60
4.26 Shear velocity along the x-axis at $y = 0$ on the free surface with different wall conductance ratio ($B_0 = 0.31\ T$) 61
4.27 Streamlines of the time-averaged horizontal velocity in the midplane parallel to the mold wide face varying with Mc 61

5.1 Schematic view of the bubble-driven flow under consideration 66
5.2 Exemplary mesh used for the simulations 66
5.3 Schematic representation of the liquid metal column showing two different types of outlet boundary conditions: degassing outlet condition (left) and opening outlet condition (right) 67
5.4 Contour plots of the liquid vertical velocity at the vertical mid-plane, $Q_G = 0.83\ cm^3/s$ 68
5.5 Profiles of the axial liquid velocity for both outlet boundary conditions at $Q_G = 0.83\ cm^3/s$ 69
5.6 Profiles of the vertical liquid velocity along a line at $r/R = 0.87$ for two turbulence models and two outlet boundary conditions at $Q_G = 0.83\ cm^3/s$ 69
5.7 Vertical and radial profiles of the vertical liquid velocity for two turbulence models calculated at $Q_G = 0.33\ cm^3/s$ 70
5.8 Contour plots of the vertical liquid velocity obtained by the correction model for a longitudinal magnetic field at $Q_G = 0.33\ cm^3/s$ 71
5.9 Radial profiles of the vertical liquid velocity along the cylinder diameter at $z/H = 0.5$ for a longitudinal magnetic field at $Q_G = 0.33\ cm^3/s$ 71
5.10 Streamlines of the time-averaged liquid velocity in a transverse magnetic field for $Ha = 271$: (a and c) $Q_G = 0.83\ cm^3/s$, (b and d) $Q_G = 3.67\ cm^3/s$. (a and b) conventional turbulence model, (c and d) modified turbulence model taking into account the anisotropy coefficient as described in the text 73
5.11 Distributions of the electrical current density (streamlines) and the velocity (cones) over the cross section at $z/H = 0.5$ 74
5.12 Vector plots of the liquid velocity at the center plane perpendicular to the direction of the transverse magnetic field for $Q_G = 0.83\ cm^3/s$ and $Ha = 271$ 74
5.13 Time series of the local liquid velocity for various Hartmann numbers ($Q_G = 3.67\ cm^3/s$, $r/R = 0.87$, $z/H = 0.5$) 75
5.14 Contour plots of the void fraction at the free surface in a transverse magnetic field at $Q_G = 0.83\ cm^3/s$ 76
5.15 Total kinetic energy of the liquid motion as a function of the Hartmann number 76
5.16 Schematic drawing of the Lorentz force and the liquid velocity in the mid-plane parallel to the direction of the transverse magnetic field 76

6.1 Computational domain and mesh 81
6.2 Location of special points and lines in the mold midplane across the wide face 82
6.3 Streamlines of time-averaged velocity and distribution of time-averaged bubble void fraction in the mid-plane parallel to the wide face for different bubble diameters, $B_0 = 0$ 84

6.4 Escape location of bubbles from the top surface for different bubble diameter over time, $B_0 = 0$ 85
6.5 Streamlines of time-averaged velocity and distribution of time-averaged bubble void fraction in the mid-plane parallel to the wide face for different bubble diameters. (electrically conducting wall, $B_0 = 0.31\ T$) 86
6.6 Escape location of bubbles from the top surface for different bubble diameter over time. (electrically conducting wall, $B_0 = 0.31\ T$) 87
6.7 Plot of horizontal velocity on a horizontal center line at $z = 0.328\ m$, $B_0 = 0$ 88
6.8 Plot of horizontal velocity on a horizontal center line at $z = 0.328\ m$, $B_0 = 0.31\ T$, electrically conducting wall 88
6.9 Plot of horizontal velocity on a vertical center line at $x = 0.068\ m$, $B_0 = 0$. 89
6.10 Plot of horizontal velocity on a vertical center line at $x = 0.068\ m$, $B_0 = 0.31\ T$, electrically conducting wall 89
6.11 3d distribution of gas void fraction over time varying with electrical wall boundary conditions 90
6.12 Time-averaged contours of turbulent kinetic energy in the mid-plane across the wide face 90
6.13 Vortex cores for the different boundary conditions: a) $B_0 = 0$; b) $B_0 = 0.31\ T$ insulating wall; c) $B_0 = 0.31\ T$ conducting wall 91
6.14 Shear strain rate for different boundary conditions 92
6.15 Time series of liquid metal velocity at one position ($0.024\ m$, 0, $0.229\ m$) . . . 92
6.16 Distributions of time-averaged gas void fraction in the mid-plane across the wide face for electrically conducting wall (left parts: streamlines of bubbles) . 93
6.17 Streamlines and distributions of time-averaged liquid metal velocity in the mid-plane across the wide face for electrically conducting wall 94
6.18 Distribution of bubble size fraction on a horizontal centerline at $z = 0.28\ m$ without magnetic field 95
6.19 Distribution of bubble size fraction on a horizontal centerline at $z = 0.28\ m$. (electrically conducting wall, $B_0 = 0.31\ T$) 96
6.20 Time-averaged streamlines of liquid metal velocity in the mid-plane for different wall conductance ratio at $B_0 = 0.31\ T$ 96
6.21 Time-averaged liquid metal velocity along the vertical centerline at 1 mm to the narrow face for different wall conductance ratios 96

List of Tables

1.1 Properties of $Ga_{68}In_{20}Sn_{12}$ and the mold wall in the model experiments . . . 13

3.1 Implementation of mathematical models in CFX 35
3.2 Properties of liquid and geometry 37

4.1 Operating parameters with $Mc = 2.0$ 59
4.2 Operating parameters with $Mc = 0.63$ 60

6.1 Bubble size and size fraction 79

1 Introduction

Modern steels are made with varying combinations of alloying metals to fulfill many purposes, for instance, in the construction of roads, railways, other infrastructure, buildings, appliances, cars and so forth. To become steel, it must be melted and reprocessed to reduce the carbon to the correct amount, at which point other elements can be added. This liquid is then continuously cast into long slabs or molded into ingots. The productivity and quality of a continuous caster depend mainly on process parameters, i.e. casting speed, casting temperature, depth of Submerged Entry Nozzle (SEN), cleanliness of the melt, water flow rates in the different cooling zones, etc. The phenomena in the casting mold are very complex, including heat transfer, mass transfer, phase change, chemical reaction, etc. Many quality problems that originate during continuous casting can be directly attributed to poor control of fluid flow conditions, fluctuations on flow rate from the tundish into the mold cavity and changes of the nozzle exit port flow patterns. Therefore, flow control in the mold takes a crucial role in the continuous casting process to improve the quality and productivity, whereby magnetic fields have substantial capabilities to improve the quality of the steel and to enhance the productivity of the process

1.1 Research Objectives

Generally, the fluid flow in the metallurgical plant is highly turbulent and presents a complex coupling with heat transfer, phase transfer, chemical reaction, momentum transportation, etc. Owing to the complexity and lack of reliable measuring techniques, it has not been fully understood until now. CFD simulations provide information about flow and fluid properties that may be difficult or costly to obtain by measurements and which provides insight and understanding into the performance of a product or flow behaviour in a specified situation. The ready applicability of CFD today has caused its usefulness to be recognized in many areas. Computational models of fluid flow can be useful tools to study and quantify these problems. The overall objective of this work concentrates on investigating the effect of electromagnetic braking and gas injection on the fluid flow in a continuous casting slab mold numerically and making verifications on basis of a small Liquid Metal Model for Continuous Casting of steel (mini-LIMMCAST). Numerical calculations were performed by means of the software package CFX with an implemented RANS-SST (Reynolds-averaged Navier-Stokes-Shear Stress Transport) turbulence model. The non-isotropic nature of the MHD turbulence was taken into account by specific modifications of the turbulence model. This work is dedicated to pursuing a flexible mathematical model which is able to deal with complex industrial flow under the influence of external magnetic field and obtain a better understanding of flow control in the continuous casting process.

1.2 Motivation for the thesis

In a continuous casting process, productivity and quality are commonly concerned by both producers and customers. A longitudinal facial crack is a special type of defect that only occurs in continuous casting processes. This defect is caused by uneven cooling, both primary cooling and secondary cooling, and includes molten steel qualities, such as the chemical composition being out of specification, cleanliness of the material, and homogeneity. In a slab

steel casting process, the jets impinging against the narrow face may cause shell thinning, and even breakouts, if the superheat is too high and the interfacial gap is excessive. Fluid flow in the continuous casting process can cause many different types of defects in the final products, so small improvements in flow pattern can have a big impact. The decisive relationship between the quality of the solidified steel products and the properties of the melt flow during the continuous casting process has been demonstrated in many studies (for instance, see the references in [96]). Insufficient surface flow tends to make meniscus freezing and related surface defects. Excessive surface shear velocity may entrain mold-slag inclusions and lead to surface level variations and fluctuations with time. Deep penetration of the jet entering the mold cavity promotes the capture of subsurface inclusions. Fluid flow in the mold is controlled by many design and operation conditions, for example, design of submerged entry nozzle (SEN), mold size, casting speed, flow rate of gas injection, etc. Understanding the basic physics behind the continuous casting process is beneficial to improve the productivity and quality. For example, the SEN controls the flow pattern developed in the casting mold, since the SEN governs the speed, direction and other characteristics of the liquid jet entering the mold. The jet in turn influences the ultimate quality of the product through its effect on surface waves, heat and mass transfer [55, 92, 97, 48, 91].
Application of various magnetic fields provides an innovative and efficient tool for an effective and contactless flow control in the mold, which facilitates substantial capabilities to improve the quality of the steel and to enhance the productivity of the process. The external magnetic field is of potential to control fluid flow in the mold cavity by damping, accelerating, levitating, and stirring. Multitude implementations of magnetic field damping on the continuous casting process have been categorized as follows:

1. Electromagnetic Brakes (EMBr): There are two typical Electromagnetic Brakes: EMBr Ruler and EMBr Local Field. EMBr Ruler with a surrounding yoke and cores with two part coils guiding the magnetic field towards the mold (see Fig. 1.1(a)). The braking area of the Ruler covers substantially the entire width of the slab. EMBr Local Field is of four part coils with electrical copper windings together with cores and outer yokes (see Fig. 1.1(b)). The braking area covers the steel outlet from the SEN.

2. Flow Control Mold (FC-Mold): The Flow Control Mold (FC Mold) was developed on the basis of Kawasaki Steel's operational experience of the first generation of EMBr. This system produces two static magnetic fields covering the entire width of the strand, one at the meniscus and the other through the lower part of the mold (see Fig. 1.1(c)).

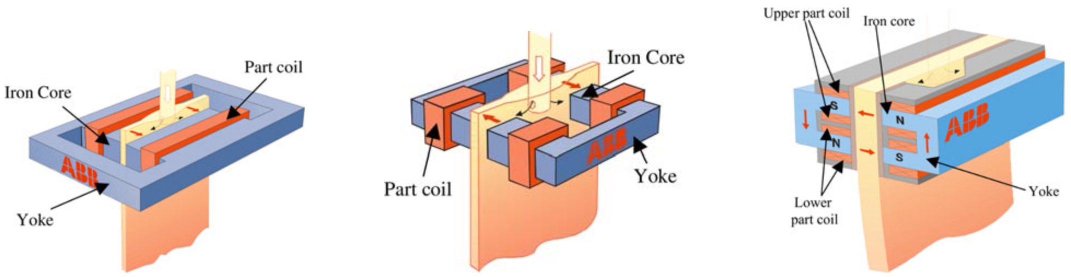

(a) EMBr Ruler (b) EMBr Local Field (c) FC Mold

Fig. 1.1: Types of the imposed external static magnetic fields for a continuous casting slab mold (from ABB comany)

The principle of an electromagnetic brake (EMBr) employs a static magnetic field aligned perpendicular to the main flow direction. It relies on the interaction between the electrically conducting melt and the applied magnetic field resulting in a retarding force to slow down the mold flow and to damp strong velocity fluctuations. A uniform reduction of the melt flow especially in the neighborhood of the jet emerging from the submerged entry nozzle (SEN) is the main goal of the flow control because violent flows at high velocities are supposed to cause an entrapment of bubbles or non-metallic inclusions impairing therefore the steel cleanliness significantly. When a magnetohydrodynamic (MHD) flow is studied in the presence of an external DC magnetic field, we basically encounter two boundary conditions: electrically insulating wall and electrically conducting wall. Figure 1.2 illustrates the distribution of electric currents in a MHD duct flow with electrically insulating wall and electrically conducting wall, respectively. When an electrically conducting viscous incompressible fluid flows through ducts and a uniform steady magnetic field acts perpendicular to the channel walls, the distribution of electric currents present significant variations. For electrically insulating wall (see Fig. 1.2(a)), the electric currents make closure inside the channel and are intensified in the vicinity of the walls. The walls normal to and parallel to the direction of the external magnetic field are named Hartmann wall and side wall, respectively. For electrically conducting wall (see Fig. 1.2(b)), the electric currents are able to pass through the interface between liquid and solid shell. Obviously the boundary condition is very important when we deal with MHD flow. To begin with investigating the EMBr effect in a continuous casting steel slab mold, we need to know the boundary condition in detail. Figure 1.3 shows a schematic of slab mold in a center-plane across the wide face. The magnetic field is applied perpendicular to the wide face, the cyan solid line present the induced electric currents. A layer of re-solidified flux exists between the liquid pool and the water-cooling copper mold. The electrically insulating wall is assumed on account of the small electrical conductivity of the re-solidified flux. Therefore, the electrically insulating wall boundary condition is treated by most of numerical simulations in the past. In reality, however, the electrical conductivity of the solidified steel shell has to be taken into account, which is larger compared to that of the molten steel. The induced electric currents prioritize through the solidified shell in preference to making closures in the vicinity of the wall with the application of external magnetic field. Such influence of wall boundary condition is characterized by a nondimensional parameter, the wall conductance ratio:

$$C_W = \frac{2\sigma_W \delta_W}{\sigma L} \tag{1.1}$$

where σ_W denotes electrical conductivity of wall, δ_W is the thickness of the wall, σ is electrical conductivity of liquid and L is the length scale (half of slab width). In addition, argon gas is normally injected into the SEN to protect clogging. However, the interplay between the turbulent liquid metal two-phase flow and the magnetic field turns out to be rather complex. On one hand, the magnetic field should have a considerable influence on the bubble velocity, the bubble shape or the distribution of the gas in the cross section of the mold. On the other hand, the void fraction also determines the closure of the induced electric current in the melt and, therefore, the distribution of the Lorentz force. An electrically insulating gas bubble does not experience a direct impact of the electromagnetic force, however, the pressure and the velocity field in the surrounding conducting fluid are strongly affected by the applied magnetic field. Modifications of the bubble shape, the drag coefficient or the trajectory are expected to exert a significant influence on the dynamics of a dispersed bubbly flow. Our motivation is to develop a flexible three-dimensional turbulence model based on a validation using a liquid metal mold with electrically insulating wall and electrically conducting wall, respectively, so that we can get an insight into the effect of EMBr and gas injection on the flow pattern in a continuous casting steel slab mold.

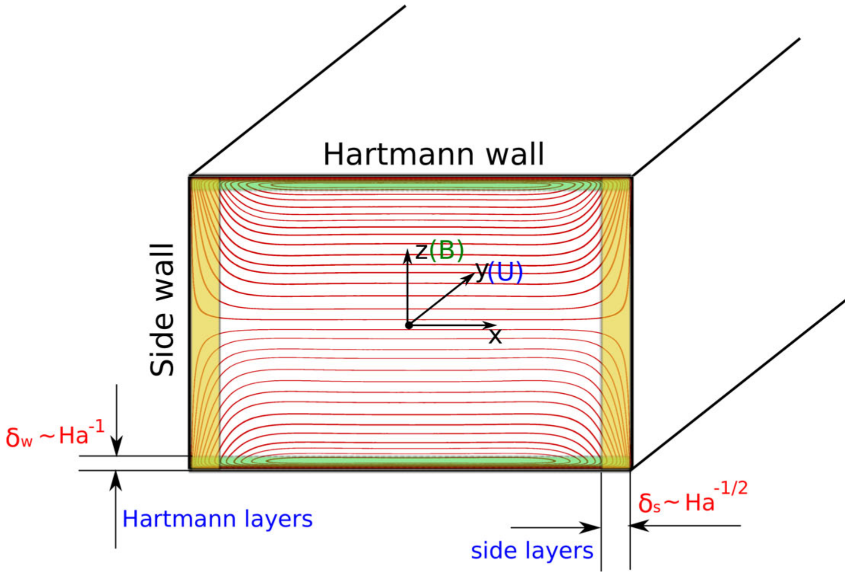
Hartmann wall
Side wall
z(B)
y(U)
x
$\delta_w \sim Ha^{-1}$
Hartmann layers
side layers
$\delta_s \sim Ha^{-1/2}$

(a) electrically insulating wall

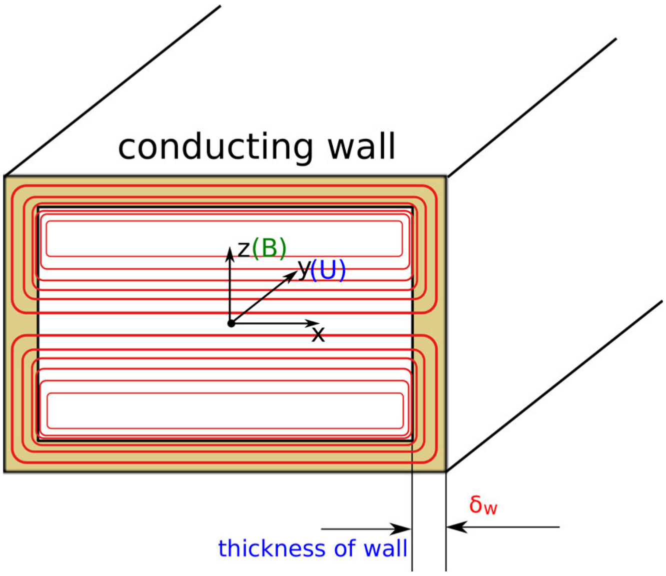
conducting wall
z(B)
y(U)
x
thickness of wall
δ_w

(b) electrically conducting wall

Fig. 1.2: Distribution of electric currents in a rectangular duct flow with a homogeneous DC magnetic field (a homogeneous DC magnetic field, B, is applied in z direction; the fluid flow s in x axis with velocity U.)

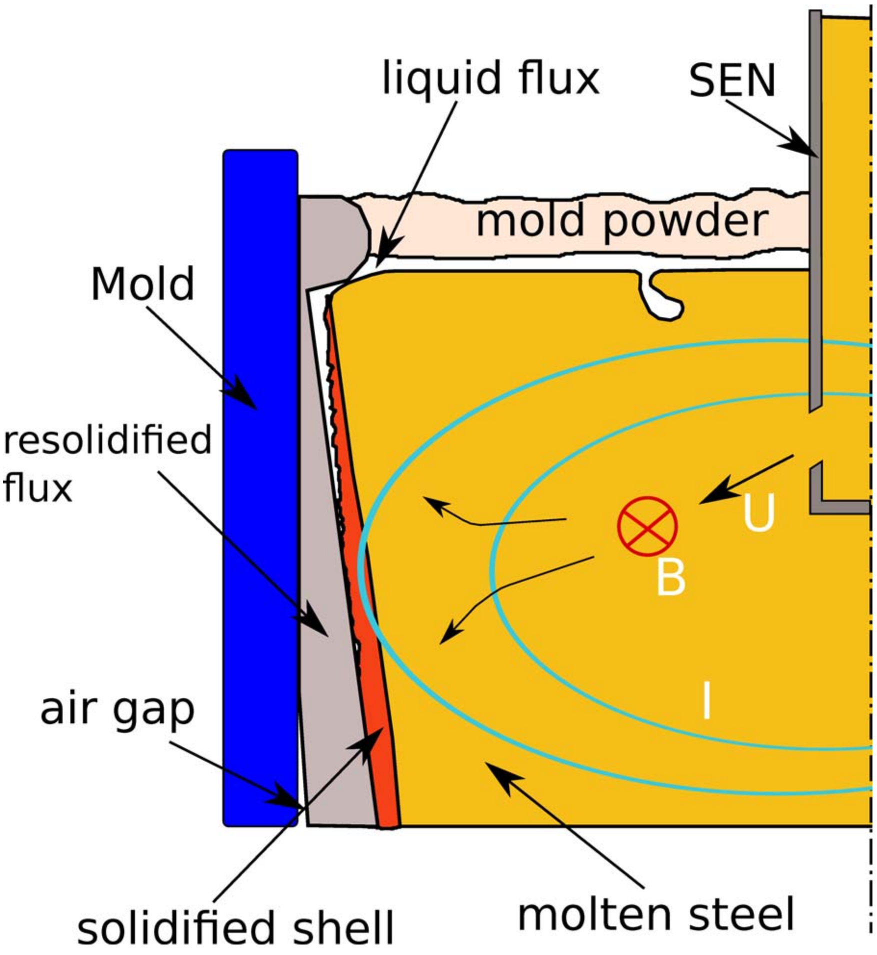
liquid flux
SEN
mold powder
Mold
resolidified flux
U
B
I
air gap
solidified shell
molten steel

Fig. 1.3: A schematic of steel slab mold in a center-plane across the wide face (static DC magnetic field B is imposed perpendicular to the wide faces in a slab mold; liquid metal discharged from SEN into the liquid pool crossing B; the corresponding induced electric currents make closure in the mold)

1.3 Literature review

1.3.1 EMBr effect in a single-phase continuous casting process

Although various EMBr designs have already been adopted for industrial use since more than 20 years [61, 42], the impact of a DC magnetic field on such highly turbulent and complex flows is a complicated phenomenon and has not been fully understood until now. Contrary to the usual expectations, static magnetic fields may even destabilize liquid metal flows. Respective indications have been found in convection experiments in liquid metals, where it could be demonstrated that a weak DC magnetic field can enhance the convective heat transfer [80, 79, 9]. First, direct observations of the destabilizing effect on the velocity field by an applied DC magnetic field were reported by Zhang et al [94, 95], who considered the imposition of a horizontal magnetic field on a bubble-driven flow inside a cylindrical liquid metal column. For a certain parameter range, the DC magnetic field gives rise to the development of distinctive transient flow pattern with increased turbulent perturbations.
In spite of physical models, CFD (computational fluid dynamics) is now used widely in industries, for instance, the impact of an EMBr on the melt flow in the continuous casting mold was addressed by many numerical studies considering various magnetic field configurations or examining the influence of variations of different casting parameters on the magnetic field effect exerted by a given assembly. There is no doubt that an EMBr affects the jet characteristics and the entire flow pattern in the mold significantly. Most of the authors rely on a $k-\varepsilon$ turbulence model and report a suppression of the mean flow and the turbulent fluctuations as well. The convective heat transfer is usually decreased and violent deflections of the free surface can be diminished. Cukierski and Thomas [12] studied the configuration of a local EMBr and documented remarkable effects of the magnetic field on the jet angle, the impingement depth, the recirculation zones and the surface velocity. Kim et al [39] employed a revised variant of a low Reynolds-number $k-\varepsilon$ turbulence model to simulate the mold flow under the influence of a local magnetic field. Wang and Zhang [87] obtained a lowering of the turbulent kinetic energy at the SEN outports and a more uniform flow pattern in the mold if a local EMBr is applied. Similar findings were presented for local EMBr [68], magnetic fields of the ruler type [46, 47] or in a FC mold [30]. The efficiency of braking the velocity at the free surface or the penetration depth of inclusions was suggested to depend on the position and intensity of the magnetic field. A comparison between local and ruler EMBr was drawn by Harada et al [26] showing a higher braking efficiency provided by a level magnetic field. These numerical results based on Large Eddy Simulations (LES) are supported by accompanying mercury model experiments. It is interesting to note that a sensitive dependence of the surface velocity on the nozzle conditions was observed in case of a local EMBr. A related study based on LES was performed by Takatani [81] who described the general effect of the local magnetic field as a suppression of the turbulent flow and a tendency of the flow pattern to become two-dimensional. Furthermore, he found that the electromagnetic brake may accelerate the fluctuations and the meniscus flow in some cases, in particular for an improper selection of the nozzle discharge angle.

1.3.2 Bubbly flow with an external magnetic field

In principle, interactions of bubbles exert a great impact on the flow pattern in a bubbly flow system. Three basic flow regimes were observed by Evans et al [22] during the experimental trials in the down-flowing column for the range of gas and liquid velocities. These were (i) bubbly, (ii) churn-turbulent flow, and (iii) annular flow. Flow regimes are closely dependent on the gas void fraction. Wallis [86] defined the critical void fraction, 0.27, which is the void fraction at zero gas drift flux where bubble coalescence commences and churn-turbulent flow begins. It is in reasonable agreement with the value obtained by Evans and Jameson [21] for turbulent liquid flow in a down-flowing air-water system.

Some few theoretical papers are devoted to the magnetic field impact on the shape of a single bubble rising in a liquid metal [82, 72, 70]. Unfortunately, respective experimental results are not available because of the still missing availability of measuring techniques to provide a reliable reconstruction of the surface of a gas bubble inside an opaque liquid metal. Shin and Kang [72] considered an incompressible gas bubble in an axisymmetric straining flow under the influence of a uniform magnetic field. They predicted an elongation of the bubble along the direction of the magnetic field. This bubble elongation increases monotonously as the magnetic interaction parameter N_B increases. The phenomenon of bubble elongation in field direction was also reported by Shibasaki et al [70] for a bubble rising inside a steady magnetic field parallel to the gravity force. Takatani [82] studied two configurations of a bubble ascending in either a vertical or a horizontal magnetic field. In case of a longitudinal field the bubble contour is transformed to a bullet-like shape, which reduces the flow resistance, but leaves the terminal velocity almost unaffected compared to the situation without magnetic field. In contrast, the shape of the bubble becomes flat if a transverse field is applied. The resulting bubble velocity is supposed to be lower than that without magnetic field.

Experimental investigations on rigid spheres revealed an increase of the drag coefficient proportional to the square root of the interaction parameter, N. Galfgat [24] and Eckert et al [19] investigated the influence of a transverse magnetic field on the velocity slip ratio in a channel flow. The linear dependence of the drag coefficient on the magnetic field strength would imply a continuous decrease of the slip ratio with rising magnetic flux. However, the slip ratio was found to be reduced only at moderate values of the magnetic field strength, but increases again at higher values of the field intensity. This tendency is caused by the braking effect on the liquid metal flow, which is proportional to B^2 and becomes dominant at high field intensities therefore.

Experiments with single bubbles in stagnant liquid metal pools have demonstrated that an imposed DC magnetic field modifies the drag coefficient. A vertical magnetic field damps the horizontal components of the bubble velocity. This effect forces the bubble into a straighter path and reduces the apparent drag force [93]. Similar observations were made by Mori et al [59] in a transverse magnetic field. A suppression of the zig-zag motion of the bubble leads to a higher terminal velocity. By contrast, the terminal velocity of bubbles moving along a rectilinear way decreases with increasing field strength.

Another study was focused on turbulent dispersion of gas bubbles in an MHD duct flow [18] which were initially injected from a point source. The application of a transverse magnetic field results in an anisotropic distribution of the void fraction over the duct cross-section with a significantly higher dispersion coefficient found for the direction parallel to the field lines. This finding indicates that the damping of turbulent fluctuations is much more pronounced in the direction parallel to the magnetic field than in the perpendicular direction. That means that the bubble dispersion is determined by the existence of quasi-two-dimensional fluctuations with a vorticity along the magnetic field direction being well-known for MHD turbulence [76].

The rise of gas bubbles drives a flow inside the liquid metal and acts as a source of turbulence. Gherson and Lykoudis [25] investigated a mercury pipe flow with dispersed nitrogen bubbles. At large magnetic fields they found regions with liquid turbulent fluctuations higher than in the case without magnetic field. The authors explain this observation by a magnetically-induced redistribution of the void fraction with the formation of large but unstable bubbles. The higher frequency of bubble break-up processes cause an additional turbulence production.

Recently, Zhang et al [94, 95] presented an experimental study with respect to the impact of a DC magnetic field on a bubble plume in a cylindrical liquid metal column. Measurements of the liquid velocity revealed that a transverse magnetic field might provoke a destabilization of the global flow resulting in transient, oscillating flow structures with predominant frequencies.

That outcome seems to be contrary to usual expectations, because the Lorentz force is often supposed to cause a deceleration of the mean flow and a damping of turbulent fluctuations.

1.3.3 Effect of EMBr and gas injection in a continuous casting process

Gas injection is necessary to prevent SEN from clogging and to reduce the quantity of inclusions in molten steel by attaching. But with gas injection, the gas phase may often cause the entrainment of mold slag into the liquid pool resulting in defects. In a steel continuous casting process the bubbly flow regime is the most desirable operational regime because the small discrete bubbles provide the greatest collection efficiency for inclusions, and also minimise the generation of unwanted turbulence within the casting mould.

Bai and Thomas [4, 5, 3] employed an Eulerian multiphase model to simulate two-phase turbulent flow of liquid steel and argon bubbles in a slide gate nozzle and validated the results through PIV (particle image velocimetry) measurements at a water-air model experiment. They reported that large bubbles cause a shallower jet angle and large flow fluctuations in the mold. The bubble size increases and the size distribution become less uniform as the liquid velocity and the gas flow rate increase. All those results are in agreement with the experimental findings of [63, 64]. By means of $k-\varepsilon$ turbulence model, SEN clogging is studied by Wu et al [92]. Moreover, Ramos et al [62] studied gas-liquid flows inside the submerged entry nozzle of a slab mold and its influence in the flow in the mold by mathematical simulations and PIV. They found that bubbly and annular flows in the SEN generate structurally-uncoupled and structurally-coupled flows in the mold, respectively.

1.4 Research Background

Continuous casting (CC) is the process whereby molten metals are solidified into casts which can be further forged in the finishing mills (see figure 1.4). These semi-finished slabs, blooms, or billets are continuously casted by using unbottomed mold with water-cooling system. The continuous casting process was granted between 1840 and 1940, when the CC development was mainly in the proposal and pioneer development stage. The full range industrial development started only between 1940 and 1970 [11, 23]. Fig. 1.5 shows the share of CC production in % of total crude steel in the world [2]. By 1970, about 4% of the steel was continuously cast, and then CC technique widespread. Relative to other casting processes, continuous casting generally has a higher capital cost, but lower operating costs.

To start the casting process, firstly, a dummy bar is positioned at the bottom of the mold. Liquid metal flows through Submerged Entry Nozzle (SEN) at the bottom of the tundish and fills into the mold, and then the molten steel is solidified into a certain thickness shell in contact with the walls of the water-cooling mold. Withdrawal of the dummy bar is initiated when the liquid metal level in the mold reaches a predetermined position. When the dummy bar head reaches a certain position, it is mechanically disconnected and the dummy bar is removed. Solidification of the molten steel continues progressively as the strand moves through the casting machine, which casting conditions are established such that the strength of the solidified steel shell leaving the mold is sufficient to withstand the static pressure of the molten steel in the mold. The strand is kept cooling down in the secondary zone till reaching the torch cutoff point, where the strand is completely solidified.

A major problem that may occur in continuous casting is breakout if solidifying steel sticks to the mold surface, causing a tear in the shell of the strand. To prevent the mold wall from sticking of the solidified shell, the water-cooling mold is designed to oscillate vertically. Meanwhile, mold powder or oil is added on the top of the liquid pool in the mold to lubricate between the solidified shell and the inner walls of the mold.

Below the water-cooling mold, the secondary cooling zone is followed, on certain types of

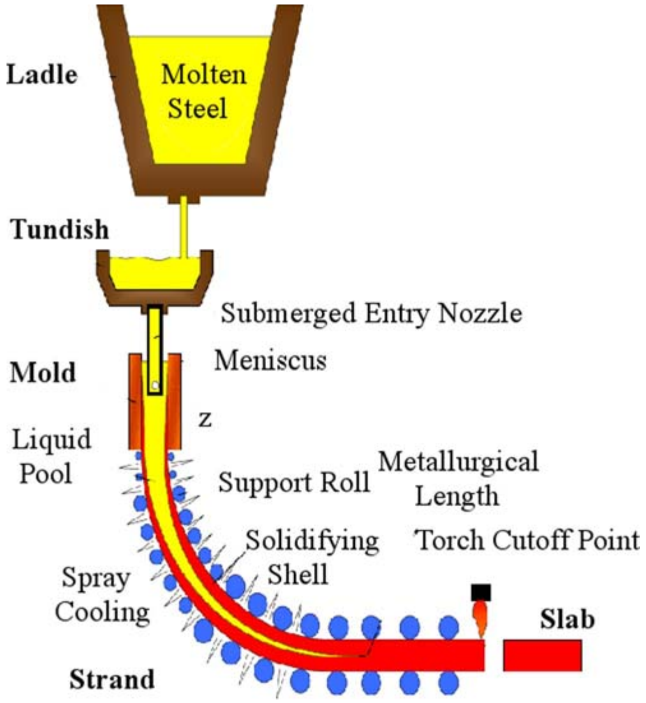
Ladle
Molten Steel
Tundish
Submerged Entry Nozzle
Meniscus
Mold
z
Liquid Pool
Support Roll
Metallurgical Length
Solidifying Shell
Torch Cutoff Point
Spray Cooling
Slab
Strand

Fig. 1.4: Schematic view of a continuous casting system

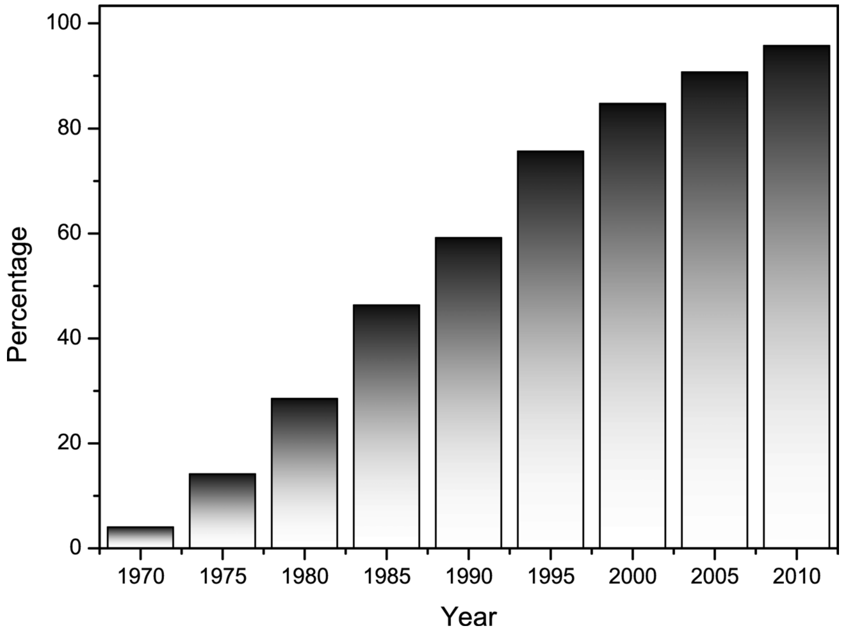

Fig. 1.5: Share of continuous casting products in total crude steel in the world [2]

machine, by a bending unit and a straightener. After straightening, the cast section is cut to the desired length either by torches or shears. The hot-cutoff lengths are then either delivered to cooling beds or transferred directly to subsequent hot and cold rolling operations.

1.5 Some fundamentals of magnetohydrodynamics

Magnetohydrodynamics (MHD) is a branch of fluid dynamics which studies the dynamics of electrically conducting fluids including plasmas, liquid metals, and salt water or electrolytes. The engineering applications of MHD are related to MHD power generation, MHD propulsor, MHD pump, plasma confinement, liquid-metal cooling of nuclear reactors, electromagnetic casting, etc. MHD can be mathematically represented by the combination of Maxwell's equations governing the electromagnetic field and the Navier-Stokes equations governing the flow field [13].

The crucial nondimensional parameters describing the influence of an external magnetic field B on the electrically conducting fluid are Reynolds number Re, Hartmann number Ha, magnetic interaction parameter N and magnetic Reynolds number Re_m, which can be written as:

$$Re = \frac{\rho U L}{\mu} \tag{1.2}$$

$$Re_m = \mu_0 \sigma U L \tag{1.3}$$

$$Ha = BL\sqrt{\frac{\sigma}{\mu}} \tag{1.4}$$

$$N = \frac{Ha^2}{Re} = \frac{\sigma L B^2}{\rho U} \tag{1.5}$$

where ρ, μ, μ_0, U represent the material properties of the liquid (density, dynamic viscosity, magnetic permeability), and the characteristic velocity. L and B denote characteristic length scale and the magnetic field, respectively.

In many practical situations, the Reynolds number Re of the flow is quite large and the magnetic Reynolds number Re_m is much less than unity. Therefore, the induced magnetic field can be neglected.

The application of an external magnetic field imposes a body force on the electrically conducting liquid, the so-called electromagnetic force or Lorentz force F_L

$$\mathbf{F_L} = \mathbf{J} \times \mathbf{B} \tag{1.6}$$

where the induced current density $\mathbf{J}$ is determined by Ohm's law

$$\mathbf{J} = \sigma\left(\mathbf{E} + \mathbf{U} \times \mathbf{B}\right). \tag{1.7}$$

The above electric field $\mathbf{E}$ can be expressed by the electric potential φ in the form of $\mathbf{E} = -\nabla\varphi$. Because of the conservation of charge Eq. (1.7) can be rewritten as

$$\Delta\varphi = div(\mathbf{U} \times \mathbf{B}). \tag{1.8}$$

When an electrically conducting viscous incompressible fluid flows through two unbounded plates or ducts and a uniform steady magnetic field acts perpendicular to the channel walls, the structure of the flow changes drastically. The velocity profile becomes flat in the core as a result of the electromagnetic braking effect. Moreover, two boundary layers develop in the vicinity of the walls which have been theoretically predicted and experimentally characterized by Hartmann [28, 29]. The main aspect is that a steady magnetic field orientates at right angles to a boundary can completely transform the nature of the boundary layer, for example,

changing its characteristic thickness.
Suppose a rectilinear shear flow adjacent to a plane, stationary surface (see Fig. 1.6). Far from the wall the flow is uniform and equal to U_∞ in x direction, and the no slip boundary condition ensures some kind of boundary layer close to the wall. A uniform magnetic field **B** is imposed in y direction. It then follows that

$$\mathbf{F}_L = \mathbf{J} \times \mathbf{B} = -\sigma B^2 U \tag{1.9}$$

The Navier-Stokes equation is given as

$$\mu \frac{\partial^2 U}{\partial y^2} - \sigma B^2 u = \frac{\partial p}{\partial x} \tag{1.10}$$

which may be transformed to

$$\frac{\partial^2}{\partial y^2}(U - U_\infty) = \frac{U - U_\infty}{\delta^2}, \delta = (\mu/\sigma B^2)^{1/2} \tag{1.11}$$

This boundary layer with the thickness $\sim \delta$ is called Hartmann boundary layer. It follows $\delta = O(Ha^{-1})$, where δ is the non-dimensional boundary-layer thickness.

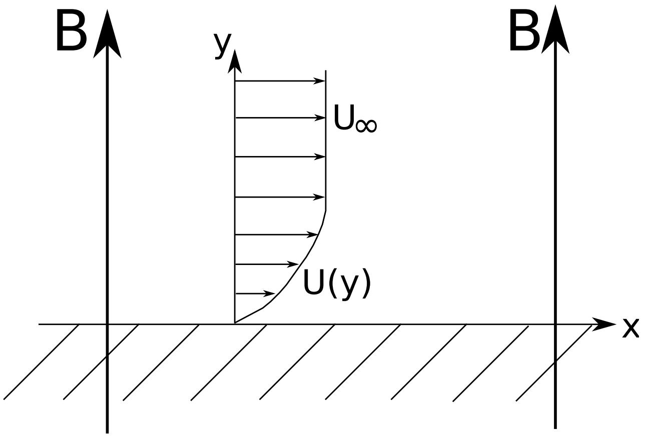

Fig. 1.6: Sketch of a Hartmann boundary layer

1.6 Experimental Setup

The LIMMCAST (LIquid Metal Model of continuous CASTing of steel) program has been established at HZDR for investigations of fluid flow and related transport processes which are of relevance for the continuous casting of steel [83, 84] (see Fig. 1.7). The experiments were conducted at the mini-LIMMCAST facility which operates at room temperature using the eutectic alloy $Ga_{68}In_{20}Sn_{12}$, which is liquid at room temperature (Table 1.1). The interest is focused on flow measurements in the mold in order to investigate the impact of a level magnetic field on the discharging jet. The experimental set-up corresponds to the configuration of a ruler EMBr. A detailed description and schematic views of the experimental facility can be found in the paper of [83] The flow measurements were conducted in a rectangular mold with a cross section of $140 \times 35 mm^2$ made of acrylic glass. The melt is discharged through the SEN with an inner diameter of $10mm$ into the mold through two oval ports on both sides of the nozzle. The DC magnetic field is installed perpendicular to the flow direction at the nozzle ports along the wide face of the mold. A maximum field strength of $0.31T$ can be achieved corresponding to a Hartmann number of 417.

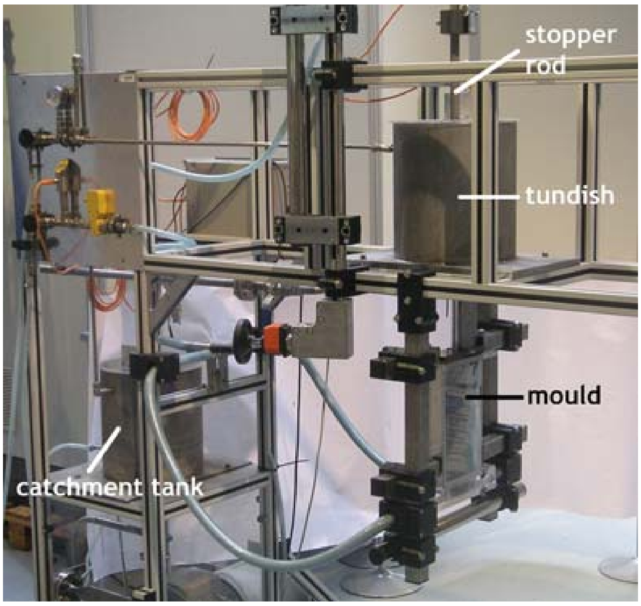
stopper rod
tundish
mould
catchment tank

Fig. 1.7: Snapshot of mini-LIMMCAST in HZDR

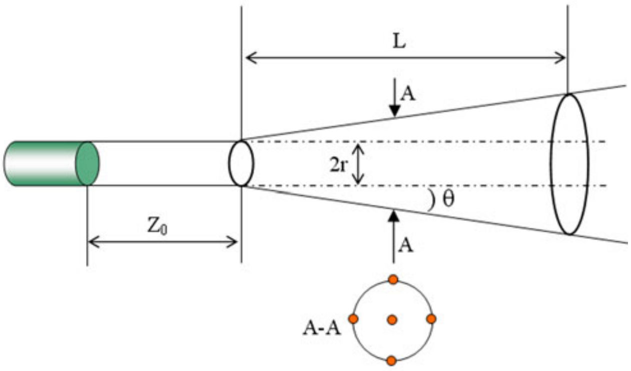
L
A
2r
θ
Z_0
A
A-A

Fig. 1.8: Schematic view of the measuring volume inside the ultrasonic beam transmitted by an ultrasonic transducer into a liquid medium

Tab. 1.1: Properties of $Ga_{68}In_{20}Sn_{12}$ and the mold wall in the model experiments

Density (ρ)	6360 $kg \cdot m^{-3}$
Dynamic viscosity (μ)	0.00216 $kg \cdot m^{-1} \cdot s^{-1}$
Electrical conductivity (σ)	3.2×10^6 $S \cdot m^{-1}$
Wall conductivity (σ_W)	15×10^6 $S \cdot m^{-1}$
Wall conductance ratio (C_W)	0.133 (brass plate)

The fluid velocity in the mold was measured by means of the Ultrasound Doppler Velocimetry (UDV) [84] using the DOP2000 velocimeter (model 2125, Signal Processing SA, Lausanne). This instrument is equipped with an internal multiplexer allowing for a sequential data recording from a maximum of ten sensors. The US transducers were installed in two ways: For measuring the horizontal velocity component perpendicular to the magnetic field direction the sensor was attached at the outer mold wall. Various measuring positions were selected along the midsection of the narrow face. Vertical velocities were determined by a direct immersion of the sensor into the melt at the free surface. The velocity profiles were acquired with a scan rate of approximately $5Hz$, whereas the lateral resolution varies between $5mm$ at measuring depths close to the sensor and approximately $9mm$ at a measuring depth of $100mm$. A velocity resolution of about $2.5mm/s$ was achieved. To investigate transient characteristics of fluid flow in the mold, instantaneous velocities are obtained by an ultrasound transducer of $90Hz$ scan rate.

According to figure 1.8, the specific shape of the measuring volume of a particular sensor at each axial position was taken into account by a spatial average using five points within the cross section of the ultrasonic beam.

To make validations of the mathematical modeling, the effective experimental results are indispensable. In this dissertation, all the experimental data based on the mini-LIMMCAST are acquired by one of my colleagues, Mr. Klaus Timmel.

2 State of the Art

2.1 Governing equations Continuum Mechanics

The numerical procedure presented in this study is done for the assumption of incompressible flow of Newtonian fluids. The transport equation for single-phase is given in a stationary frame.
The Continuity equation:

$$\nabla \cdot (\mathbf{U}) = 0 \tag{2.1}$$

The Momentum equations

$$\rho\overbrace{\Big(\underbrace{\frac{\partial \mathbf{U}}{\partial t}}_{\substack{\textit{Unsteady}\\ \textit{acceleration}}} + \underbrace{\mathbf{U}\cdot\nabla\mathbf{U}}_{\substack{\textit{Convective}\\ \textit{acceleration}}}\Big)}^{\textit{Inertia (per volume)}} = \overbrace{\underbrace{-\nabla p}_{\substack{\textit{Pressure}\\ \textit{gradient}}} + \underbrace{\mu\nabla^2\mathbf{U}}_{\textit{Diffusion}}}^{\textit{Divergence of stress}} + \underbrace{\mathbf{f}}_{\substack{\textit{Other}\\ \textit{body}\\ \textit{forces}}} \tag{2.2}$$

In our daily life almost all fluid flow which we encounter is turbulent, which for numerical solutions requires fine mesh enough to resolve all turbulent scales and also requires a small time resolution when the Navier-Stokes equations are solved numerically. For this reason, we usually use Reynolds decomposition in turbulent flow, whereby an instantaneous quantity $\widetilde{U_i}$ is decomposed into its time-averaged part U and fluctuating part u so that $\widetilde{U_i} = U_i + u_i$. Time-averaged equations of motion for fluid flow are called Reynolds-averaged Navier-Stokes equations (or RANS equations). The governing equations can be written as follows:

$$\rho U_j \frac{\partial U_i}{\partial x_j} = \frac{\partial}{\partial x_j}\left[-P\delta_{ij} + \mu\left(\frac{\partial U_i}{\partial x_j} + \frac{\partial U_j}{\partial x_i}\right) - \rho\left\langle u_i u_j \right\rangle\right]. \tag{2.3}$$

The above equations lead to the turbulence problem: the last term on the right-hand side, the Reynolds stress, is unknown. The averaged equations are not closed. The objective of turbulence models for the RANS equations is to compute the Reynolds stresses, which can be done by three main categories of RANS-based turbulence models:

1. Linear eddy viscosity models
2. Nonlinear eddy viscosity models
3. Reynolds stress models (RSM)

Linear eddy viscosity models are widely used in which the Reynolds stresses, as obtained from a Reynolds averaging of the Navier-Stokes equations, are modelled by a linear constitutive relationship with the mean flow straining field, as:

$$-\rho\left\langle u_i u_j \right\rangle = 2\mu_t S_{ij} - \frac{2}{3}\rho k \delta_{ij} \tag{2.4}$$

where μ_t is the coefficient termed turbulent "viscosity" (also called the eddy viscosity),

$$k = \frac{1}{2}\left(u_1 u_1 + u_2 u_2 + u_3 u_3\right) \tag{2.5}$$

is the mean turbulent kinetic energy

$$S_{ij} = \frac{1}{2}\left[\frac{\partial U_i}{\partial x_j} + \frac{\partial U_j}{\partial x_i}\right] - \frac{1}{3}\frac{\partial U_k}{\partial x_k}\delta_{ij} \tag{2.6}$$

is the mean strain rate.
The Reynolds-averaged Navier-Stokes equations can be given in the following form:

$$\frac{\partial}{\partial x_j}(U_j) = 0 \tag{2.7}$$

$$\frac{\partial \rho U_i}{\partial t} + \frac{\partial}{\partial x_j}(\rho U_i U_j) = -\frac{\partial p^*}{\partial x_i} + \frac{\partial}{\partial x_j}\left[(\mu + \mu_t)\left(\frac{\partial U_i}{\partial x_j} + \frac{\partial U_j}{\partial x_i}\right)\right] + S_M \tag{2.8}$$

where p^* is modified pressure defined by

$$p^* = p + \frac{2}{3}\rho k + (\mu + \mu_t)\frac{\partial U_k}{\partial x_k} \tag{2.9}$$

The last term in the above equation is neglected for incompressible flows. ρ is the fluid density, U_i is the i component of the fluid velocity, t is the time, x_j is j spatial coordinate, p is pressure, μ and μ_t are laminar viscosity and turbulence viscosity, S_M stands for the sum of body forces.
The URANS equations are the usual RANS equations, but with the transient (unsteady) term retained. Even if the results from URANS are unsteady, one is often interested only in the time-averaged flow. The time-averaged velocity is defined as $\overline{U}_i$, which means that we can decompose the results from an URANS as a time-averaged part $\overline{U}_i$, a resolved fluctuation u_i, and the modeled turbulent fluctuation u'_i. Apparently, Unsteady Reynolds-time-averaged turbulence model is capable to capture the flow fluctuation, but the modeled turbulent fluctuation,u_i , can not be shown in figure 2.1.

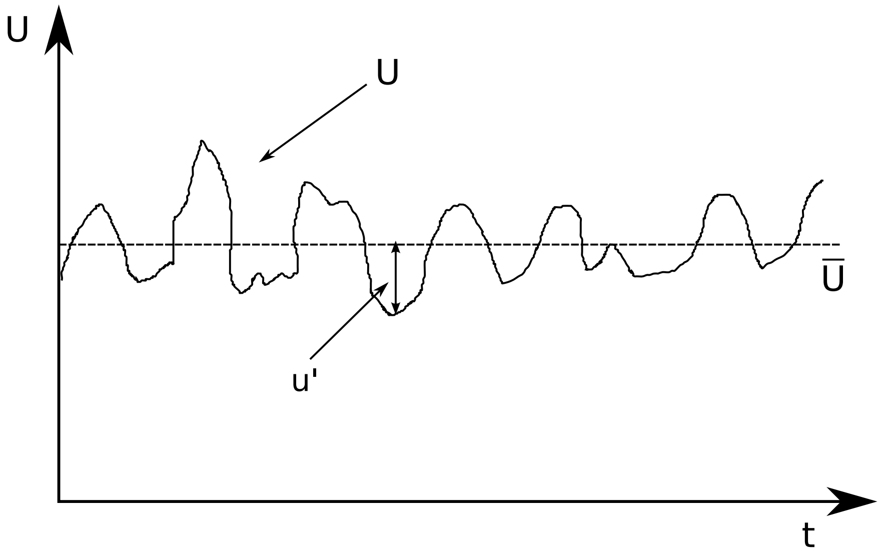

Fig. 2.1: Reynolds decomposition of velocity

2.2 Turbulence models

In fluid dynamics, the Reynolds number is used to characterize different flow regimes: laminar, laminar-turbulent transition, turbulence. Turbulence flow is a flow regime characterized by chaotic and randomness. In turbulent flow, unsteady vortices appear on many scales and interact with each other. Turbulence models are necessary because we cannot afford big enough computers to directly capture every scale of motion. As a result, there are unsteady (turbulent) motions affecting the flow that cannot be resolved directly; they must therefore be modeled. There are several subcategories for the linear eddy-viscosity models, depending on the number of (transport) equations solved for the eddy viscosity coefficient: Algebraic models; One-equation models; Two-equation models.

2.2.1 Zero-equation turbulence model

Algebraic turbulence models or zero-equation turbulence models are models that do not require the solution of any additional equations, and are calculated directly from the flow variables. As a consequence, zero equation models may not be able to properly account for history effects on the turbulence, such as convection and diffusion of turbulent energy. Ludwig Prandtl introduced the additional concept of the mixing length, along with the idea of a boundary layer. For wall-bounded turbulent flows, the eddy viscosity must vary with distance from the wall, hence the addition of the concept of a 'mixing length'. In the simplest wall-bounded flow model, the eddy viscosity is given by the equation:

$$\nu_t = \left|\frac{\partial U}{\partial y}\right| l_m^2 \tag{2.10}$$

where $\frac{\partial U}{\partial y}$ is the partial derivative of the streamwise velocity (u) with respect to the wall normal direction (y), l_m is the mixing length.
For boundary layers, δ , we have

$$l_m = \kappa y, \text{ for } y < \delta$$
$$l_m = \delta, \text{ for } y \geq \delta$$

where $\kappa = 0.41$ is the Karman constant.

2.2.2 One-equation turbulence model

One-Equation models solve a single transport equation for a quantity which is used to obtain the turbulent viscosity. For example, in Prandtl's one-equation model, kinetic eddy viscosity is defined as

$$\nu_t = k^{\frac{1}{2}} l = C_t \frac{k^2}{\varepsilon} \tag{2.11}$$

The kinetic turbulent energy is calculated by

$$\frac{\partial k}{\partial t} + U_j \frac{\partial k}{\partial x_j} = \tau_{ij} \frac{\partial U_i}{\partial x_j} - C_t \frac{k^{\frac{3}{2}}}{l} + \frac{\partial}{\partial x_j}[(\nu + \frac{\nu_t}{\sigma_k}) \frac{\partial k}{\partial x_j}] \tag{2.12}$$

where $C_t = 0.08$, $\sigma_k = 1$, l denotes the turbulent length scale and the deviatoric stress tensor is $\tau_{ij} = 2\nu_t S_{ij} - 2/3k\delta_{ij}$.
Currently, a prominent one-equation model is the Spalart-Allmaras model [77] which solves a transport equation for a viscosity-like variable.

2.2.3 Two-equation turbulence model

Two-Equation models require the solution of two additional governing equations in order to compute the contributions of turbulence to the mean flow. Two-equation turbulence models are very widely used, as they offer a good compromise between numerical effort and computational accuracy. Two of the most common models are the $k-\varepsilon$ model and the $k-\omega$ model. The $k-\varepsilon$ model is one of the most common turbulence models, although it just doesn't perform well in cases of large adverse pressure gradients [90]. Usually, there are three kinds of $k-\varepsilon$ model: Standard $k-\varepsilon$ model; Realizable $k-\varepsilon$ model; RNG(Re-Normalisation Group) $k-\varepsilon$ model. The $k-\varepsilon$ model is widely used for industrial simulations [97, 48, 62, 12, 46, 47].

$k-\varepsilon$ turbulence model

The $k-\varepsilon$ model is one of the most common turbulence models on the basis of two major formulations of k and ε. It is first introduced by Harlow et al [27] even though the development of this model is often credited to [37].

The turbulent energy, k, can be computed as:

$$k = \frac{3}{2}\,(U\,I)^2 \tag{2.13}$$

where U is the mean flow velocity and I is the turbulence intensity. U can be computed from the three mean velocity components U_x, U_y and U_z as:

$$U \equiv \sqrt{U_x^2 + U_y^2 + U_z^2} \tag{2.14}$$

The turbulence intensity, I, also often refered to as turbulence level, is defined as:

$$I \equiv \frac{\sqrt{\frac{2}{3}\,k}}{U} \tag{2.15}$$

The turbulent dissipation rate, ε, can be computed using the following expression:

$$\varepsilon = C_\mu^{\frac{3}{4}}\,\frac{k^{\frac{3}{2}}}{l} \tag{2.16}$$

where C_μ is a turbulence model constant which usually has a value of 0.09, and l is the turbulent length scale.

The turbulent viscosity is modeled as:

$$\mu_t = \rho C_\mu \frac{k^2}{\varepsilon} \tag{2.17}$$

The Turbulence kinetic energy k equation for the standard $k-\varepsilon$ model is:

$$\frac{\partial}{\partial t}(\rho k) + \frac{\partial}{\partial x_i}(\rho k U_i) = \frac{\partial}{\partial x_j}\left[\left(\mu + \frac{\mu_t}{\sigma_k}\right)\frac{\partial k}{\partial x_j}\right] + P_k - \rho\varepsilon \tag{2.18}$$

The turbulence dissipation ε equation for the standard $k-\varepsilon$ model is:

$$\frac{\partial}{\partial t}(\rho\varepsilon) + \frac{\partial}{\partial x_i}(\rho\varepsilon U_i) = \frac{\partial}{\partial x_j}\left[\left(\mu + \frac{\mu_t}{\sigma_\varepsilon}\right)\frac{\partial \varepsilon}{\partial x_j}\right] + C_{1\varepsilon}\frac{\varepsilon}{k}\left(P_k + C_{3\varepsilon}P_b\right) - C_{2\varepsilon}\rho\frac{\varepsilon^2}{k} \tag{2.19}$$

where P_k, production of k, represents the generation of turbulence kinetic energy due to the mean velocity gradients, described as:

$$P_k = -\rho\left\langle u_i u_j\right\rangle \frac{\partial U_j}{\partial x_i} = \mu_t S^2 \tag{2.20}$$

The modulus of the mean rate-of-strain tensor, S, is defined as:

$$S \equiv \sqrt{2S_{ij}S_{ij}} \tag{2.21}$$

The constants are determined from simple benchmark experiments as follows: $C_{1\varepsilon} = 1.44$, $C_{2\varepsilon} = 1.92$, $C_\mu = 0.09$, $\sigma_k = 1.0$, and $\sigma_\varepsilon = 1.3$.

$SST - k - \omega$ turbulence model

Shear Stress Transport $SST - k - \omega$ two-equation model (written in conservation form) is given by the following equations [56]:

$$\frac{\partial(\rho k)}{\partial t} + \frac{\partial(\rho U_j k)}{\partial x_j} = P - \beta^* \rho \omega k + \frac{\partial}{\partial x_j}\left[(\mu + \sigma_k \mu_t)\frac{\partial k}{\partial x_j}\right] \tag{2.22}$$

$$\begin{aligned}\frac{\partial(\rho \omega)}{\partial t} + \frac{\partial(\rho U_j \omega)}{\partial x_j} &= \frac{\psi}{\nu_t}P - \beta\rho\omega^2 + \frac{\partial}{\partial x_j}\left[(\mu + \sigma_\omega \mu_t)\frac{\partial \omega}{\partial x_j}\right] \\ &\quad + 2(1 - F_1)\frac{\rho\sigma_{\omega 2}}{\omega}\frac{\partial k}{\partial x_j}\frac{\partial \omega}{\partial x_j}\end{aligned} \tag{2.23}$$

In order to recover the original formulation of the eddy-viscosity, $\mu_t = \frac{\rho a_1 k}{\max(a_1\omega, \Omega)}$, the modification can be done by applying a blend function F_2 for free shear-layer. The turbulent eddy viscosity is computed from:

$$\nu_t = \frac{a_1 k}{\max(a_1\omega, SF_2)} \tag{2.24}$$

The production term P can be expressed for incompressible flow as:

$$P = \mu_t S \Omega \tag{2.25}$$

where S denotes the magnitude of the strain rate, S_{ij}, is the strain rate tensor, Ω is the magnitude of vorticity rate, and Ω_{ij} stands for the vorticity tensor.

$$S = \sqrt{2S_{ij}S_{ij}} \tag{2.26}$$

$$S_{ij} = \frac{1}{2}\left(\frac{\partial U_i}{\partial x_j} + \frac{\partial U_j}{\partial x_i}\right) \tag{2.27}$$

$$\Omega = \sqrt{2\Omega_{ij}\Omega_{ij}} \tag{2.28}$$

$$\Omega_{ij} = \frac{1}{2}\left(\frac{\partial U_i}{\partial x_j} - \frac{\partial U_j}{\partial x_i}\right) \tag{2.29}$$

Each of the constants is a blend of an inner (1) and outer (2) constant, blended via:

$$\phi = F_1\phi_1 + (1 - F_1)\phi_2 \tag{2.30}$$

where ϕ_1 represents constant 1 and ϕ_2 represents constant 2.

The constants are:

$$\psi_1 = \frac{\beta_1}{\beta^*} - \frac{\sigma_{\omega 1}\kappa^2}{\sqrt{\beta^*}}, \quad \psi_2 = \frac{\beta_2}{\beta^*} - \frac{\sigma_{\omega 2}\kappa^2}{\sqrt{\beta^*}},$$

$$\sigma_{k1} = 0.85, \quad \sigma_{\omega 1} = 0.5, \quad \beta_1 = 0.075,$$

$$\sigma_{k2} = 1.0, \quad \sigma_{\omega 2} = 0.856, \quad \beta_2 = 0.0828,$$

and $a_1 = 0.31$, $\beta^* = 0.09$.

Additional functions are given by:

$$F_1 = \tanh\left(\mathrm{arg}_1^4\right) \tag{2.31}$$

$$\mathrm{arg}_1 = \min\left[\max\left(\frac{\sqrt{k}}{\beta^*\omega d}, \frac{500\nu}{d^2\omega}\right), \frac{4\rho k}{\mathrm{CD}_{k\omega}\sigma_{\omega 2}d^2}\right] \tag{2.32}$$

$$F_2 = \tanh\left(\mathrm{arg}_2^2\right) \tag{2.33}$$

$$\mathrm{arg}_2 = \max\left(2\frac{\sqrt{k}}{\beta^*\omega d}, \frac{500\nu}{d^2\omega}\right) \tag{2.34}$$

The term arg_1 obviously goes to zero far enough away from solid surfaces because of the $1/d$ or $1/d^2$ dependency in all three terms. This argument ensures F_1 goes to zero towards the boundary layer edge and is equal to one in the sublayer. When F_1 is equal to one, the ω equation can be transformed into the ε equation.

The positive portion of the cross-diffusion term is given by

$$\mathrm{CD}_{k\omega} = \max\left(2\rho\sigma_{\omega 2}\frac{1}{\omega}\frac{\partial k}{\partial x_j}\frac{\partial \omega}{\partial x_j}, 10^{-10}\right) \tag{2.35}$$

and d is the distance to the next surface, $\nu_t = \mu_t/\rho$ is the turbulent kinematic viscosity.

2.2.4 Discussions and conclusions

The $k-\omega$ model is the model of choice in the sublayer of the boundary layer. Unlike any other two-equation model, it does not involve damping functions and, as will be shown, allows simple Dirichlet boundary conditions to be specified. The SST (shear stress transport) model is a blend of a $k-\omega$ model, which is used near walls, and a $k-\varepsilon$ model, which is used in regions far from walls. This model is fairly robust and generally does a good job near solid boundaries. It also is often found to do a better job at capturing recirculation regions than other models [34, 57]. Algebraic Reynolds stress models solve algebraic equations for the Reynolds stresses, whereas differential Reynolds stress models solve differential transport equations individually for each Reynolds stress component. The exact production term and the inherent modeling of stress anisotropies theoretically make Reynolds Stress models more suited to complex flows; however, practice shows that they are often not superior to two-equation models. The Large Eddy Simulation Model (LES) is an approach which solves for large-scale fluctuating motions and uses sub-grid scale turbulence models for the small-scale motion. Mathematically, the velocity field can be separated into a resolved and sub-grid part. The resolved part of the field represent the large eddies, while the sub-grid part of the velocity represent the small scales whose effect on the resolved field is included through the Sub-Grid-Scale (SGS) model. SGS turbulence models usually employ the Boussinesq hypothesis in search of calculating the SGS stress. The Smagorinsky-Lilly model is a typical one. However, it must be noted that for wall bounded flows, so called streaky structures develop in the near wall region. These streaky structures must be resolved and this leads to high resolution requirements and computing times for LES of wall-bounded flows. The alternative approach is Detached Eddy Simulation (DES), which combines elements of RANS and LES formulations in order to arrive at a hybrid formulation, where RANS is used inside attached and mildly separated boundary layers. When it is important to resolve the whole range of spatial and temporal scales of the turbulence, or for low Reynolds numbers, less than 5000,we can consider Direct Numerical Simulation (DNS). Experience has shown that the use of LES and DNS in boundary layer flows at high Re numbers is extremely expensive and therefore not applicable for many industrial flow simulations.

In this thesis, we are mainly concentrated on numerical simulations of continuous casting process in the presence of external magnetic field. The induced electric currents will be closed in the vicinity of walls while the bounded flow passes through an external static magnetic field. When the Hartmann number is large enough, the thickness of the Hartmann layer is less that of the viscous boundary layer. Therefore, the Hartmann layer (see introduction) must be considered. Under such circumstance the $k-\varepsilon$ model is not suitable any more in this case because the critical parameter, y^{+1}, must be greater than 20 by using the $k-\varepsilon$ model. In reality, the flow in the casting process is of high turbulence characteristic. LES or DNS models will be rather costly and time consuming. In addition, the quasi-steady-state is required in a continuous casting process, which the casting speed is constant when the caster is running, so that the flow in the mold is expected to be stable. Therefore $SST-k-\omega$ two-equation model is fair enough to meet the need of flow field simulations in a steel continuous casting process, for example, flow pattern at large scale, flow oscillating and fluctuating, etc. Moreover, the $SST-k-\omega$ two-equation model is chosen for the following reasons: The use of a ω equation in the inner parts of the boundary layer makes the model directly usable all the way down to the wall through the viscous sub-layer with any damping functions; The blending function switches to a $k-\varepsilon$ behavior in the free-stream to avoid the common $k-\omega$ problem that the model is too sensitive to the inlet free-stream turbulence properties. Fine meshes near the wall not only satisfy with the numerical accuracy for the $SST-k-\omega$ model, but also meet the need to resolve the Hartmann layer.

2.3 Mathematical models for multiphase flow

In gas-liquid two-phase flow, the flow pattern in a bounded flow is dependent on the void fraction of gas phase, slip velocity, interfacial shear, etc. For example, figure 2.2 shows the flow regime in a vertical pipe. In general, the flow regime is characterized as: bubbly flow, slug flow, churn flow and annular flow. In bubbly flow regime, numerous bubbles are distinguishable as the gas is dispersed in the form of discrete bubbles in the continuous liquid phase, whereby the bubbles may vary in both size and shape. In slug flow regime, coalescence of bubbles leads to form larger bubbles as a result of increasing void fraction, which are similar in size to the pipe diameter and have a characteristic shape similar to a bullet with a hemispherical nose and a blunt tail. In churn flow regime, the structure of the flow becomes unstable with the fluid traveling up and down in an oscillatory way. Once the interfacial shear of the high velocity gas on the liquid film becomes dominant over the gravity force, the liquid is expelled from the center of the pipe and flows as a thin film on the wall. In addition, liquid may be entrained in the gas core as small droplets. We call this particularly stable flow pattern as annular flow.

In the process of a steel continuous casting, generally, Argon is introduced in Submerged Entry Nozzle (SEN) to prevent nozzle ports from clogging. We expect the gas phase injected in the liquid behaves as discrete bubbles. To simulate bubbly flow, interphase momentum transfer models are introduced. Interphase momentum, M_{LG}, occurs due to interfacial forces acting on phase L by the interaction with phase G and vice versa. The interfacial forces between two phases are equal and opposite, therefore the net interfacial forces sum to zero. The detailed mathematical models are given in the following sections.

2.3.1 Basic equations

In our simulations we apply the Euler-Euler approach considering both the liquid and the gaseous phase with certain volume fractions α_L and α_G, respectively. On the supposition that any mass exchange between the phases can be neglected, the system of equations of

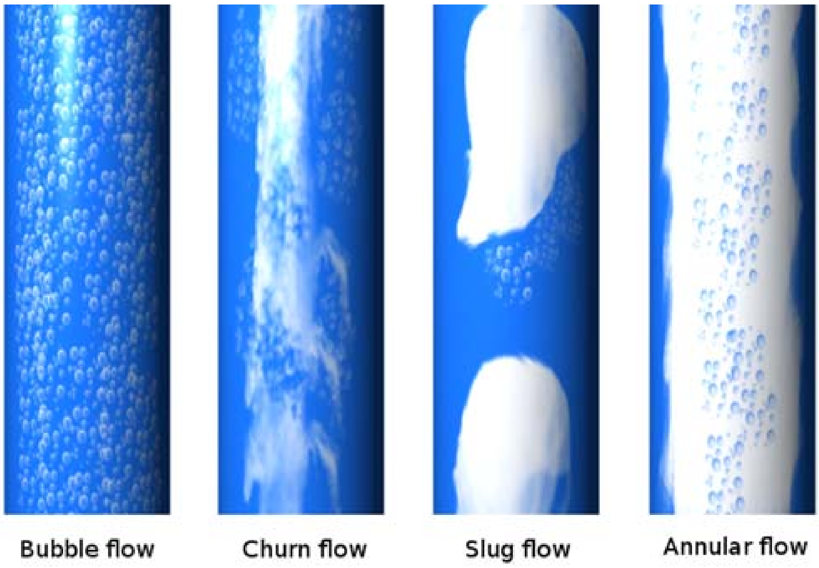

Fig. 2.2: Schematic of flow regime in a vertical pipe [22]

continuity and momentum is given as follows [17]:

$$\frac{\partial(\alpha_k \rho_k)}{\partial t} + \nabla \cdot (\alpha_k \rho_k \mathbf{U}_k) = 0 \tag{2.36}$$

$$\frac{\partial(\alpha_k \rho_k \mathbf{U}_k)}{\partial t} + \nabla \cdot (\alpha_k \rho_k \mathbf{U}_k \mathbf{U}_k) = -\nabla p - \nabla \cdot (\alpha_k \tau_k) + \alpha_k \rho_k \mathbf{g} + \mathbf{F}_{I,k} + \mathbf{F}_{L,k} \tag{2.37}$$

where the subscript $k = L$ denotes the liquid metal phase and $k = G$ the gas phase, respectively. The terms on the right-hand side of Eq. (2.37) represent the pressure gradient, the turbulent viscous stress, the gravity force, the interfacial forces $\mathbf{F}_{I,k}$, and the electromagnetic force $\mathbf{F}_{L,k}$. The summation of void fraction, α_k, is unity.

In multiphase fluid flow, the summation of the net interfacial forces is equal to zero. The interfacial forces $\mathbf{F_{I,L}}$ in Eq. (2.37) can be expressed as

$$\mathbf{F}_{I,L} = -\mathbf{F}_{I,G} = \mathbf{F}_{D,L} + \mathbf{F}_{L,L} + \mathbf{F}_{VM,L} + \mathbf{F}_{LUB,L} + \mathbf{F}_{TD,L} \tag{2.38}$$

where the terms on the right-hand side of Eq. (2.38) are the drag force, the lift force, the virtual mass force, the wall lubrication force and the turbulent dispersion force.

2.3.2 Bubble-induced turbulence

Within this study the $SST - k - \omega$ turbulence model [56] was chosen, which can be applied for calculating the turbulent shear-stress viscosity in the continuous phase. This model has to be extended for the situation of a bubbly flow. Sato et al [66, 65] proposed a model taking account the turbulence induced by the motion of dispersed bubbles. He assumed that the effective viscosity of the liquid phase is composed of three contributions: the laminar viscosity, the turbulent eddy viscosity and the bubble-induced turbulence (BIT).

$$\mu_{BIT} = C_{BIT} \rho_L \alpha_G d_G |\mathbf{U}_L - \mathbf{U}_G| \tag{2.39}$$

where the parameter C_{BIT} has a value of 0.6.
However, Deen and Dhotre et al [15, 16] found that the added bubble-induced viscosity did not alter the simulation results significantly. Considering the migration of gas bubbles through the

liquid phase and the effect of bubble-induced turbulence, Simonin and Viollet [73] included extra source terms into the turbulence models. The expressions are given by:

$$S_{t,k} = C_{k2} C_f \rho_L \alpha_L \alpha_G k \tag{2.40}$$

$$S_{t,\varepsilon} = C_{\varepsilon 2} C_f \rho_L \alpha_L \alpha_G \varepsilon \tag{2.41}$$

For the SST k-ω turbulence model, an expression has to be obtained for $S_{t,\omega}$ instead of $S_{t,\varepsilon}$. This term can be written in the form of $S_{t,\omega} = C_{\varepsilon 2} C_f \rho_L \alpha_L \ \alpha_G C_\mu \omega k$, whereas C_f stands for the interphase friction coefficient $C_f = \frac{3}{4}(C_D/d_B) \mid \mathbf{U}_G - \mathbf{U}_L \mid$. The coefficients $C_\mu = 0.09$, $C_{k2} = 0.75$ and $C_{\varepsilon 2} = 0.6$ are suggested by [69].

2.3.3 Drag force

The drag force results from the skin friction and the form drag due to the viscous surface shear stress and the pressure distribution around the bubble. A generic description for the drag force per unit volume was proposed by Clift [10] for bubbles

$$\mathbf{F}_{D,L} = \frac{3}{4} \alpha_G \rho_L \frac{C_D}{d_B} \mid \mathbf{U}_G - \mathbf{U}_L \mid (\mathbf{U}_G - \mathbf{U}_L) \tag{2.42}$$

where C_D is the drag coefficient which can be adopted by the Grace model and the Ishii-Zuber model [33]. C_D is not a constant but varies as a function of speed, flow direction, object position, object size, fluid density and fluid viscosity. As is shown in figure 2.3, drag coefficient for a sphere as a function of Reynolds number Re. The solid line is for a sphere with a smooth surface, while the dashed line is for the case of a rough surface. The numbers along the line indicate several flow regimes and associated changes in the drag coefficient:

- a: Stokes flow and steady separated flow,
- b: transitional separated unsteady flow with a laminar flow boundary layer,
- c: separated unsteady flow with a laminar boundary layer at the upstream side and a chaotic turbulent wake at the downstream of the sphere,
- d: supercritical separated flow.

The Grace drag model in the distorted particle regime is given by:

$$C_D(ellipse) = \frac{4}{3} \frac{g d_B}{U_T^2} \frac{\Delta\rho}{\rho_L} \tag{2.43}$$

where $\Delta\rho = \rho_L - \rho_G$ and U_T denotes bubble terminal velocity.
The Ishii-Zuber correlation gives:

$$\begin{cases} C_D(\text{sphere}) = \frac{24}{Re_B}\left(1 + 0.15 {Re_B}^{0.687}\right) \\ C_D(\text{ellipse}) = \frac{4}{3} d_B \sqrt{\frac{2g\triangle\rho}{\gamma}} \\ C_D(\text{cap}) = \frac{8}{3} \end{cases} \tag{2.44}$$

where γ denotes the interfacial tension between liquid and gas. $Re_B = d_B |U_{\text{slip}}| / \nu_L$ is the bubble Reynolds number, in which d_B denotes the bubble diameter, slip velocity $\mathbf{U}_{\text{slip}} = \mathbf{U}_L - \mathbf{U}_G$, represents the relative velocity of the liquid with respect to the bubble, ν_L is the kinetic viscosity of the liquid.
Consequently, the resulting drag coefficient was taken as

$$C_D = max\{C_D(\text{sphere}), min[C_D(\text{ellipse}), C_D(\text{cap})]\} \tag{2.45}$$

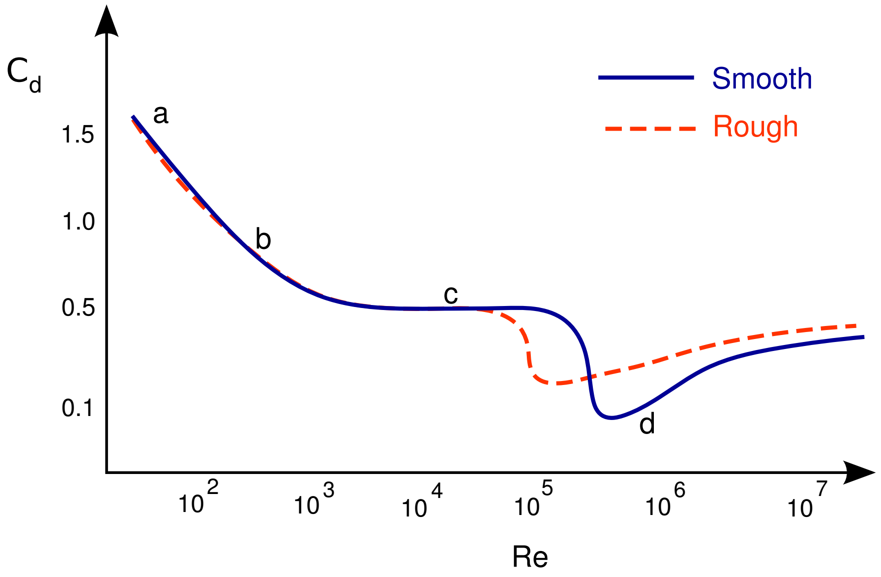

Fig. 2.3: Relationship between drag coefficient and Reynolds number for a sphere [10]

2.3.4 Lift force

A bubble rising in a liquid in the presence of a transverse velocity gradient is subjected to a perpendicular lift force. The lift force, which arises from the shear-induced relative motion in the continuous phase around the bubble, was introduced by Zun [98]. It can be calculated as follows:

$$\mathbf{F}_{L,L} = C_L \alpha_G \rho_L (\mathbf{U}_G - \mathbf{U}_L) \times (\nabla \times \mathbf{U}_L) \tag{2.46}$$

Usually, the lift force coefficient has a positive value, which acts in the direction of decreasing liquid velocity. Numerical [20] and experimental [85] investigations showed that the direction of the lift force change its sign when a substantial deformation of the bubble occurs. As is shown in figure 2.4, the lift force for large ellipsoidal bubble point towards the center, but the lift force changes it sign towards the wall. From experiments on a single bubble,

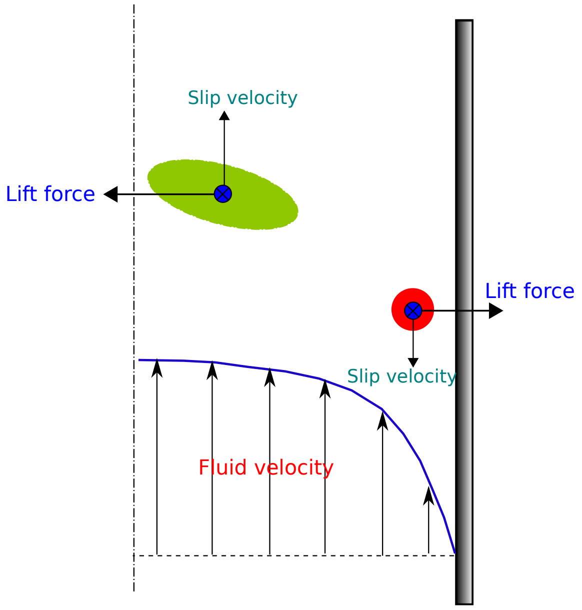

Fig. 2.4: Schematic of lift force in a vertical pipe flow [85]

Tomiyama1995 et al [85] derived the following correlations for the lift coefficient:

$$C_L = \begin{cases} \min\{0.288 + \tanh(0.121Re_B), f(Eo_B)\} & Eo_B < 4 \\ f(Eo_B) & 4 \leq Eo_B < 10.7 \\ -0.27 & Eo_B \geq 10.7 \end{cases} \tag{2.47}$$

with $f(Eo_B) = 0.00105Eo_B^3 - 0.0159Eo_B^2 - 0.0204Eo_B + 0.474$. The Eötvös number of the bubble is defined as

$$Eo_B = \frac{(\rho_L - \rho_G)gd_H^2}{\gamma} \tag{2.48}$$

d_H is the maximum horizontal dimension of the bubble. The empirical correction for the aspect ratio is obtained by Wellek et al [88] with the following equation:

$$d_H = d_B \sqrt[3]{1 + 0.163Eo^{0.757}} \tag{2.49}$$

Investigations by Lucas et al [50, 49, 51] showed that these correlations work well also for poly-disperse flows. Comparing numerical simulation and experiments, Krepper et al [44] concluded that the lift force exerts a damping effect in dense bubble plumes.

2.3.5 Other forces on bubbles

The turbulent dispersion force was introduced in order to account for the random influence of the turbulent eddies in the liquid flow on the dispersed bubbles. The turbulent dispersion force model of [7, Lopez de Bertodano] was chosen

$$\mathbf{F}_{TD,L} = C_{TD}\rho_L k_L \nabla\alpha_L, \tag{2.50}$$

where the turbulent dispersion coefficient is $C_{TD} = 0.1$ and k_L is the liquid turbulent kinetic energy per unit of mass.

In two-phase fluid flows, the virtual mass force is caused by an accelerated motion of the bubble, which displaces the liquid around. It appears as an additional resistance to the bubble motion being proportional to the relative phase accelerations [35].

$$\mathbf{F}_{VM,L} = \mathbf{F}_{VM,G} = \alpha_G\rho_L C_{VM}(\frac{D}{Dt}\mathbf{U}_G - \frac{D}{Dt}\mathbf{U}_L) \tag{2.51}$$

Moreover, the virtual mass force seems important to stabilize the calculation during the early stages of the flow evolution and makes no difference on the final results [74]. Normally, the virtual mass force coefficient C_{VM} is specified to 0.5 by default.

The wall lubrication force is strongly connected with the lateral lift force, which tends to push the dispersed phase away from the wall in a vertical pipe flow. Antal et al [1] proposed a wall lubrication force model as follows:

$$\mathbf{F}_{LUB,L} = -C_{WL}\rho_L\alpha_G|\mathbf{U}_L - \mathbf{U}_G|^2\mathbf{n}_W \tag{2.52}$$

where $\mathbf{n}_W$ is the unit normal pointing away from the wall. The coefficient of wall lubrication force, C_{WL}, is given by

$$C_{WL} = max\{0, \frac{-0.01}{d_B} + \frac{0.05}{d}\} \tag{2.53}$$

Note that y_W, the distance to the nearest wall, is only active in a thin layer adjacent to the wall. By default $C_{WL} = 0$ when $d \geq 5d_B$.

2.3.6 MUSIG model

For simplicity, the gas phase is treated as mono-dispersed phase in a gas-liquid two-phase flow. However, many industrial fluid flow applications involve a two-phase flow with a size distribution. The size distribution of the dispersed phase, including solid particles, bubbles, or droplets, can evolve in a combination of different phenomena like nucleation, growth, dispersion, aggregation, breakage, etc. To model a poly-dispersed flow, a balance equation is required to describe the changes in the particle population, in addition to momentum, mass, and energy balances. A number density function is introduced to account for the particle population in consideration of source or sink terms caused by particles entering and leaving a control volume through different mechanisms:

$$\frac{\partial}{\partial t}n(m,t) + \frac{\partial}{\partial x_i}(U_i(m,t)\cdot n(m,t)) = S_i \tag{2.54}$$

where $n(m,t)$ represents the number density of particles of mass m at time t, S_i is a source term.

The size distribution is discretized into a predefined set of size groups. The relationship between the diameter and the mass of a particular group is defined as:

$$m = \rho_G \frac{\pi d_B^3}{6} \tag{2.55}$$

By means of equal diameter discretization, the diameter of group i is calculated from:

$$d_{B,i} = d_{B,min} + \frac{d_{B,max} - d_{B,min}}{N}(i - \frac{1}{2}) \tag{2.56}$$

where N is the number density of the size group, $d_{B,min}$ is minimum bubble diameter and $d_{B,max}$ is maximum bubble diameter.

The MUSIG (Multiple Size Group) model has been developed to deal with poly-dispersed multiphase flows in Ansys CFX. A homogeneous MUSIG model was firstly proposed by Luo [52], which assumed all size groups for a given poly-dispersed (MUSIG) fluid at the same velocity. The homogeneous model is limited to convection dominated bubbly flows or bubbles with small inertia. To improve the MUSIG model, Krepper et al [45] developed an inhomogeneous MUSIG model where the gaseous phase is allowed to be divided into Nr phase groups with their own velocities.

Defining the size fraction $f_i = \alpha_{G,i}/\alpha_G$, whereby the volume fraction of size group i is $\alpha_{G,i}$. The transport equations for all size fractions of the dispersed phase can be written as:

$$\frac{\partial}{\partial t}(\rho_{G,i}\alpha_G f_i) + \frac{\partial}{\partial x_i}(\rho_{G,i}\alpha_{G,i} f_i) = B_B - D_B + B_C - D_C \tag{2.57}$$

where B_B, D_B, B_C and D_C stand for the birth rate due to breakup of larger particles, the death rate due to breakup into smaller particles, the birth rate due to coalescence of smaller particles, and the death rate due to coalescence with other particles, respectively.

Obviously, the inhomogeneous MUSIG model is capable of dealing with heterogeneous velocity fields of dispersed phase with different size groups at the same time. In the meanwhile it allows sufficient size groups to model the process of coalescence and breakup for dispersed phase, for example, bubbles. In Ansys CFX, the coalescence model of Prince and Blanch [60] is supported. The Prince and Blanch Model assumes that the coalescence of two bubbles occurs in three steps: the collision of bubbles traps a small amount of liquid between them in the form of a liquid film; This liquid film then drains until it reaches a critical thickness; The film ruptures and the bubbles join together. The coalescence kernel is then modeled by

$$Q(m_i;m_j) = (\theta_{ij}^T + \theta_{ij}^B + \theta_{ij}^S)\eta_{ij} \tag{2.58}$$

whereby, m_i and m_j stand for mass of bubble i and j, Q denotes collision rate, η_{ij} is collision efficiency relating to the time, and θ_{ij}^T, θ_{ij}^B, θ_{ij}^S stand for turbulent, buoyancy, and shear contributions to collision frequency, respectively.

For the breakup of bubbles, Luo and Svendson [53] developed a theoretical model based on the theory of isotropic turbulence and probability. The breakup kernel is modeled as:

$$g(m_i;m_j) = 0.923F_B(1-\alpha_G)(\frac{\varepsilon_L}{d_{B,i}^2})^{1/3} \int\limits_{\xi_{min}}^{1} \frac{(1+\xi)^2}{\xi^{11/3}} e^{-\chi} d\xi \tag{2.59}$$

where ξ is the dimensionless size of eddies in the inertial subrange of isotropic turbulence, ε_L is the continuous-phase eddy dissipation rate, F_B is a calibration coefficient, and

$$\chi = \frac{12((m_j/m_i)^{2/3} + (1-m_j/m_i)^{2/3} - 1)\gamma}{2\rho_L \varepsilon_L^{2/2} d_{G,i}^{5/3} \xi^{11/3}}, \tag{2.60}$$

γ is surface tension.

2.4 Modeling of near-wall turbulence

Owing to large velocity gradients and the selective damping of wall-normal velocity fluctuations, wall boundary conditions require special treatment (Fig. 2.5). A wall-function simulation normally requires that y^+ of the first cell outside the walls is in the log-layer, which starts at about $y^+ \sim 20$ and, depending on the Re number, extends up to $y^+ \sim 200$. In the log layer, there is equilibrium between production and dissipation of the turbulent kinetic energy, therefore decreasing turbulent instability in near-wall simulations.

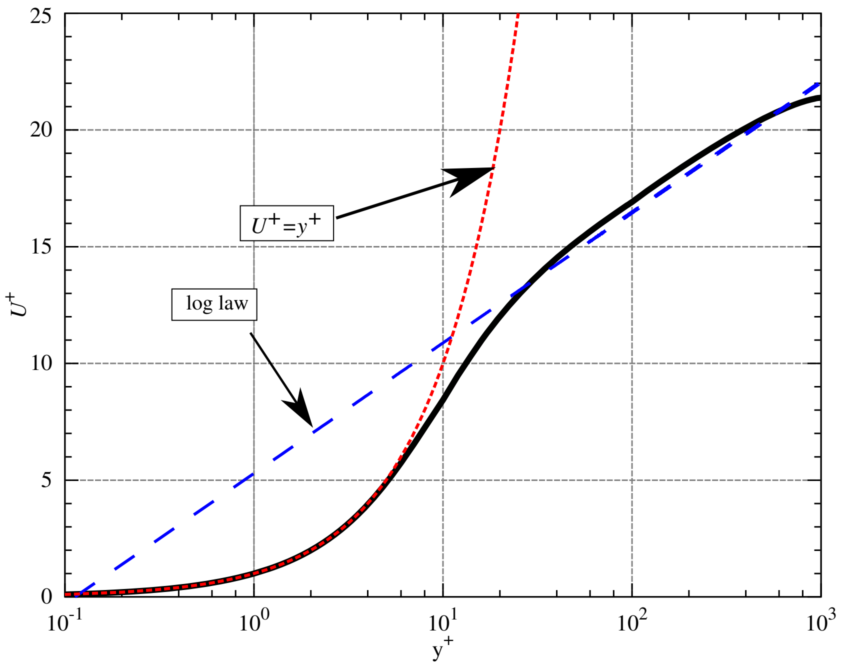

Fig. 2.5: Wall function, i.e. horizontal velocity near the wall with mixing length model

The momentum balance for the near-wall cell requires the wall shear stress $\tau_w (= u_\tau^2)$, which needs some assumption between near-wall and the surface. If the near-wall node lies in the logarithmic region then

$$U^+ = \frac{U_t}{U_\tau} = \frac{1}{\kappa} ln(y^+) + B \tag{2.61}$$

where

$$y^+ = \frac{\rho \Delta y U_\tau}{\mu} \tag{2.62}$$

$$U_\tau = \frac{\tau_\omega}{\rho} \tag{2.63}$$

U^+ stands for the near wall velocity, U_τ represents the friction velocity, U_t denotes the known velocity tangent to the wall at a distance of Δy from the wall, $\kappa \approx 0.41$ is the von Karman constant, B is a log-layer constant depending on wall roughness (~ 5.0 for a smooth wall), y^+ is the dimensionless distance from the wall and τ_ω is the wall shear stress. Δn is the distance between the first and second grid points off the wall. For standard wall function, $\Delta y = \Delta n/4$.
a) Scalable Wall Functions
Obviously the equation 2.35 becomes singular at separation points where the near wall velocity, U_t, approaches zero. An alternative velocity scale, u^* can be used instead of u_τ:

$$u^* = C_\mu^{1/4} k \tag{2.64}$$

Based on this definition, the following explicit equation for u_τ can be obtained:

$$U_\tau = \frac{U_t}{\frac{1}{\kappa} ln(y^*) + B} \tag{2.65}$$

The absolute value of the wall shear stress τ_ω, is then obtained from:

$$\tau_\omega = \rho U^* U_\tau \tag{2.66}$$

where $y^* = (\rho U^* \Delta y)/\mu$, The above scalable wall function can be applied on arbitrarily fine meshes and allows users to perform a consistent mesh refinement independent of the Reynolds number of the application.
The basic idea behind the scalable wall-function approach is to limit the y^* value used in the logarithmic formulation by a lower value of $y^+ = max(y^*, 11.6)$ where 11.06 is the value of y^+ at the intersection between the logarithmic and the linear near wall profile. To use these equilibrium profiles effectively, it is desirable that the grid spacing be such that the near-wall node lies within the logarithmic layer; ideally, $30 < y^+ < 150$, has to be relaxed somewhat in practice, but means that with wall-function calculations the grid cannot be made arbitrarily fine close to solid boundaries.
b) Automatic near-wall treatment
A low-Re simulation using fully resolved boundary layers requires special viscosity-dependent modifications to the turbulence model and refined boundary layer mesh with the first cell at the walls at a value of y^+ less than 1. Stretching of the following cells outside of a wall should usually be kept below something like 1.25 of growth rate. This condition cannot be guaranteed in most applications at walls. For this reason, a new near wall treatment was developed by CFX for the ω based models that allows for a smooth shift from a low-Reynolds number form to a wall function formulation. This near wall boundary condition, named automatic near wall treatment in CFX, is used as the default in all models based on the ω-equation. The flux for the k-equation is artificially kept to be zero and the flux in the momentum equation is computed from the velocity profile. The equations are as follows:
Flux for the momentum equation, F_U:

$$F_U = -\rho U_\tau U^* \tag{2.67}$$

where

$$U^* = \sqrt[4]{(\sqrt{\frac{\mu}{\rho} |\frac{\Delta U}{\Delta y}|})^4 + (\sqrt{\alpha_1 k})^4} \tag{2.68}$$

$$U_\tau = \sqrt[4]{(\sqrt{\frac{\mu}{\rho}|\frac{\Delta U}{\Delta y}|})^4 + (\frac{U}{1/\kappa log(y^+) + B})^4} \tag{2.69}$$

Flux for the k-equation:

$$F_k = 0 \tag{2.70}$$

In the ω-equation, an algebraic expression is specified instead of an added flux. It is a blend between the analytical expression for ω in the logarithmic region and the sublayer region, respectively.

$$\omega_{log} = \frac{U^*}{\alpha_1 \kappa y} = \frac{1}{\alpha_1 \kappa \nu} \frac{U^*}{y^+} \tag{2.71}$$

$$\omega_{sub} = \frac{6\nu}{\beta \Delta y} \tag{2.72}$$

where $\Delta y = \Delta n$. Using this a blending can take the following form:

$$\omega_\omega = \omega_{sub} \sqrt{1 + \frac{\omega_{log}}{\omega_{sub}}}, \tag{2.73}$$

In the low Reynolds number mode, the location of the first mesh point is virtually moved down through the viscous sub-layer as the mesh is refined. Note that the physical location of the first mesh point is always at the wall. However, the first mesh point is treated as if it were $\triangle y$ away from the wall.

2.5 Modeling of magnetic field influence on turbulence

The application of a strong DC magnetic field gives rise to a magnetic dissipation term called as Joule dissipation. The turbulent flow undergoes a reorganization as consequence of the conservation of angular momentum against the background of a continuous decay of turbulent kinetic energy. The structure of the turbulent flow becomes modified considerably, because velocity fluctuations being non-parallel with respect to the magnetic field lines are subjected to the Joule dissipation. As a consequence the turbulent eddies become aligned and elongated along the direction of the imposed magnetic field [76, 14]. It is also clear that the destruction of kinetic energy in the presence of magnetic field is accelerated by Joule dissipation and consequently the contribution of viscosity to the overall damping of the vortex is found to be negligible [78]. Under a weak magnetic field, the behavior of a vortex is complex due to the large ratio of centrifugal forces acting on the vortex to the Lorentz forces. The fluid structure propagates radially outwards like a thermal pump. For the case of a high interaction parameter and a low magnetic Reynolds number, the Joule time (t_m), is small in comparison with the turn-over time of an eddy, $t_0 = L/U$:

$$t_m = \rho/\sigma B^2 \ll L/U, \tag{2.74}$$

so that the interaction parameter, N, is large compared to unity:

$$N = t_0/t_m = \sigma B^2 L/\rho U \gg 1. \tag{2.75}$$

Sommeria and Moreau [76] conducted the vorticity equation of the parallel component z in the following approximate linear form when both interaction parameter and Reynolds number are large:

$$\frac{\partial \omega_z}{\partial t} = -\frac{\sigma B^2}{\rho} \nabla_\perp^{-1} \left(\frac{\partial^2 \omega_z}{\partial z^2} \right) \tag{2.76}$$

The application of the $\nabla_{\perp}^{-1}$ operator is equivalent to multiplication by $-l_{\perp}^{2}$ in Fourier space, where $L_{\perp}$ is the length scale perpendicular to the magnetic field. The length scale parallel to the field, $L_{\parallel}$, is expected to evolve in the form of

$$L_{\parallel} = L_{\perp}(t/t_m)^{1/2} \tag{2.77}$$

According to the above relation, an anisotropic state is attained if a turbulent structure is subject to a magnetic field, wherein

$$L_{\parallel}/L_{\perp} \sim N^{1/2} \tag{2.78}$$

if $L_{\perp}N^{1/2}$ is smaller than the spacing of the walls perpendicular to the imposed magnetic field.

The anisotropy of the Joule dissipation has to be taken into account by the turbulence model which needs an input of information about the dimensionality of the turbulence. Usually, the turbulence can be considered to be 3D and isotropic in most applications, but, a preferred orientation of the turbulent vortices in field direction provokes a quasi-2D character of the turbulent flow field. This reorganization of the flow leads to a remarkable anisotropy of the Reynolds stress which cannot be reproduced by the Reynolds-averaged models.

Generally RANS (Reynolds-Averaged Navier-Stokes) turbulence models do not take into account the damping of turbulence by the magnetic field. Lykoudis and Brouillette [54] proposed damping functions generalized by the Prandtl mixing length concept. Damping functions are added to the algebraic model in consideration of the presence of magnetic field. Equations for the turbulent kinetic energy and its dissipation rate based on two scale direct interaction approximation approach is derived by Shimomura [71]. A consideration of turbulent flows exposed to an external steady magnetic field B requires a completion of the equations for k and ε with sink terms describing the magnetic Joule dissipation. A few studies are known to extend turbulence models to MHD flows in closed channels in a transverse magnetic field [40, 32, 36]. The authors suggested sink terms for k and ε equations in describing the effect of the Joule dissipation in the form of

$$S_{e,k} = C_3\frac{\sigma B_0^2}{\rho}k \tag{2.79}$$

and

$$S_{e,\epsilon} = C_4\frac{\sigma B_0^2}{\rho}\epsilon \tag{2.80}$$

respectively, with the closure constants $C_3 = 0.5$ and $C_4 = 1.0$ in [40].

Unlike the above constant coefficients, Smolentsev et al [75] postulated modifications for C_3 and C_4 as follows:

$$C_3 = 1.9e^{-2.0N} \tag{2.81}$$

and

$$C_4 = 1.9e^{-4.0N} \tag{2.82}$$

Ji and Gardner [36] suggested a modified $k-\epsilon$ turbulence model for a turbulent pipe flow under the action of a transverse magnetic field. Extra terms were incorporated into the equations for k and ϵ in order to modulate the Hartmann effect of the electromagnetic damping. The decay of the turbulent kinetic energy was postulated to be proportional to e^N, whereas N denotes the magnetic interaction parameter. This model is restricted to relatively simple geometries (e.g. pipe or channel flow) and to homogeneous magnetic fields.

The approach was further refined by Kenjeres and Hanjalic [38] proposing a more sophisticated modification of the standard $k-\varepsilon$ model on the basis of the full stress transport equation.

They introduced a local interaction parameter which should reflect the local relation between the characteristic magnetic braking time and the turbulence time scale. It was shown that this modification makes the new model suitable to deal with liquid metal flows in inhomogeneous magnetic fields. Widlund et al [89] proposed a Reynolds stress closure for homogeneous shear-free turbulence exposed to a strong DC magnetic field at low magnetic Reynolds numbers. Therefore, a new scalar dimensionality anisotropy parameter α_μ was introduced which contains important information about the length-scale distribution of vortices showing various orientations with respect to the applied magnetic field. An additional transport equation was implemented to describe the development of the anisotropy parameter on the basis of phenomenological reasoning. The Joule dissipation was integrated into the k-equation as an extra source term with the anisotropy parameter α_μ.
In the present work, we mainly deal with electromagnetic braking in a continuous casting slab mold. Considering the complex geometry and the imposed inhomogeneous magnetic field, the above modified $k-\varepsilon$ turbulence model is not suitable. Therefore, we use a so-called anisotropy variable, α_μ, which was proposed by Widlund et al [89]. Joule dissipation for kinetic energy scales as $(\frac{\lambda_\perp}{\lambda_\parallel})^2\frac{\sigma B_0^2}{\rho}k$, where $\lambda_\perp$ and $\lambda_\parallel$ are characteristic turbulent length scales in the directions parallel and perpendicular, respectively, to the magnetic field. α_μ is proportional to $(\frac{\lambda_\perp}{\lambda_\parallel})^2$. A respective value of $\alpha_\mu = 1/3$ has been selected for isotropic turbulence, whereas it tends to $\alpha_\mu = 0$ in the limit of 2D turbulence. In this case the turbulent structures are expanded along the direction of the magnetic field. The sink source terms for the $SST-k-\omega$ turbulence model are modified and then given by

$$S_{e,k} = \frac{\sigma B_0^2}{\rho}\alpha_\mu k \tag{2.83}$$

$$S_{e,\omega} = \frac{\sigma B_0^2}{\rho}\alpha_\mu \omega \tag{2.84}$$

The value of the anisotropy variable α_μ can be derived from

$$\frac{D\alpha_\mu}{Dt} - \frac{\partial}{\partial x_j}(\nu_t \frac{\partial \alpha_\mu}{\partial x_j}) = C_{\alpha 1}(\frac{1}{3} - \alpha_\mu)\omega - C_{\alpha 2}\frac{\sigma B_0^2}{\rho}\alpha_\mu^2 \tag{2.85}$$

where $C_{\alpha 1} = 0.2$ and $C_{\alpha 2} = 1.74$. The right-hand first term denotes a linear return-to-isotropy term, driving a return to isotropic state ($\alpha_\mu = 1/3$). The right-hand second term stands for magnetic anisotropy, forcing the turbulence towards the two dimensional state ($\alpha_\mu = 0$). $S_{e,k}$ and $S_{e,\omega}$ are added as source terms in k equation and $-\omega$ equation, respectively.
In ANSYS CFX implementation, α_μ is defined as a user scalar variable of the generic form. Source terms are linearized and written (in a cell P) as:

$$S = S_U + S_P\alpha_\mu \tag{2.86}$$

The α_μ is calculated by its transport equation in CFX. The source term for the α_μ transport equation is

$$S_{\alpha_\mu} = S_U + S_P\alpha_\mu = \frac{1}{3}C_{\alpha 1}\omega - (C_{\alpha 1}\omega + C_{\alpha 2}\frac{\sigma_0 B_0^2}{\rho}\alpha_\mu)\alpha_\mu, \tag{2.87}$$

where $C_{\alpha 1} = 0.2$ and $C_{\alpha 2} = 1.74$.
The boundary conditions for α_μ are:

- At Inlet and Outlet, $\alpha_\mu = 1/3$;
- In the solution domain, $\alpha_\mu = 1/3$;
- At walls, zero gradient of α_μ

3 Implementation of mathematical models

In this work, we choose the commercial CFD software ANSYS CFX and the "hypnos" cluster (in HZDR) as a computing platform. CFX software is a high-performance, general purpose fluid dynamics program that is able to be applied to solve wide-ranging fluid flow problems. In particular, it is convenient and flexible to modify or add transport equations by using CFX Expression Language (CEL). Thanks to the cluster in HZDR, all the cases can be run in parallel.

3.1 Finite Volume Method

The finite-volume method (FVM) is widely used in Computational Fluid Dynamics (CFD), which representing and evaluating partial differential equations in the form of algebraic equations. This method is conservative and applicable for general polyhedral finite control volume (CV). ANSYS CFX uses an element-based finite volume method, which first involves discretizing the spatial domain using a mesh. Seeing figure 3.1, the values are stored in cell centers (black dots) and fluxes are calculated at face enters (white dots). In the finite volume method, volume integrals in a partial differential equation that contain a divergence term are converted to surface integrals, using the divergence theorem.

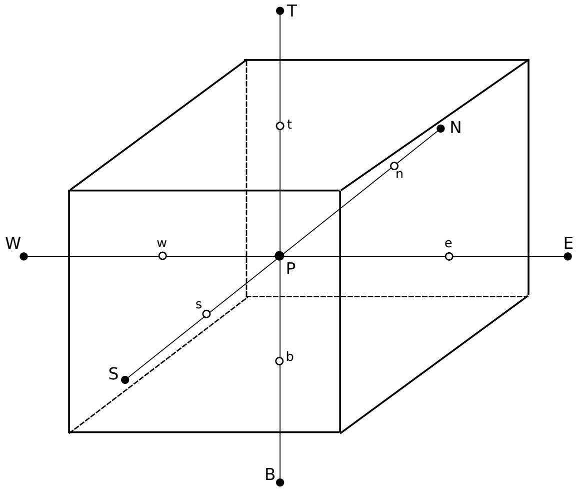

Fig. 3.1: Control volume definition

The conservation equation for the transport of a scalar ϕ in unsteady flow has the general form as:

$$\underbrace{\frac{\partial \rho\phi}{\partial t}}_{\text{transient term}} + \underbrace{\operatorname{div}(\rho\phi u)}_{\text{convection term}} = \underbrace{\operatorname{div}(\Gamma \operatorname{grad}\phi)}_{\text{diffusion term}} + \underbrace{S_\phi}_{\text{source term}} \tag{3.1}$$

Discretization of the transient term in a finite control volume is written as:

$$\int_{CV} \frac{\partial(\rho\phi)}{\partial t} dV = \int_{t-\frac{1}{2}\Delta t}^{t+\frac{1}{2}\Delta t} \frac{\partial(\rho\phi)}{\partial t} dV = \frac{(\rho\phi)^{t+\frac{1}{2}\Delta t} - (\rho\phi)^{t-\frac{1}{2}\Delta t}}{\Delta t} \Delta V \tag{3.2}$$

where, second order backward Euler scheme is chosen and defined as follows:

$$(\rho\phi)^{t+\frac{1}{2}\Delta t} = \frac{3}{2}(\rho\phi)^{t} - \frac{1}{2}(\rho\phi)^{t-\Delta t},$$
$$(\rho\phi)^{t-\frac{1}{2}\Delta t} = \frac{3}{2}(\rho\phi)^{t-\Delta t} - \frac{1}{2}(\rho\phi)^{t-2\Delta t}$$

Discretization of the convective term is:

$$\int_{CV} \frac{\partial(\rho u_i \phi)}{\partial x_i} dV = \oint_S \rho \underbrace{\phi \mathbf{u} \cdot \mathbf{n}}_{\text{convective flux C}} dS = \sum_f \mathbf{S}_f \cdot (\rho \mathbf{u})_f \phi_f \tag{3.3}$$

Discretization of the diffusion term is:

$$\int_{CV} \frac{\partial}{\partial x_i}(\Gamma \frac{\partial \phi}{\partial x_i}) dV = \oint_S \underbrace{\Gamma \nabla \phi \cdot \mathbf{n}}_{\text{diffusive flux D}} dS = \sum_f \Gamma_f \mathbf{S}_f \cdot (\nabla \phi)_f \tag{3.4}$$

Discretization of the source term is:

$$\int_{CV} Q dV = Q_P \Delta V \tag{3.5}$$

There are normally three differencing schemes for the property of ϕ as follows:
The central differencing (CD) scheme is second-order accurate, but unbounded,

$$\phi_f = \overline{fN}/\overline{PN}\phi_P + (1 - \overline{fN}/\overline{PN})\phi_N \tag{3.6}$$

where, the subscript f stands for the face, $\overline{fN}$ is the distance between face f and cell centre N, $\overline{PN}$ is the distance between cell centre P and N, and $\mathbf{S}_f$ is outward face vector.
The upwind differencing (UD) scheme is first-order accurate and bounded,

$$\phi_f = \{ \begin{array}{ll} \phi_P & \text{for } \mathbf{S}_f \cdot (\rho \mathbf{U})_f \geq 0 \\ \phi_N & \text{for } \mathbf{S}_f \cdot (\rho \mathbf{U})_f < 0 \end{array} \tag{3.7}$$

The blending differencing (BD) scheme combines UD and CD in an attempt to preserve the boundedness with reasonable accuracy,

$$\phi_f = (1 - \beta)(\phi_f)_{UD} + \beta(\phi_f)_{CD} \tag{3.8}$$

where β represents the blending coefficient. In ANSYS CFX, the High Resolution Scheme is chosen to calculate convection term, diffusion term, and source term. The High Resolution Scheme uses a special nonlinear recipe for β at each node, computed to be as close to 1 as possible without introducing new extrema. The nodal value for β is taken to be the minimum value of all integration point values surrounding the node and not permitted to exceed 1. ANSYS CFX also uses a co-located (non-staggered) grid layout such that the control volumes are identical for all transport equations to deal with Pressure Gradient term by using Rhie and Chow Pressure-Velocity Coupling method.
In the two-phase fluid model, both of the phases must be continuous, but it is obvious that in a dispersed phase existing in a continuous fluid, the discontinuity appears. Thus, for solving this difficulty, and also to determine which phase is present at a particular point (function of space and time), the phase indicator function $M_k(x,t)$ is defined as:

$$M_k(x,t) = \left\{ \begin{array}{ll} 1 & \text{if phase } k \text{ is found at (x,t)} \\ 0 & \text{otherwise} \end{array} \right. \tag{3.9}$$

It follows that the ensemble averaged phase indication function, summed over all phases, must equal one. Therefore, the volume fraction of each phase can be defined by

$$\alpha_k = \lim_{n\to\infty} \frac{1}{Np} \sum_{n=1}^{Np} (M_k)_n \tag{3.10}$$

where Np is the number of experiments.
Then the weighted-averaging procedures follows that:

- Phase-weighted density $\langle\rho\rangle = \frac{\overline{M_k\rho}}{\overline{M_K}} = \frac{\overline{M_k\rho}}{\alpha_k}$
- Phase-weighted velocity $\langle U_{k,i}\rangle = \frac{\overline{M_k\rho U_i}}{\overline{M_K\rho}} = \frac{\overline{M_k\rho U_i}}{\alpha_k\langle\rho_k\rangle}$
- Phase-weighted electrical potential $\langle\sigma\rangle = \frac{\overline{M_k\sigma}}{\overline{M_K}} = \frac{\overline{M_k\sigma}}{\alpha_k}$

The above definitions show that the volume fraction for dispersed phase (particles, bubbles, droplets...) is obtained by statistical probability and the interface structure is not available after averaging. Averaging also introduces unknown correlations, which must be modeled by phase interaction models, for example, drag force model, lift force model, etc. Moreover, the forces (Lorentz force, drag force, etc.) acting on finite control volume are the results from phase-weighted averaging, then the physical modeling error and the spatial discretization error are unavoidable. Therefore, two-phase MHD flow must be validated before making further simulations, which a non-trival bubble-driven MHD flow was investigated (see Chapter 5 in detail).
Base on the Chapter 2, the mathematical models chosen in this work are given in Table 3.1.

Tab. 3.1: Implementation of mathematical models in CFX

	Single-phase in C.C. (Chapter IV)	Bubbly flow (Chapter V)	Two-phase in C.C. (Chapter VI)
Turbulence model	$SST-k-\omega$	$SST-k-\omega$	$SST-k-\omega$
MHD model	electrical potential method	electrical potential method	electrical potential method
Modification of magnetic field on turbulence	Ola Widlund α_μ model	Ola Widlund α_μ model	Ola Widlund α_μ model
Particle model	···	Homogeneous particle model	Inhomogeneous MUSIG model
Drag force	···	Ishii-Zuber model	Ishii-Zuber model
Lift force	···	Tomiyama lift force model	Tomiyama lift force model
Turbulent dispersion model	···	Lopez de Bertodano model	Lopez de Bertodano model
Wall lubrication force model	···	[1] model	[1] model
Bubble induced turbulent model	···	[73] model	[73] model

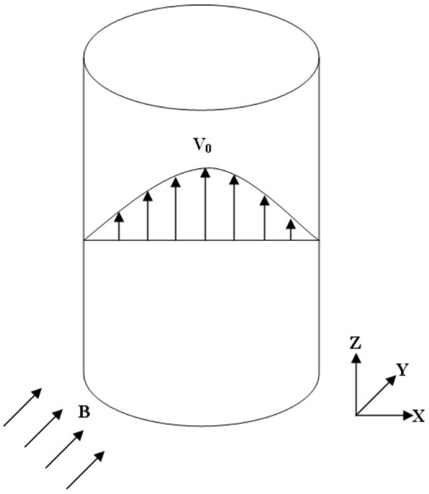

Fig. 3.2: Configuration of test case

3.2 Test of MHD model in CFX

In order to validate the MHD model, one simple case was carried out and implemented in ANSYS CFX. Assuming an electrically conducting fluid flows through a pipe with an inhomogeneous velocity under the consideration of a transverse magnetic field. Fig. 3.2 shows the configuration, where the radius of pipe is $R = 45mm$ and the height is $H = 220mm$. The velocity can be defined by:

$$\mathbf{U} = \left\langle 0, 0, U_0(1 - r^2/R^2) \right\rangle \tag{3.11}$$

and the magnetic field is

$$\mathbf{B} = \langle 0, B_0, 0 \rangle \tag{3.12}$$

In cylindrical coordinate, the variables of velocity and magnetic field were transformed as follows:

$$\mathbf{U} = \left\langle 0, 0, U_0(1 - r^2/R^2) \right\rangle \tag{3.13}$$

$$\mathbf{B} = \langle B_0 \sin\theta, B_0 \cos\theta, 0 \rangle \tag{3.14}$$

Electrical current can be taken in the form of

$$\mathbf{J} = \sigma \left(-\nabla\varphi + \mathbf{U} \times \mathbf{B} \right) \tag{3.15}$$

Therefore, we obtain an electrical potential Laplace equation owing to the source-free property of the electrical current.

$$\Delta\sigma\varphi = \nabla\sigma \left(\mathbf{U} \times \mathbf{B} \right) \tag{3.16}$$

For insulating wall, $\mathbf{J}_n = 0$, which means the electrical current normal to the wall is zero. Therefore, analytical solution of Lorentz force can be derived as follows:

$$F_x = F_y = 0, F_z = \frac{\sigma U_0 B_0^2}{4} \left(\frac{r^2}{R^2} - 1 \right) \cos\theta \tag{3.17}$$

Calculation was performed by CFX with MHD model. The properties of liquid are listed in Table 3.2.

According to the above parameters, the Reynolds number is 100, and the Hartmann numbers are 30 and 60. Consequently the interaction parameter, $N = Ha^2/Re$, are 9 and 36, respectively. It makes clear that the flow in this case is in the laminar regime.

Tab. 3.2: Properties of liquid and geometry

Characteristic length scale	$L = 2R = 0.09m$
Characteristic velocity	$U_0 = 1m \cdot s^{-1}$
Electrical conductivity	σ, is 1 $S \cdot m^{-1}$
Density	1000 $kg \cdot m^{-3}$
Dynamic viscosity	0.9 $kg \cdot m^{-1} \cdot s^{-1}$
Magnetic flux B	10 T and 20 T

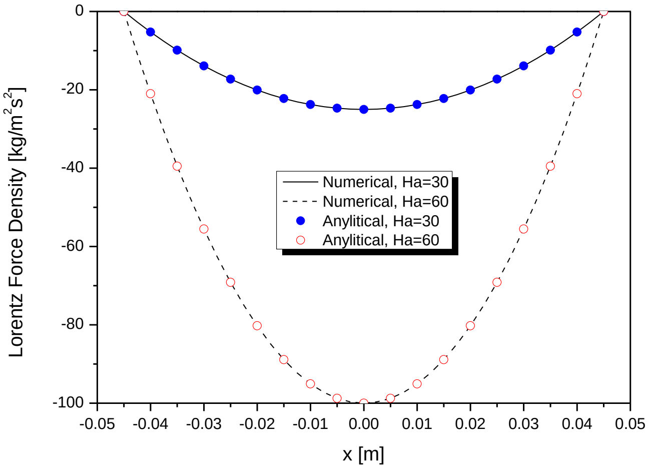

Fig. 3.3: Lorentz force density profile along X-axial at half height

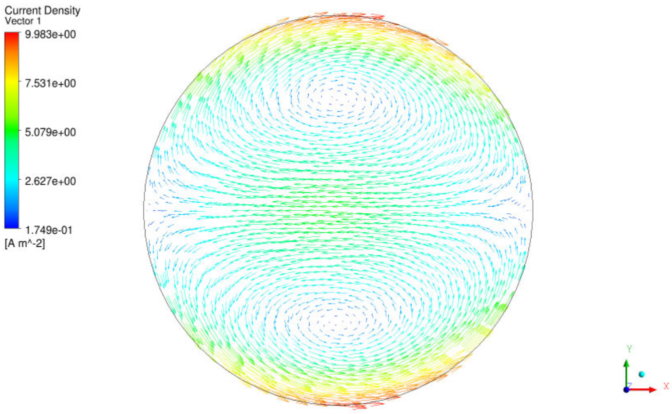

Fig. 3.4: Distribution of electrical current in a cross-section at half height, (left: Ha=30, right: Ha=60)

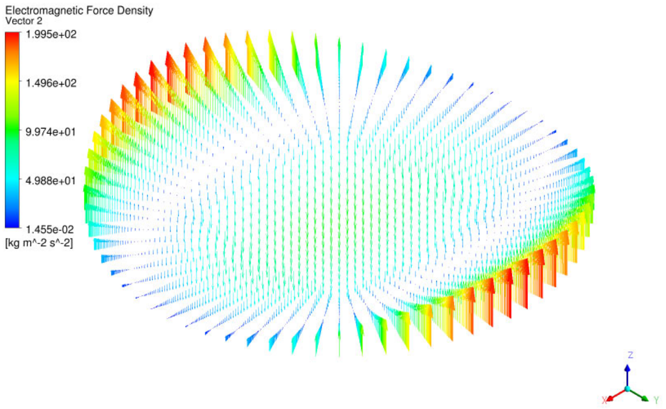

Fig. 3.5: Distribution of Lorentz force in a cross-section at half height, Ha=60

Figure 3.3 shows the Lorentz force profile along x-axial at half height. The numerical result is in very good agreement with the analytical solution at different Hartmann numbers. The distributions of electrical current and Lorentz force in a cross-section at a half height are shown in figure 3.4 and 3.5, receptively. The distribution of electrical current is comparable to Davidson's solution [14]. By taking this simple test, the MHD model in CFX was testified initially. It turns out that the MHD model in CFX is valid.

3.3 Grid sensitivity

As mentioned above, the Hartmann layer is an important property of MHD flows. [6] studied a MHD duct flow with different mesh near the wall and concluded that numerical solutions are consistent with theoretical predictions provided a sufficient resolution is placed in the Hartmann layers attached to the walls. In order to obtain accuracy, finer grids are required. However, finer grid will result with increase in time computing. Thus, optimization of grid size is required to provide an acceptable solution accuracy.

To give a meaningful CFD prediction, numerical uncertainty should first be estimated, especially on the grid sensitivity before making further studies. In this section we discuss numerical results for a MHD duct flow problem which exhibit typical MHD boundary layers: Hartmann layers with the thickness $O(Ha^{-1})$ at the walls perpendicular to the magnetic field, and side layers with the thickness $O(Ha^{-1/2})$ at the parallel walls. Classic "M-shaped" velocity profile is presented caused by a uniform magnetic field.

3.3.1 Configuration of an MHD duct flow

In this grid sensitivity study, a nonconducting rectangular duct is considered with an aspect ratio $L_b/L_a = 1$ (here, L_b is the duct half-height in the magnetic field direction and L_a is the duct half-width perpendicular to the magnetic field), and the ratio of duct length to width is 30. Uniform magnetic field is applied in the direction of height. Reynolds number, Hartmann number and interaction parameter are 90000, 90 and 0.09, namely. The $SST - k - \omega$ model is adopted to calculate the velocity field.

3.3.2 Results and discussion

The distribution of electric current at a cross-section is shown in figure 3.6. With electrically insulating wall, the electric currents separate at $y = 0$ and make closure near the wall. Obviously the electric current is strongly intensified in the region of walls perpendicular to

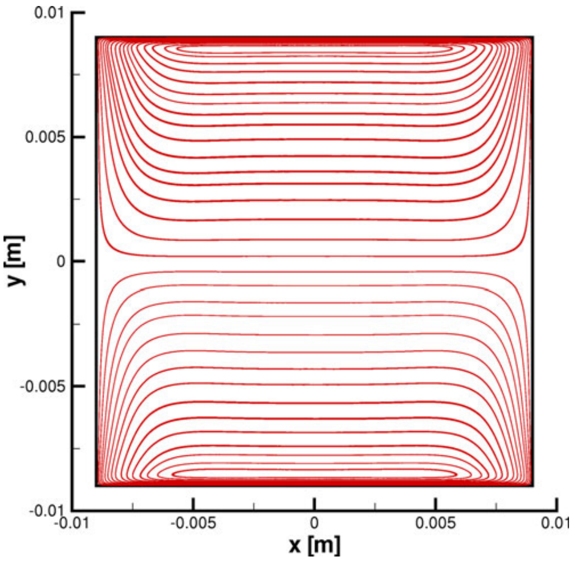

Fig. 3.6: Current distribution at a cross section, electrically insulating wall

the magnetic field. To make a grid sensitivity analysis, y^+ is identified to characterize the grid resolution. Figure 3.7 shows the velocity profiles over the center line perpendicular and parallel to the applied magnetic field, respectively. It was found that the numerical solutions varies with y^+. The case with $y^+ = 1$ is closely approaching to that with $y^+ = 0.01$. For the other cases, the accuracy is not guaranteed. The results indicate that y^+ must be equal to or less than unity in order to remain accuracy when we choose turbulence models to deal with turbulent MHD flow.

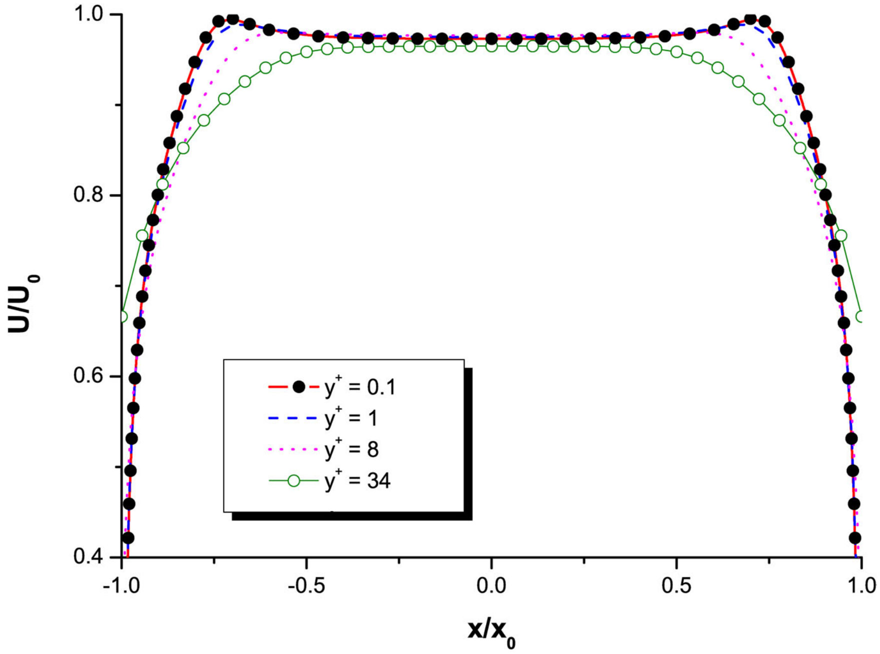

(a) along x-axis

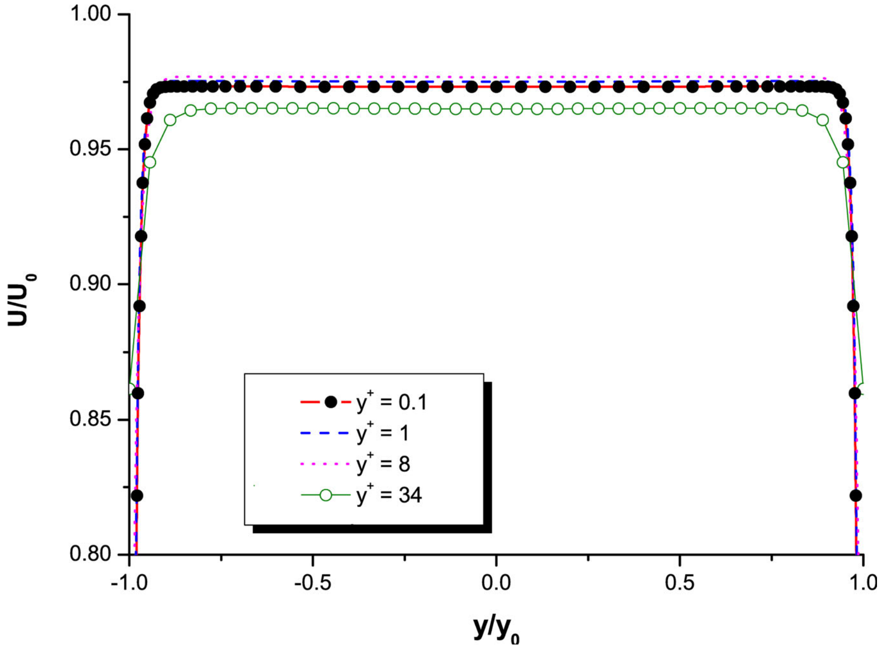

(b) along y-axis

Fig. 3.7: Velocity profiles at center lines at half height

4 Study of the modified turbulence model in a continuous casting slab liquid metal mold

As a first step, we want to focus on the impact of a DC magnetic field on the mean flow pattern and the large energy-carrying structures. Therefore, the URANS-SST $k-\omega$ turbulence model [56] is used within this chapter to calculate the Reynolds stress. In this chapter, firstly we verify the modified turbulence model (Ola Widlund α_μ model) in a continuous casting slab liquid metal mold (mini-LIMMCAST) by comparing with experimental results. Then further investigation on the effect of external static magnetic field on the flow pattern in the mold was carried out with different electrical wall boundary conditions.

4.1 Computational conditions

The geometry of the considered case is on the basis of the Mini-LIMMCAST facility at HZDR (see chapter introduction). Figure 4.1 shows the full scale computational domain, which is divided into ~ 1.2 million hybrid cells. The monitoring points of instantaneous velocity are plotted in figure 4.2. An external static DC magnetic field is applied perpendicular to the wide face, where the magnet pole faces are positioned in the jet zone. As shown in figure 4.3, the distribution of the imposed magnetic flux is almost homogeneous in x direction (mold width from $-0.07\ m$ to $0.07\ m$). The maximum of magnetic flux is located in the jet zone and decayed away from magnet pole face.

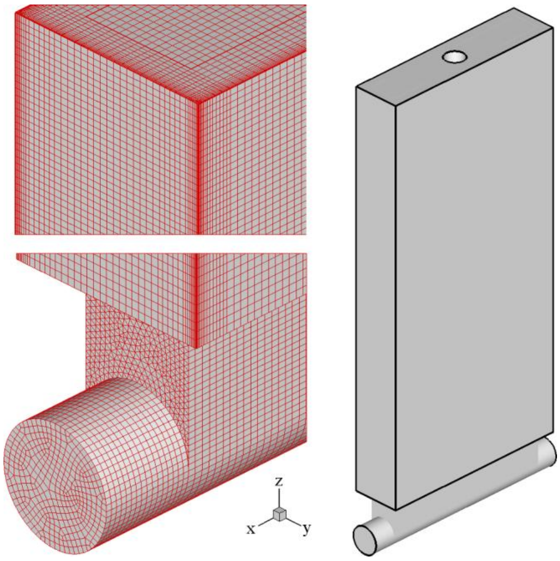

Fig. 4.1: Computational domain and mesh based on the geometry of the mini-LIMMCAST facility

The inlet velocity and turbulence parameters in the solution domain are obtained from the velocity profile which is calculated independently from a previous nozzle flow simulation (flow

rate ~0.11 $L \cdot m^{-1}$). At the free surface, a free-slip wall is specified for simplicity and no-slip wall is assumed for all other walls. At the exit of the domain, the static pressure is zero, and normal gradients of all variables are set to zero.
The boundary condition for the electric potential φ is given by:

$$\frac{\partial \varphi}{\partial n} = (\mathbf{U} \times \mathbf{B})_b \cdot \mathbf{n} \tag{4.1}$$

where the subscript b stands for the boundary and $\mathbf{n}$ is the unit vector normal to the boundary. For an electrically insulating boundary, it gives $\varphi = \varphi_0$, which means that the induced current normal to the wall is zero. For an electrically conducting boundary, the electric current is conserved through the interface between fluid domain and solid domain (shell) in the way that $\frac{\partial \varphi}{\partial n} = \frac{\partial \varphi_b}{\partial n}$.
Even though the thickness of the solidified shell grows along the casting direction in the continuous casting mold, for simplicity, a uniform thickness of solidified shell is assumed for numerical simulations because the maximum magnetic flux is located in the jet area, the thickness of shell is fixed and the wall conductance ratio only varies with the electrical conductivity of shell.
In the case of $N \gg 1$, there is only one possible type of boundary layer, the Hartmann layer, in which the electromagnetic and viscous terms are much larger than the inertial terms. Therefore, it follows $\delta = O(Ha^{-1})$, where δ is a non-dimensional boundary-layer thickness. For example, the Hartmann layer thickness is ~ 0.042 mm when the reference Hartmann number is 417 ($B_0 = 0.31$ T). Moreover, it is rather difficult to define a universal Reynolds number in a continuous casting slab mold. Here, we define three typical Reynolds numbers according to the flow characteristics as follows:

- In the SEN, the characteristic velocity is 1.4 m/s (mean velocity at the inlet), the length scale is 0.01 m, the Reynolds number is 41222, and the boundary layer thickness is approximately equal to 0.25 mm;
- In the jet area, characteristic velocity is 0.4 m/s (bulk velocity), the length scale is 0.01 m, the Reynolds number is 20611, and the boundary layer thickness is approximately equal to 0.61 mm;
- In the computation domain, the characteristic velocity is 0.024 m/s (casting speed), the length scale is 0.177 m (cube root of domain volume), the Reynolds number is 12508, and the boundary layer thickness is approximately equal to 5.23 mm;

In our calculations, the thickness of Hartmann layer is much smaller than the boundary layer thickness. Therefore, the Hartmann layer is considered by fining the mesh near the wide and narrow faces in the mold (see Fig. 4.1).

4.2 Results

4.2.1 Comparison of the Time-Averaged Flow

In a first step, we examine the spatial structure of the time-averaged velocity field. A specific processing and adaptation of the numerical data was necessary to allow for a suitable comparison between the numerical results and corresponding experiments where a line array of ten ultrasonic transducers was used with a distance of 10 mm between two adjacent sensors. As can be see in figure 4.4, the dark rectangle is the mapping area of UDV. The two-dimensional contour plots of the velocity field in a half mold as shown in the figures 4.5 through 4.9 for the x-z plane at y = 0 have been obtained by an interpolation process based on the data along the ten measuring lines.

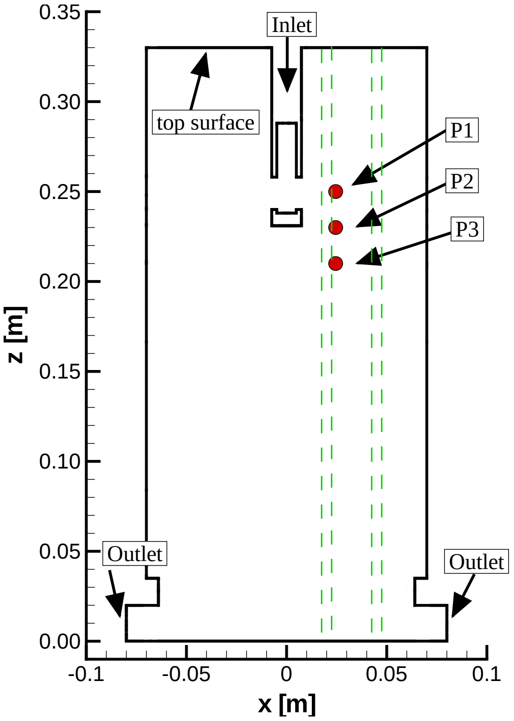
Inlet
top surface
P1
P2
P3
Outlet
Outlet
z [m]
x [m]
0.35
0.30
0.25
0.20
0.15
0.10
0.05
0.00
-0.1
-0.05
0
0.05
0.1

Fig. 4.2: Monitoring positions and spatial-averaging regions in which instantaneous vertical velocities are evaluated in the midplane between widefaces. (Dashed lines are boundaries of the cylindrical UDV measurement regions, $x = 0.02\ m$ and $x = 0.045\ m$): p1 ($0.0245\ m$, $0\ m$, $0.25\ m$), p2 ($0.0245\ m$, $0\ m$, $0.23\ m$), p3 ($0.0245\ m$, $0\ m$, $0.21\ m$)

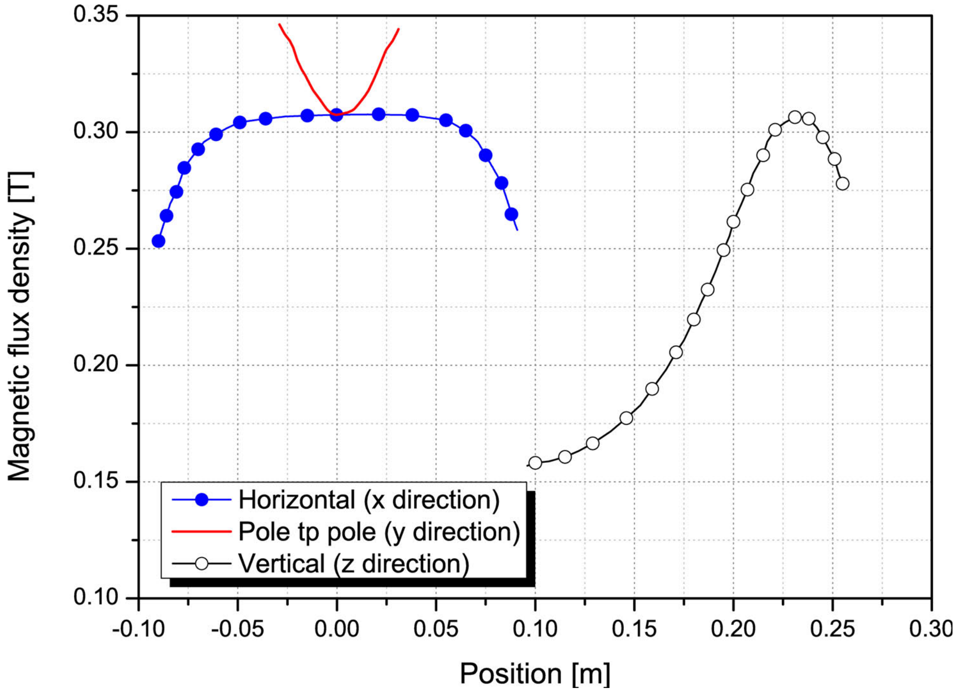

Fig. 4.3: Plots of the imposed external static magnetic fields for calculations in the mold, $B_0 = 0.31\ T$

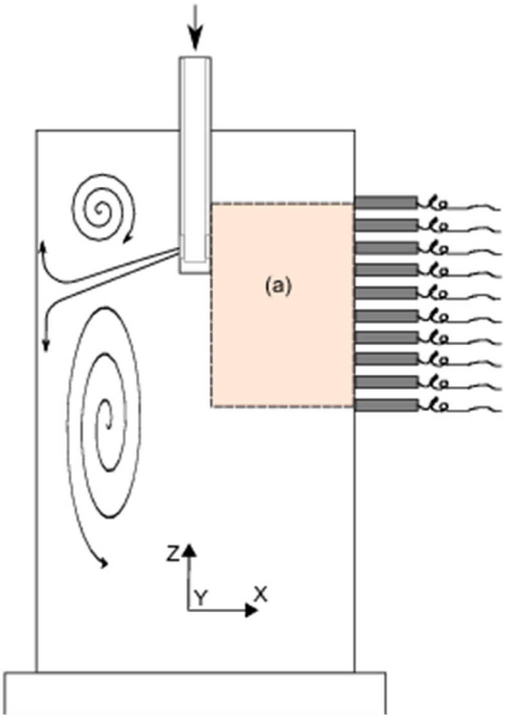

Fig. 4.4: Mapping area of UDV and position of transducers in mini-LIMMCAST mold, (a) mapping area from $z = 0.18\ m$ to $z = 0.27\ m$

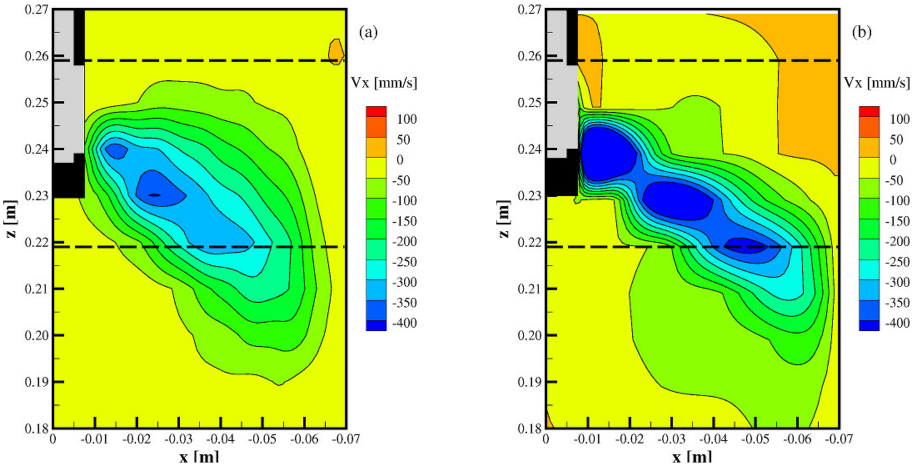

(a) experimental result

(b) numerical simulation

Fig. 4.5: Contour plots of the time-averaged horizontal velocity in the midplane parallel to the mold wide face without any applied magnetic field

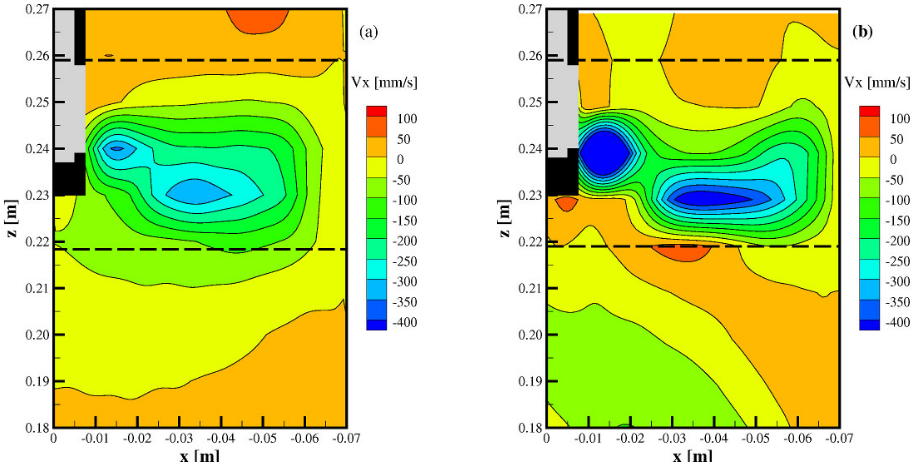

(a) experimental result

(b) numerical simulations using a modified turbulence model

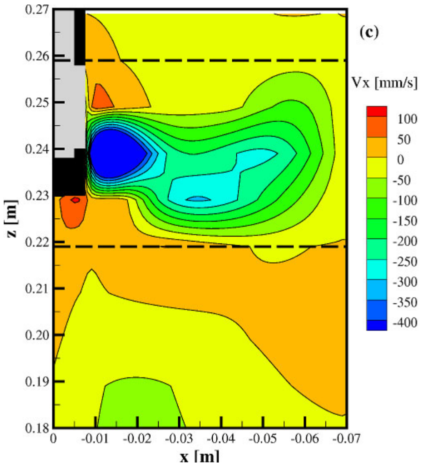

(c) numerical simulations using $SST-k-\omega$ without modification

Fig. 4.6: Contour plots of the time-averaged horizontal velocity in the midplane parallel to the mold wide face with electrically insulating mold walls, $B_0 = 0.31\ T$ (within the dotted lines)

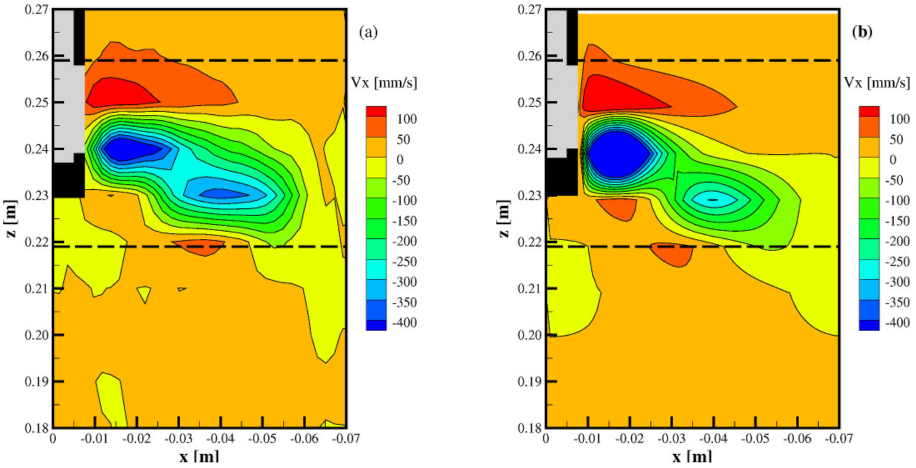

(a) experimental result

(b) numerical simulations using a modified turbulence model

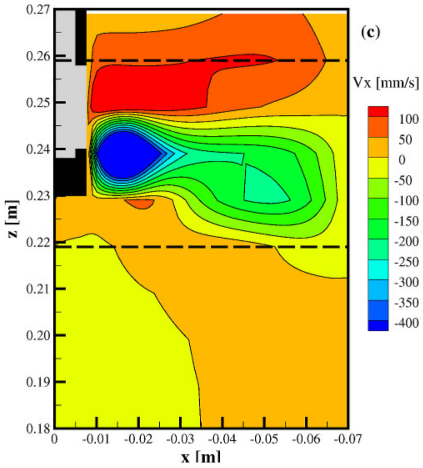

(c) numerical simulations using $SST - k - \omega$ without modification

Fig. 4.7: Contour plots of the time-averaged horizontal velocity in the midplane parallel to the mold wide face with electrically conducting mold walls, $B_0 = 0.31\ T$ (within the dotted lines)

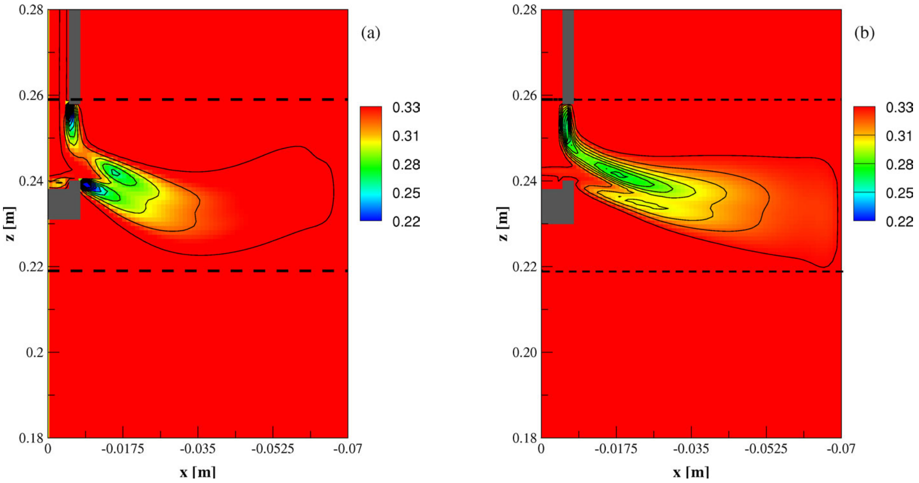

(a) electrically insulating wall

(b) electrically conducting wall

Fig. 4.8: Contour plots of the time-averaged α_μ in the midplane parallel to the mold wide face, $B_0 = 0.31\ T$

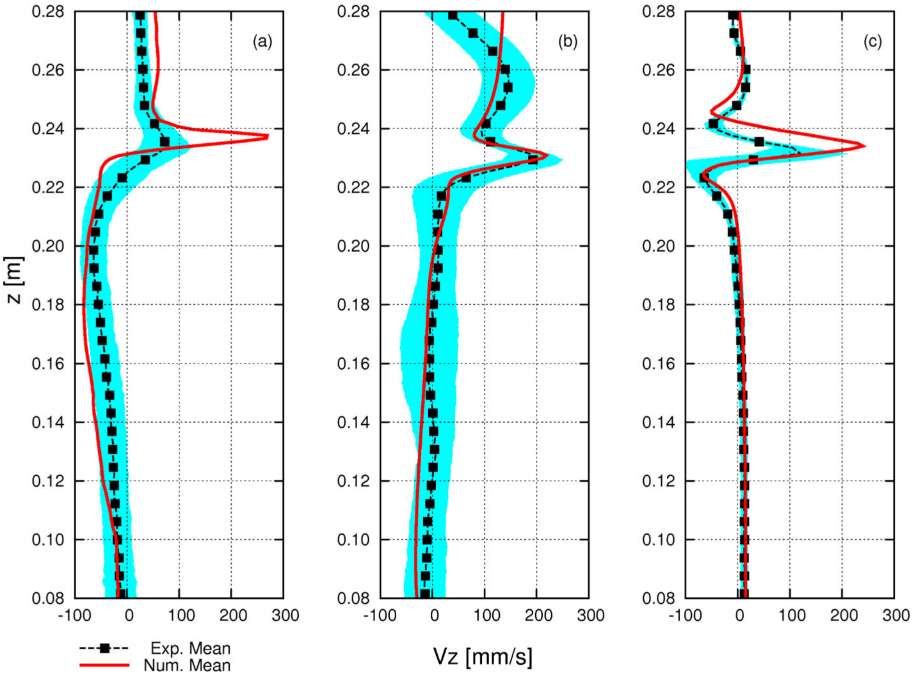

Fig. 4.9: Profiles of the time-averaged vertical velocity along a vertical line in the midplane at $x = 0.02$ m: (a) $B_0 = 0$; (b) $B_0 = 0.31$ T, insulating mold; and (c) $B_0 = 0.31$ T, conducting mold (solid line: numerical results; points: experimental data filled in the values of the minimum and maximum)

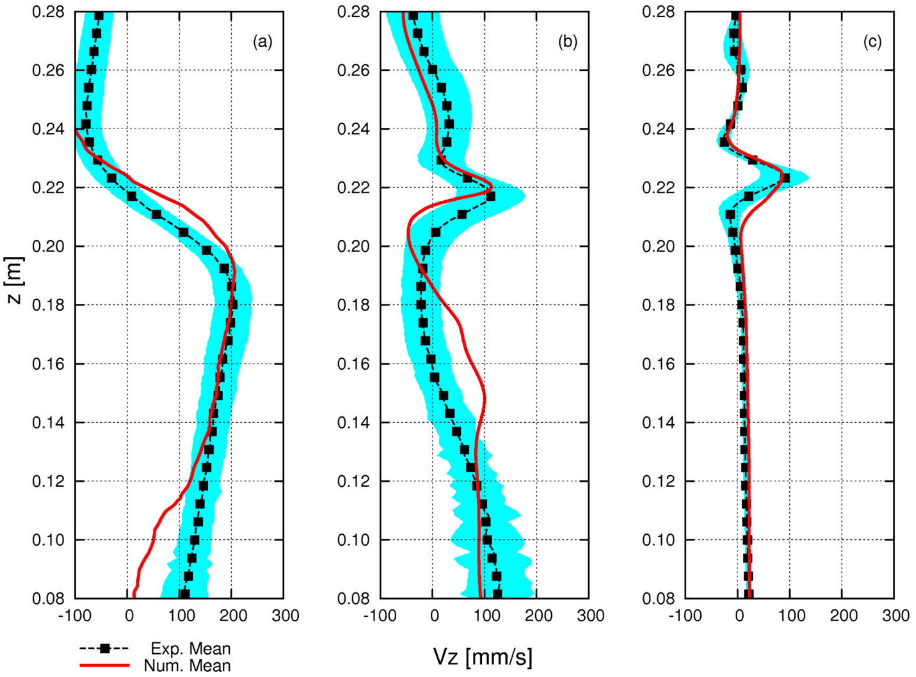

Fig. 4.10: Profiles of the time-averaged vertical velocity along a vertical line in the midplane at $x = 0.045$ m: (a) $B_0 = 0$ T; (b) $B_0 = 0.31$ T, insulating mold; and (c) $B_0 = 0.31$ T, conducting mold (solid line: numerical results; points: experimental data filled in the values of the minimum and maximum)

As a consequence, some artifacts occur in the flow pattern, typically with respect to the imperfectness of the specific measuring configuration. In particular, the measured flow velocity near the SEN port is smaller than the numerical results for all the cases. Contour plots of the horizontal velocity component are presented for three different situations: the discharged jet without magnetic field (figures 4.5), the application of a magnetic field of 0.31 T within an electrically insulating mold (figure 4.6), and the magnetic field of the same strength in an electrically conducting mold (figure 4.7). The figures show a good agreement between numerical simulation and flow measurements except that the numerical flow velocity is overestimated compared with the experimental data. This may be cause by the divergence of the ultrasound transmitting in liquid metal. The angle of the jet, which becomes flatter under the magnetic field influence, matches well for all the cases. Strong recirculation zones appear above the jet region in an electrically conducting mold (figure 4.7), whereas the simulations give a better prediction if the anisotropy of the MHD turbulence is incorporated into the model. Moreover, the electrically conducting wall promotes a braking of the velocity inside the jet, whereas the weakening of the flow becomes more pronounced in the numerical results. The corresponding distribution of the time-averaged value α_μ in the midplane across the wide face is contoured in figure 4.8. Obviously the change of α_μ is confined to the jet area for both electrically insulating wall and electrically conducting wall.

To make further comparison, corresponding profiles of the vertical velocity component at $x = 0.02$ m and $x = 0.0455$ m are shown in figure 4.9 and 4.10, respectively. In general, a comparison of the calculated results with the UDV flow measurements yields a sufficiently good coincidence. However, at $x = 0.02$ m (closer to SEN) the numerical results are larger than the experimental data in the jet area. The blue fringes around the curves represent the standard deviation of the time-averaged velocity values. It is interesting to note that fluctuations of the flow field in the lower part of the mold seem to be significantly tranquilized in case of an electrically conducting wall. Another analysis is especially focused on the observed variations of the velocity fields appearing under different electrical boundary conditions within the mold.

4.2.2 Influence of Magnetic Field Intensity

The differences of the flow pattern in the mold occurring under various magnetic field conditions become apparent by drawing the time-averaged velocity streamlines in figures 4.11 and 4.13. As shown in figure 4.11(a) for the absence of any magnetic field, the liquid metal jet discharged from the SEN ports impinges on the narrow faces and splits into upward and downward flows forming two recirculation regions: an upper vortex between jet and meniscus and a lower-recirculation region, which generates a reversed flow toward the SEN around the mold center line. A rising magnetic flux for the electrically insulating wall causes an increasing deformation of the lower recirculation zone (figures 4.11(b) through 4.11(d)). In case of the maximum magnetic field, the typical double-roll flow pattern is replaced by a new flow structure. The original lower recirculation zone is shifted downward, and extra smaller vortices appear just below the SEN at higher magnetic field strengths. Figure 4.12 presents horizontal profiles of the vertical velocity component below the magnetic field position for the nonconducting case. The imposition of the magnetic field reduces the vertical velocity at the mold center. Further increase of the field strength leads to an inversion of the flow direction corresponding to the formation of the new vortex pair as shown in figure 4.11(d).

Significant changes of the flow pattern from the magnetic field impact can also be observed in figure 4.13, where the case of the electrically conducting wall is displayed. The size of the recirculating rolls is significantly compressed to regions close to the SEN ports. The velocity field below the SEN tends toward a plug flow at the highest magnetic field strength. It is worth noting that the magnetic field considerably changes the flow at the free surface. A small

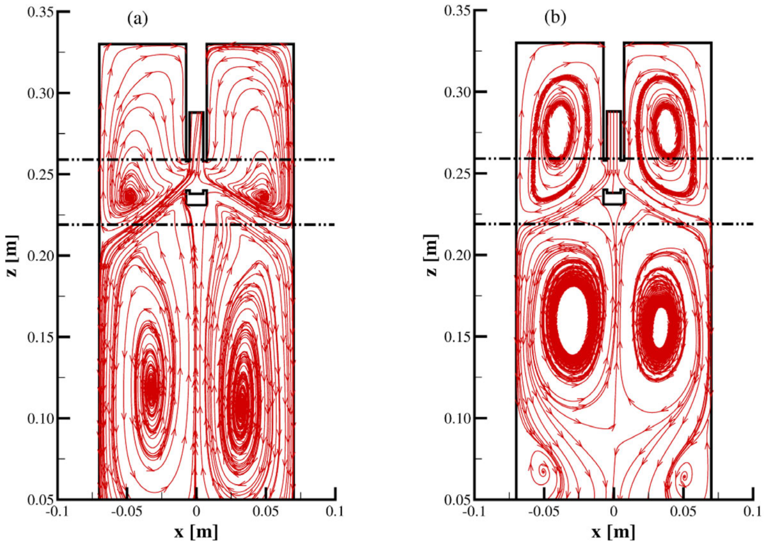

(a) $B_0 = 0$ (b) $B_0 = 0.11\ T$

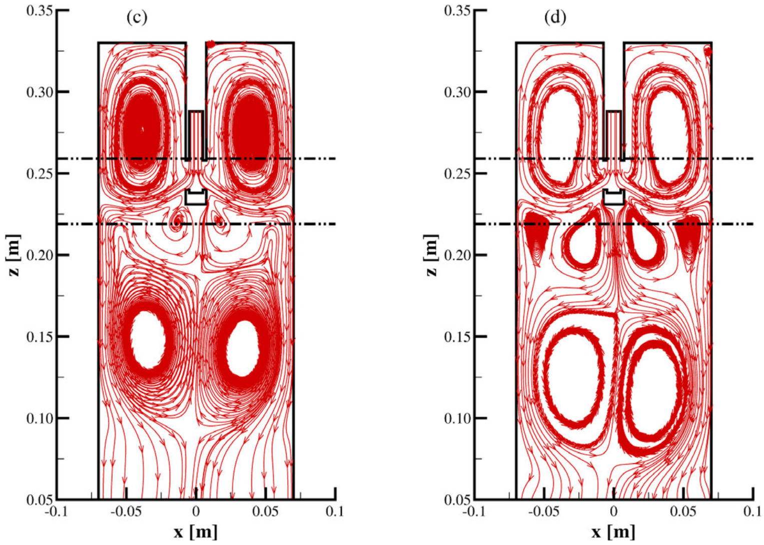

(c) $B_0 = 0.21\ T$ (d) $B_0 = 0.31\ T$

Fig. 4.11: Streamlines of the time-averaged velocity in the midplane parallel to the mold wide face with electrically insulating walls obtained from numerical simulations using a modified turbulence model

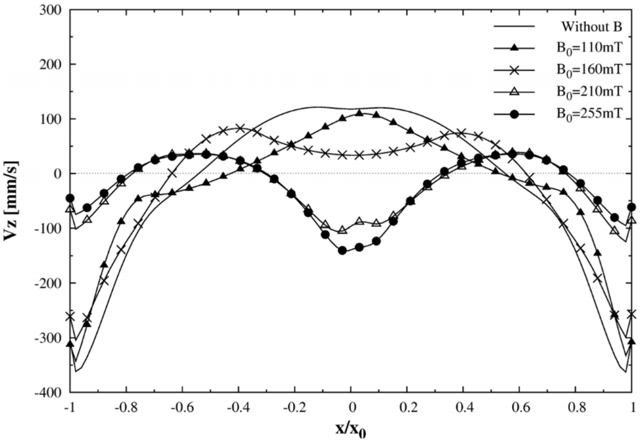

Fig. 4.12: Profiles of the time-averaged vertical velocity at different magnetic field intensities in an electrically insulating mold; data were recorded along a horizontal line in the midplane parallel to the mold wide face at $z = 0.018\ m$

counter-rotating vortex appears close to the SEN at moderate field intensities (figure 4.13(b)). A subsequent increase of the field strength causes a reversal of the flow direction near the free surface by an expansion of this vortex over the entire mold cross section.

The three-dimensional distributions of the induced electrical currents are plotted in figure 4.14 for both situations of an insulating and a conducting mold wall at a magnetic field strength of 0.31 T. If the wall is nonconducting, then the closure of the current loops occurs in a large volume between the discharging jet zones at both sides of the nozzle (figure 4.14(a)). Otherwise, the main part of electric currents in figure 4.14(b) runs through the conducting mold walls. The closure of the induced currents is basically determined by the electrical resistance along the current path. In case of the nonconducting wall, the electrical currents may close through the Hartmann layers, too. The electrical resistance of the Hartmann layers, however, is determined by their thickness δ, which scales with Ha^{-1}. The Hartmann layer thickness becomes quite small at the maximum magnetic field intensities considered in this work (0.04 mm at $Ha = 417$). This effect reduces the effective cross section of the back circuit of the electrical current and causes a relative large electrical resistance. Obviously, in the case considered in figure 4.14(a), the closure of the induced currents becomes more favorable in the bulk fluid between the two jets.

A more detailed view of the electrical current densities provides figure 4.15 showing a 2-D distribution in a y-z cross section at $x = 0.0245\ m$. In the case of the insulating wall (figure 4.15(a)), the induced currents pass through the center of the jet and distribute over a wide region above the jet. A minor part of the current closes through the Hartmann layers, causing a higher density of electrical current in the vicinity of the wall. In the other case, the current flows directly through the conducting mold wall (figure 4.15(b)). The resulting current loops are considerably smaller and are almost restricted to the zone around the jet. As a consequence, the Lorentz force should exhibit a higher concentration there. Figure 4.16 displays the distribution of the corresponding electric potential, which widely spreads over the upper part of the mold in case of a nonconducting mold (figure 4.16(a)), whereas a clear restriction to the jet zone becomes obvious for electrically conducting walls (figure 4.16(b)).

As is well-known, if the flow is irrotational and the line element is perpendicular to a streamline, the velocity potential is constant along lines perpendicular to streamlines, so that the velocity potential decreases in the direction of flow just as the electrical potential decreases in the direction in which the current flows. As a consequence, the distribution of electrical potential is similar to the streamlines of the fluid flow.

The intensity and the path of the induced electrical currents have a distinct influence on the

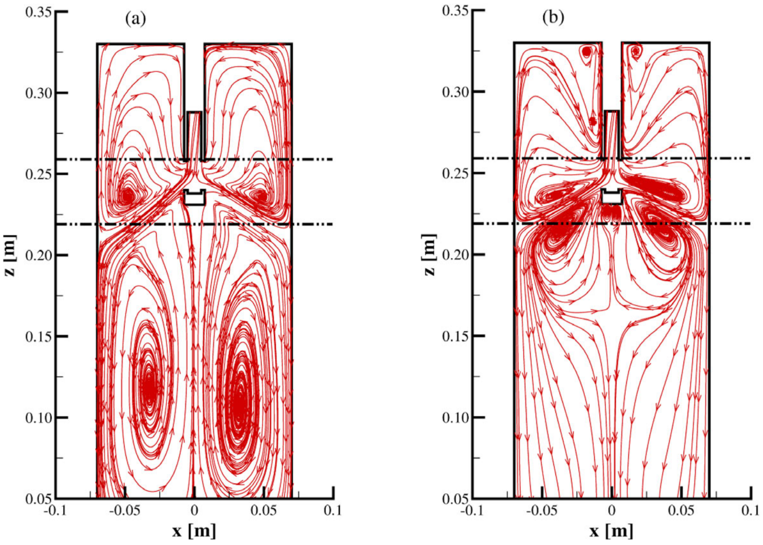

(a) $B_0 = 0$ (b) $B_0 = 0.11\ T$

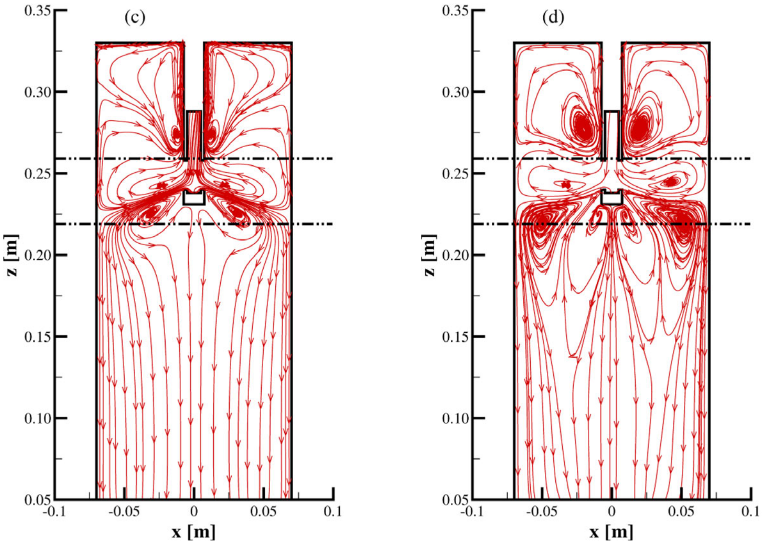

(c) $B_0 = 0.21\ T$ (d) $B_0 = 0.31\ T$

Fig. 4.13: Streamlines of the time-averaged velocity in the midplane parallel to the mold wide face with electrically conducting walls obtained from numerical simulations using a modified turbulence model except for (c) where the common RANS model was used

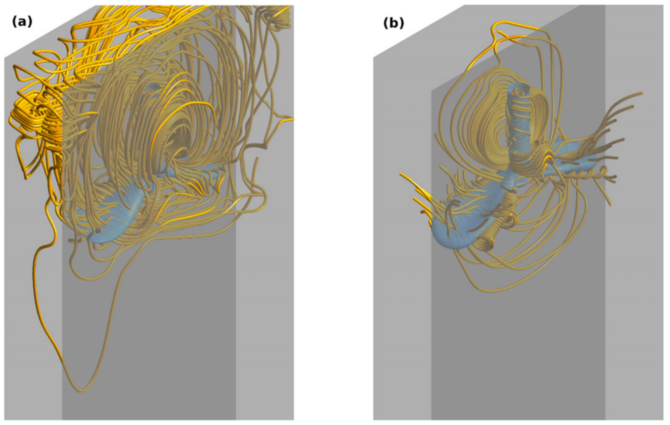

(a) insulating mold, $C_W = 0$

(b) conducting mold, $C_W = 0.133$

Fig. 4.14: 3-D distribution of the induced electrical currents around the jets discharging from the SEN, EMBr ruler ($B_0 = 0.31\ T$)

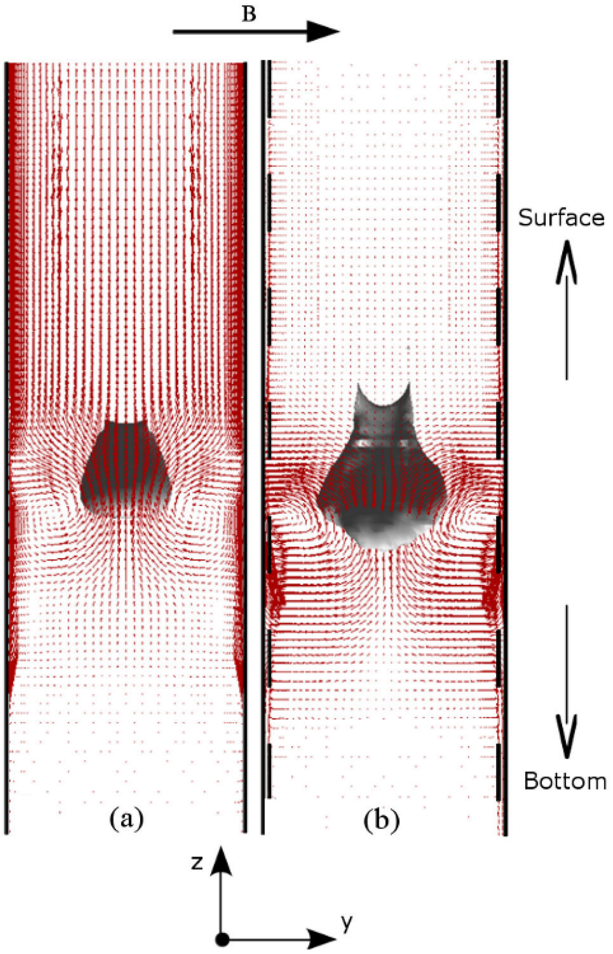

Fig. 4.15: 2D distribution of the induced electrical currents in a $y - z$ cross-section at $x = 0.0245\ m$, EMBr ruler ($B_0 = 0.31\ T$): (a) insulating mold, $C_W = 0$ and (b) conducting mold, $C_W = 0.133$. Dashed line stands for the interface between the mold and the inserted brass plates. The jet position is indicated by the gray insert represented by a velocity isosurface at $0.4\ m/s$

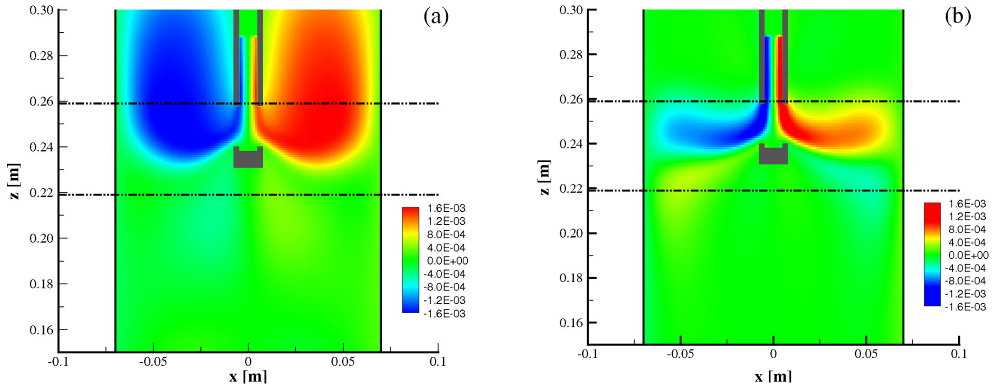

Fig. 4.16: Distribution of the electrical potential in the midplane parallel to the wide face, EMBr ruler ($B_0 = 0.31\ T$): (a) insulating mold, $C_W = 0$ and (b) conducting mold, $C_W = 0.133$

resulting Lorentz force, which is compared in figures 4.17 and 4.18 for both the situation of the insulating and electrically conducting boundary conditions. The two dashed lines denote the magnetic pole faces. The differences seem to be small in the midsection of the mold, but the deviations in regions near the wall are remarkable. Figures 4.17(b) and 4.18(b) display the situation inside the Hartmann layers wherein the Lorentz force is aligned with the flow direction. The effect of the electromagnetic force remains focused on the fluid region between the pole faces of the magnetic field for the conducting mold. The nonconducting case reveals a perceptible force action also in the upper part of the mold provoked by the closure of the induced currents in this region. Note that the magnetic field decays outside the magnet pole face region (see Fig. 4.3), but it is still strong enough in the fluid field regions to cause relevant Lorentz forces there.

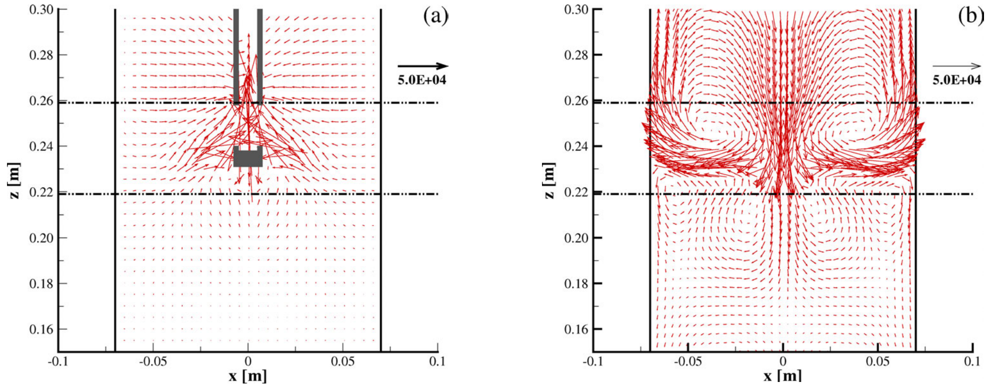

Fig. 4.17: Distribution of the Lorentz force for the case of an electrically insulating mold wall, $B_0 = 0.31\ T$: (a) in the midplane, $y = 0$ and (b) near the wall, $y = 0.0174\ m$

4.2.3 Fluctuations of the Mold Flow

The following section is devoted to the properties of the transient flow. Time series of the horizontal velocity obtained both by numerical simulations and flow measurements at a position inside the jet ($x = 0.0245\ m$, $y = 0$, and $z = 0.23\ m$) are displayed in figure 4.19. The experimental data were recorded at a scan rate of 90 Hz. For a clearer depiction, all the results shown here were filtered with a respective low-pass filter. The negative values of the velocity stand for the flow direction toward the narrow face. The time series in figure 4.19 indicate a turbulent flow, whereas the amplitudes of the velocity fluctuations found in the experiment are well recovered by the numerical simulations after 0.2s FFT filter. It is apparent

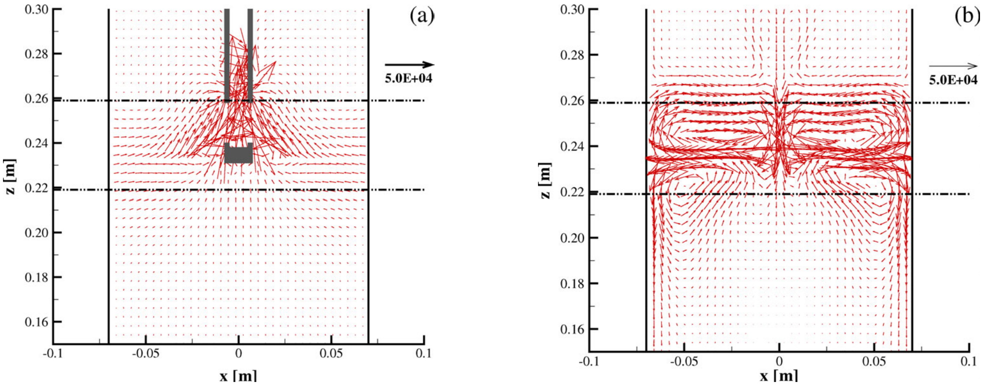

Fig. 4.18: Distribution of the Lorentz force for the case of an electrically conducting mold wall, $B_0 = 0.31\ T$: (a) in the midplane, $y = 0$ and (b) near the wall, $y = 0.0174\ m$

that turbulent fluctuations (high frequency) was damped out owing to URANS turbulence model, because $SST - k - \omega$ turbulence model models the turbulence at all scales. Therefore $SST - k - \omega$ turbulence model fails to capture turbulence with high frequency, however it is possible to obtain flow fluctuations with lower frequency.

Corresponding velocity time series for a magnetic field of 0.31 T in the electrically insulating mold are presented in figure 4.20. Obviously, under such conditions, the magnetic field has not the ability to suppress the turbulent flow. Distinct velocity fluctuations survive, and especially the low-frequency oscillations become even stronger (note the different scaling of the velocity scale). This tendency was also predicted by our numerical calculations regardless whether the anisotropy variable α_μ has been included into the turbulence model. The further comparison is shown in figure 4.21. It is apparent from figure 4.21 that the calculation with turbulence modification gives a better prediction in both amplitude and frequency. The tendency towards oscillation is caused by electromagnetic damping. When the EMBr system switches on, the typical double-roll flow pattern is changed. In the lower recirculation region, the large eddies are squeezed and become smaller by the electromagnetic damping so that the lower eddies detached from the narrow faces and the bottom. The evolution of two quasi-free eddies has a tendency to be unsteady and deformed, leading to an asymmetric flow.

Figure 4.22 shows corresponding snapshots of the two-dimensional flow field at $y = 0$. The time series presented previously were recorded at the location which is marked by the red spot. It becomes obvious that the strong velocity fluctuations observed in figure 4.20 are related to remarkable oscillations of the jet position. The same phenomenon has already been reported in the preceding experimental study [83]. Moreover, the numerical simulations show a reciprocal deflection of both jets discharging at the left and right side of the nozzle, respectively. This has been proven by further flow measurements using two ultrasonic sensors adjusted at the opposite sides of the narrow mold face. This setup allows for a simultaneous acquisition of the horizontal velocity profiles for both jets at a height of $z = 0.225\ m$.

The situation in the electrically conducting mold with a field strength of 0.31 T is shown in figure 4.23. Three different positions are considered in this figure: above the discharged jet (figure 4.23(a)), within the jet (figure 4.23(b)), and below the jet (figure 4.23(c)). The flow measurements reveal remaining velocity fluctuations at all three locations that are the strongest inside the jet. It becomes evident that this phenomenon cannot be captured by the numerical simulations as long as the anisotropy of the MHD turbulence is not considered in the turbulence model. The conventional model without anisotropy factor α_μ spuriously predicts an almost complete suppression of the turbulent flow. By contrast, the turbulent velocity fluctuations reproduced by means of the MHD turbulence model are of the same magnitude as found in the experiments. The positive horizontal velocities observed above the

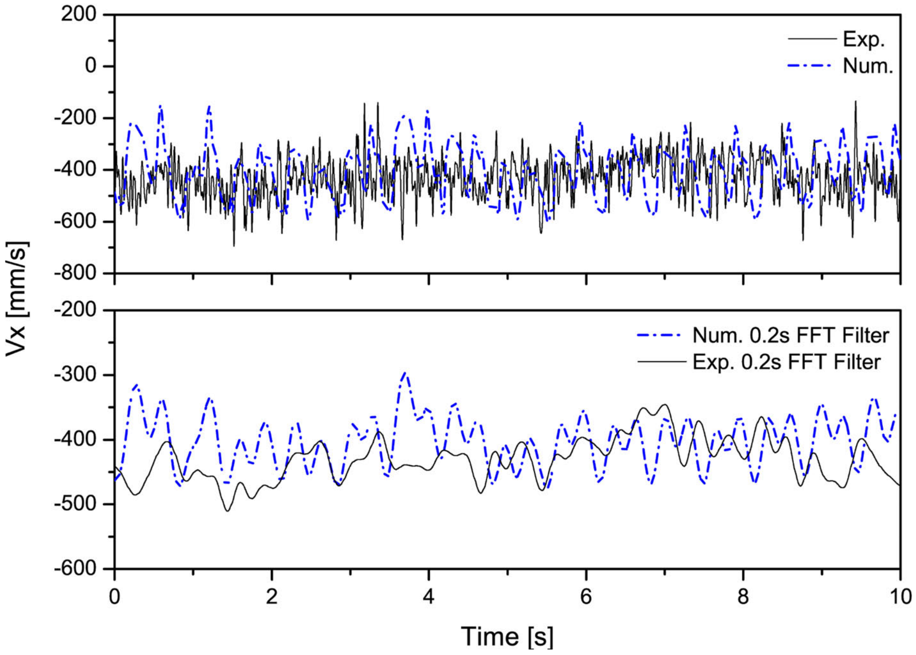

Fig. 4.19: Time series of the instantaneous horizontal velocity without magnetic field at the position P2

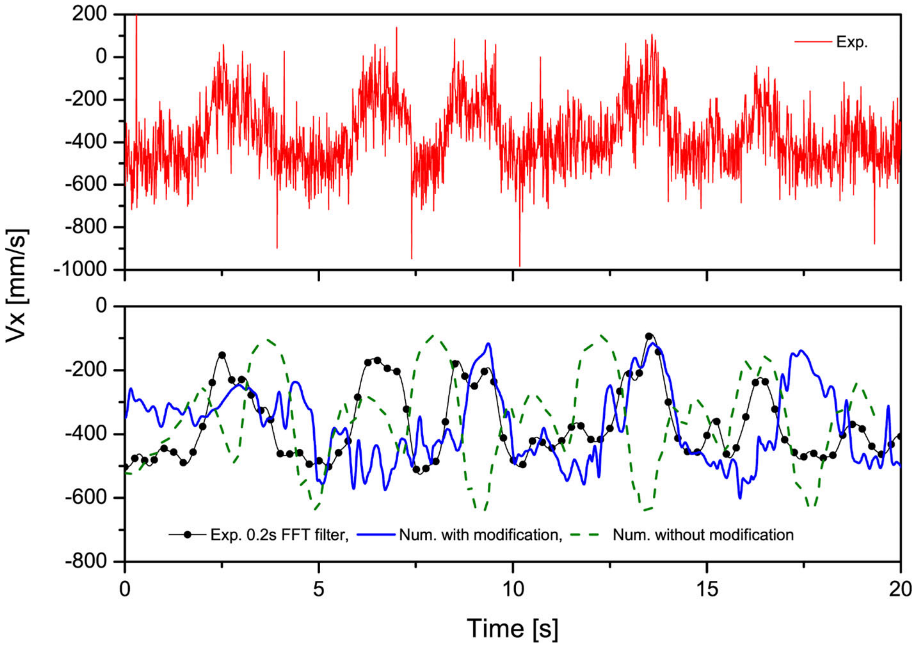

Fig. 4.20: Time series of the instantaneous horizontal velocity for $B_0 = 0.31\ T$ in the electrically insulating mold at the position P2

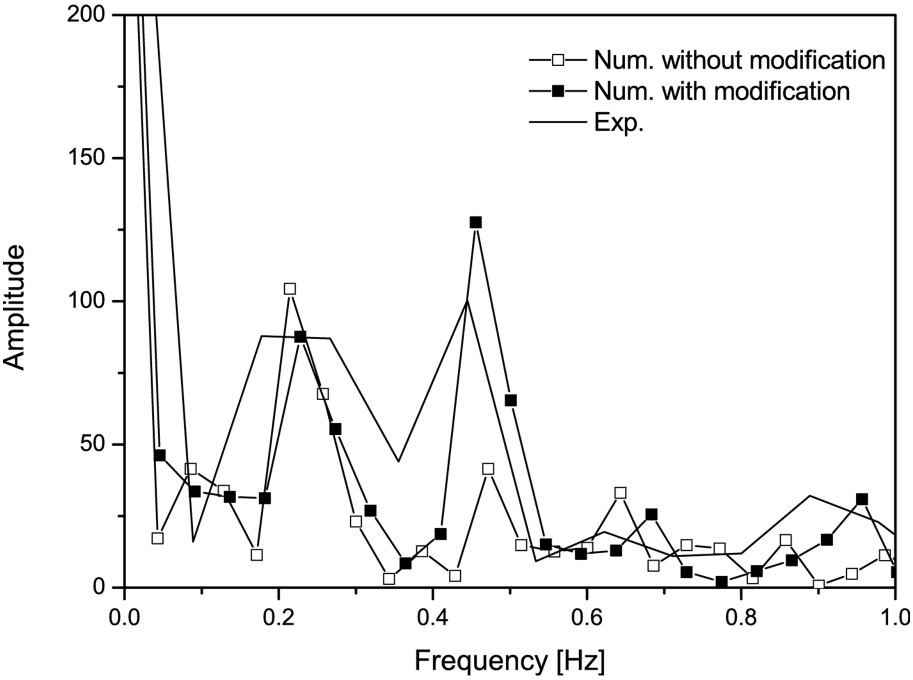

Fig. 4.21: FFT of the instantaneous horizontal velocity for $B_0 = 0.31\ T$ in the electrically insulating mold at the position P2

jet (figure 4.23(a)) indicate a return flow toward the SEN. The horizontal flow at the position below the jet (figure 4.23(c)) fluctuates only slightly around zero, confirming a calmed plug-like flow pattern in the lower mold region. The time series recorded in the vicinity of the jet show remarkable oscillations with a dominating frequency (figure 4.23(b)).

An explanation can be found by analyzing the succession of the drawings of the two-dimensional flow pattern plotted in figure 4.24. In comparison to the flow between the insulating walls as presented in figure 4.22, the jet position remains almost steady; however, a sequence of smaller vortices moves along within the jet toward the narrow face where they move along the side walls downward. Moreover, vortical structures become visible within the jet; however, the characteristic frequencies seem to be lower as found by the numerical calculations. A potential reason is the limitation of the current measuring technique with respect to the spatial resolution of the ultrasonic sensor. Future measurements might overcome this handicap by using ultrasonic sensor arrays or local conductivity anemometers.

4.2.4 Influence of Wall Conductance Ratio

In a real casting process the solidified shell plays the role of a conducting wall. The electrical wall conductance ratio was identified as an important parameter, which has a serious influence on the mold flow just as it is exposed to an external magnetic field. The wall conductance ratio increases with growing thickness of the shell. The streamlines of the time-averaged velocity in the midplane parallel to the wide face in the mold varying with the electrical wall conductance ratio under the influence of the EMBr ruler are shown in figure 4.25. It turns out that the solidifying shell has a considerable impact on the magnetic damping of the flow. The size of the recirculating eddies was compressed to the jet zone and the efficiency of the magnetic damping effect was improved with increasing electrical wall conductance ratio. The differences of the flow pattern in the mold become significant when the electrical wall conductance ratio specifies between $C_W = 0.03$ and $C_W = 0.08$ (Fig. 4.25(d) and 4.25(e)). Moreover, the flow pattern tends to behave like the case with electrically insulating wall when

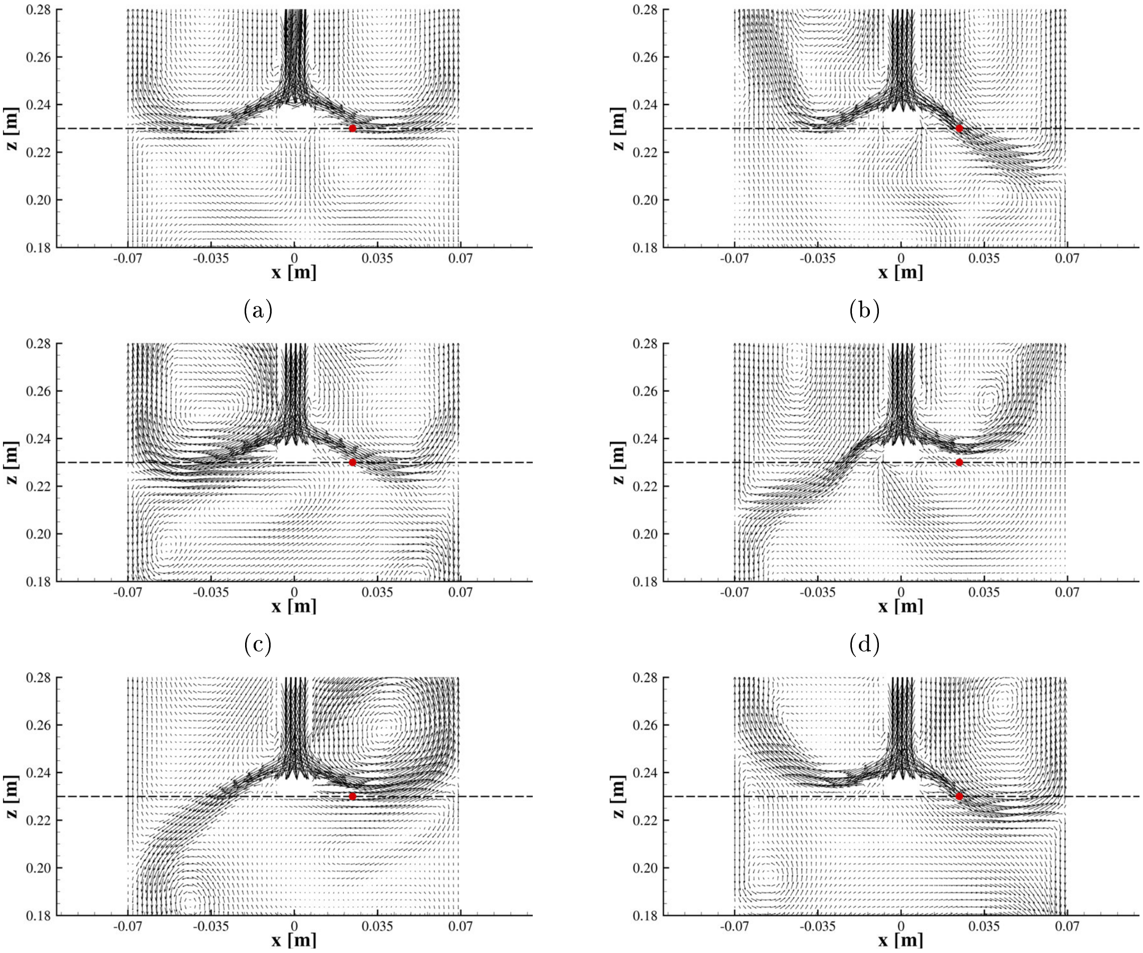

(a) (b) (c) (d) (e) (f)

Fig. 4.22: Snapshots of velocity vector field in the midplane of the mold for the case of an electrically insulating wall ($B_0 = 0.31\ T$)

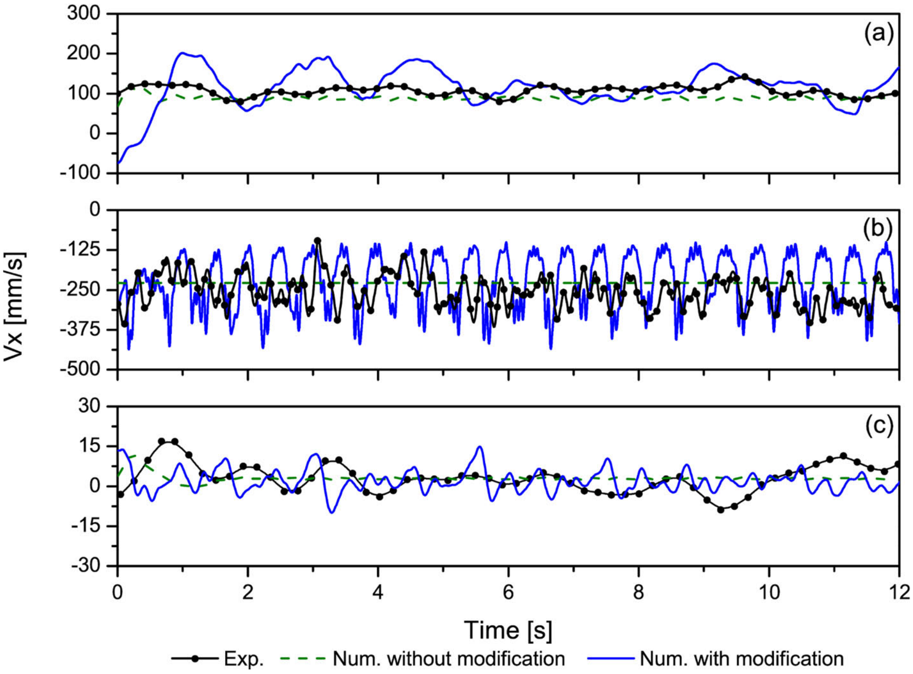

Fig. 4.23: Time series of the instantaneous horizontal velocity for $B_0 = 0.31\ T$ in the electrically conducting mold at the position P1 (top), P2 (middle) and P3 (bottom)

the electrical wall conductance ratio is less than $C_W = 0.01$.

Fig. 4.26 shows the time-averaged shear velocity profile along the x-axis at $y = 0$ on the free surface with variation of the electrical wall conductance ratio. In comparison to the case with electrically insulating wall ($C_W = 0$), the shear velocity is positive when $C_W \geq 0.01$ in the vicinity of the SEN.

From the above numerical analysis, we can draw a conclusion that the flow pattern in the mold is closely dependent on some crucial non-dimensional parameters, for example, the Hartmann number, the wall conductance ratio, the Reynolds number, etc. Therefore we propose a non-dimensional parameter to design the flow pattern in the mold under the influence of EMBr. The new non-dimensional parameter Mc is defined as follows:

$$Mc = C_W^{1/2} \frac{Ha^2}{Re} \tag{4.2}$$

To study the effect of Mc on the flow pattern, two sets of numerical simulations are performed varying the magnetic flux and the electrical conductivity of the wall. The parameters are listed in tables 4.1 and 4.2. As is shown in figure 4.27, surprisingly the same flow patterns are obtained at a fixed value of $Mc = 2.0$. Decreasing Mc to 0.63, the flow pattern differs significantly from the case with $Mc = 2.0$. In addition, we also obtain the same flow pattern on the precondition that the non-dimensional parameter Mc is fixed. It indicates that the new parameter we proposed has the potential to design and optimize the flow pattern in the mold under certain circumstance.

4.3 Summary and discussion

The main intentions for using an electromagnetic brake in slab continuous casting are the deceleration of the steel jet discharging from the SEN, the achievement of a uniform and stable flow pattern in the mold, a lowering of the surface velocity, and a reduction of turbulent

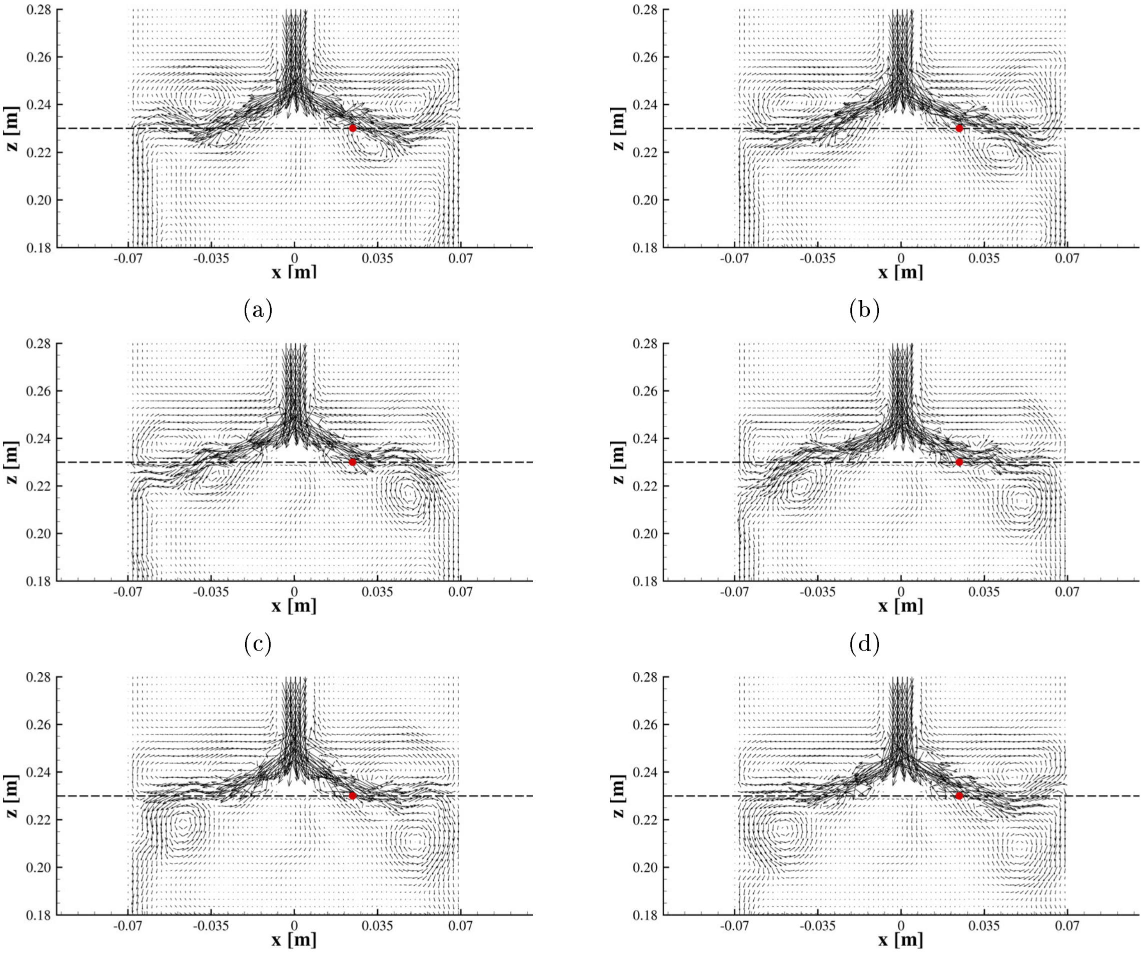

(a) (b) (c) (d) (e) (f)

Fig. 4.24: Snapshots of velocity vector field in the midplane of the mold for the case of an electrically conducting wall, $B_0 = 0.31\ T$

Tab. 4.1: Operating parameters with $Mc = 2.0$

$\sigma(S \cdot m^{-1})$	$\sigma_w(S \cdot m^{-1})$	$B_0(T)$	Ha
3.27×10^6	1.0×10^8	0.22	300
	5.2×10^7	0.27	367
	3.0×10^7	0.31	422
	1.0×10^7	0.41	556
	5.2×10^6	0.48	654
	3.0×10^6	0.55	749

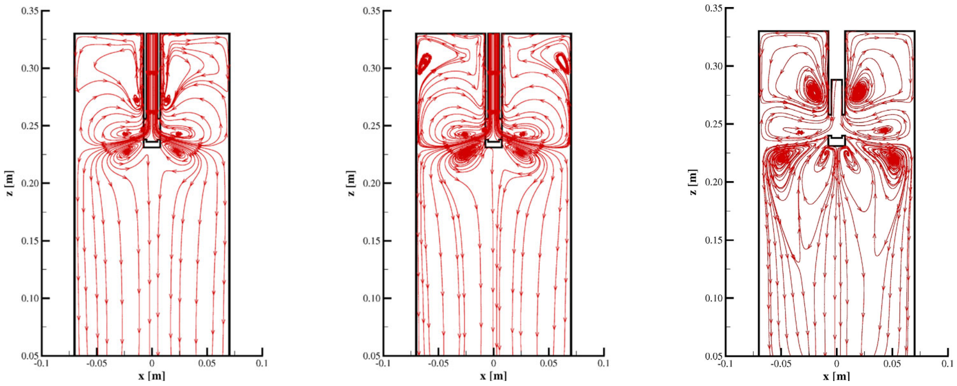

(a) Cw=0.433 (b) Cw=0.266 (c) Cw=0.133

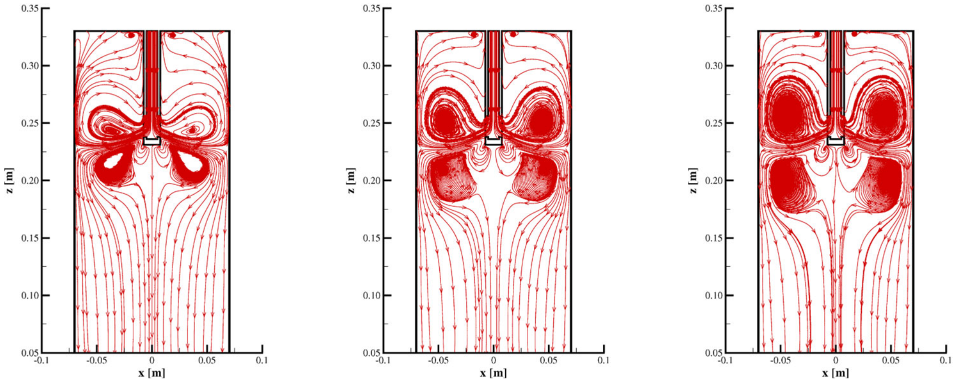

(d) Cw=0.08 (e) Cw=0.03 (f) Cw=0.01

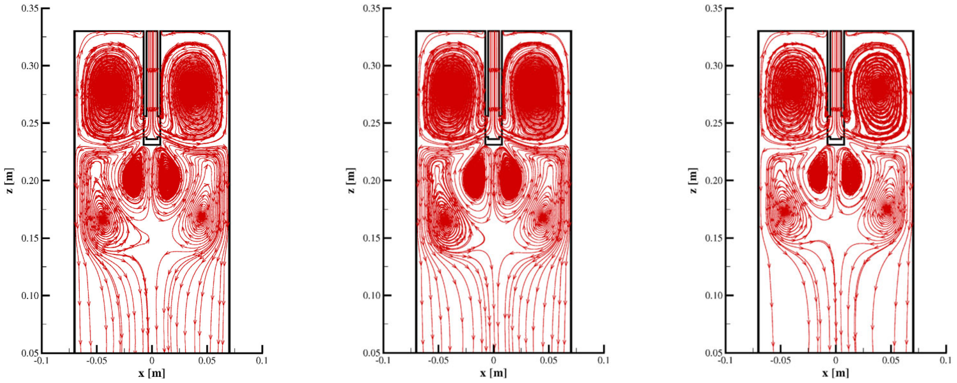

(g) Cw=10^{-5} (h) Cw=10^{-8} (i) $Cw = 10^{-11}$

Fig. 4.25: Streamlines of the time-averaged velocity in the midplane parallel to the mold wide face with different electrical conductivities of the wall ($B_0 = 0.31\ T$)

Tab. 4.2: Operating parameters with $Mc = 0.63$

$\sigma(S \cdot m^{-1})$	$\sigma_w(S \cdot m^{-1})$	$B_0(T)$	Ha
3.27×10^6	1.0×10^7	0.22	300
	5.2×10^6	0.27	367
	3.0×10^6	0.31	422
	1.0×10^6	0.41	556
	5.2×10^5	0.48	654
	3.0×10^5	0.55	749

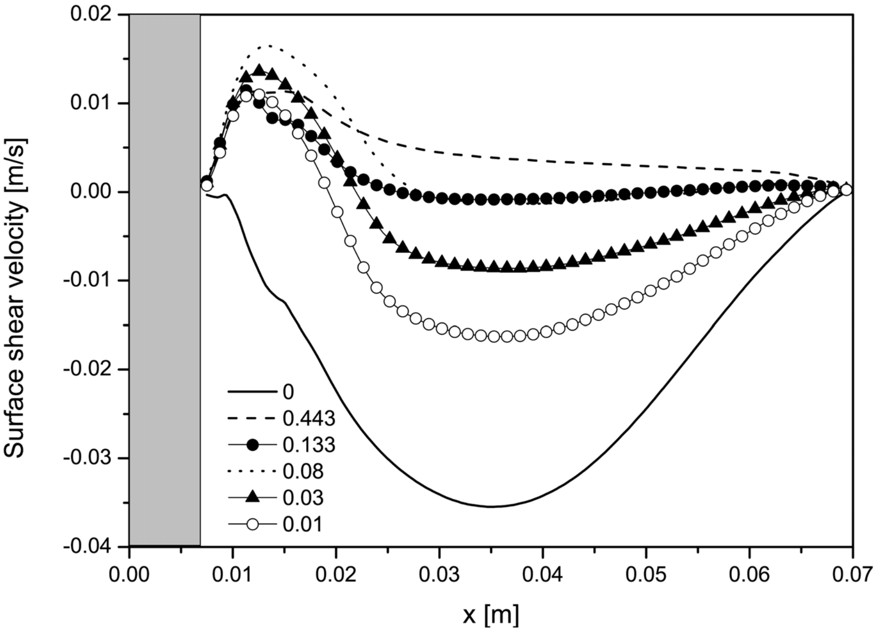

Fig. 4.26: Shear velocity along the x-axis at $y = 0$ on the free surface with different wall conductance ratio ($B_0 = 0.31\ T$)

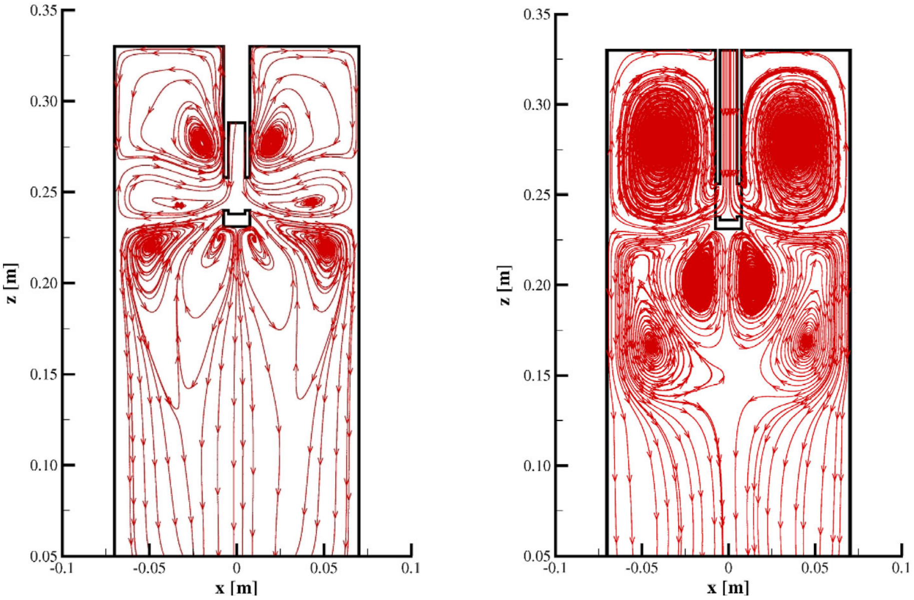

(a) $Mc = 2.0$ (b) $Mc = 0.63$

Fig. 4.27: Streamlines of the time-averaged horizontal velocity in the midplane parallel to the mold wide face varying with Mc

velocity fluctuations. The interaction between the applied magnetic field and the highly turbulent flow is very complex, and proper predictions concerning the efficiency of the EMBr are difficult. The numerical and experimental activities presented here are concerned with the melt flow in a continuous-casting mold under the impact of an EMBr, which covers the entire mold width. The effect of the DC magnetic field on the flow structure became evident both in the numerical simulations and the model experiments. Moreover, it was demonstrated that the electrical conductivity of the inner mold walls plays an important role. Modifications of the wall conductivity determine the closure of the induced electrical currents and the resulting Lorentz force. With magnetic field, the exit angle of the jet discharging from the SEN becomes flatter, which means that the penetration depth of the discharging melt flow into the lower part of the mold is reduced in the MHD case.

The flow pattern in the mold is significantly modified by the magnetic field, i.e., the typical double-roll structure is considerably deformed in the situation of an electrically conducting mold or even replaced by a multilayer vortex structure in a nonconducting mold. An inversion of the flow direction at the free surface was observed in the conducting mold.

An important issue is the magnetic damping of transient, turbulent flows. In the experiments performed within this study we did not observe a uniform damping effect of the magnetic field, which means that the resulting properties of both the mean flow and the turbulent oscillations depend significantly on the location of the observation point and the electrical boundary conditions. In particular, the application of the DC magnetic field may cause an amplification of velocity fluctuations. This effect becomes especially pronounced in case of a nonconducting mold wall resulting in a highly transient and asymmetric flow pattern. The strong velocity perturbations are associated with distinct fluctuations of the jet angle, whereas the jet oscillations on both sides of the SEN are almost opposite in phase. The situation in an electrically conducting mold is characterized by a comparatively stable flow without remarkable perturbations of the jet position. A sequence of vortices is formed inside the jet and conveyed toward the narrow face.

The application of a DC magnetic field on the flow of any electrically fluid exerts an electromagnetic damping effect. A main feature of the Joule dissipation is the anisotropy, which produces a redistribution of the turbulent energy by a selective damping of turbulent structures depending on their spatial alignment. As a consequence, velocity differences along the magnetic field direction will be eliminated. This mechanism may act as a local source of momentum, vorticity, and kinetic energy [76, 14], and it is not covered by conventional turbulence models.

The following requirements have to be taken into account for an adequate numerical simulation of the magnetic field effect on the steel flow in a continuous casting mold:

1. It must be guaranteed that the mesh size of the numerical grid resolves the Hartmann boundary layers of thickness $\delta = O(Ha^{-1})$. An improper handling of the boundary layers leads to wrong predictions of the circuits of the induced electrical currents in the melt and, consequently, to an incorrect Lorentz force.

2. The electrical conductivity of the mold wall or the solidified shell, respectively, has a large impact on the induced currents. An accurate consideration of the electrical boundary conditions is necessary to calculate the accurate Lorentz force.

3. The specific properties of the MHD turbulence have to be taken into consideration by an appropriate turbulence model. Such a model must contain respective information about the dimensionality of the turbulence and the energy distribution in the spectral space.

4. The wall conductance ratio plays a significant role for the flow structure. The new nondimensional parameter we proposed has the potential capability to design and optimize

the flow structure in a continuous casting mold subject to an EMBr.

Within this chapter, we followed the concept suggested by Widlund et al [89] to describe the anisotropic character of the MHD turbulence by a scalar dimensionality anisotropy parameter α_μ. The respective calculations delivered better predictions compared to the corresponding experimental results than comparative simulations based on the conventional turbulence models. Nevertheless, subsequent improvements of the model are necessary considering an extension to include main shear, strain, and nonlinear effects. The transport equation (2.85) for the development of α_μ is currently based on phenomenological reasoning [89]. However, the data available so far from DNS or experimental investigations do not support a serious calibration of the model. This handicap also underlines the necessity of future experimental activities using model experiments, in particular measurements of the velocity field and corresponding turbulent fluctuations in the mold, to collect a relevant database for the validation of the numerical models.

5 Study of a bubble-driven flow under the influence of a DC magnetic field

An appropriate two-phase model combined with magneto-hydrodynamic equations is indispensable to begin with investigating the effect of an EMBr on the gas-melt two-phase flow in the continuous casting process. The non-isotropic nature of MHD turbulence for single-phase flow has been implemented successfully by specific modifications of the turbulence model in chapter 3. In this chapter, the calculations were performed by means of the commercial software package CFX using the Euler-Euler multiphase approach and the URANS-SST turbulence model. The numerical models are validated with recent nontrival bubble-driven flow experiments.

The scope of the present chapter is concerned with the same configuration as investigated experimentally by [95] with its surprising observation of some magnetically enhanced oscillating flow structures. All parameters and the geometry of the problem have been chosen according to the reported experimental conditions. The motivations are to verify the modified turbulence model in investigating non-trivial phenomena under the influence of a longitudinal and a transverse DC magnetic field and to reproduce the experimentally observed magnetic field effects. As the Euler-Euler approach is adopted, the values (current density,Lorentz force, drag force, etc.) acting on finite control volume are the results from phase-weighted averaging, the interface between gas dispersed phase and liquid continua phase can not be tackled, then the physical modeling error and the spatial discretization error are unavoidable. Therefore it is indispensable to make a validation of two-phase model, in particular, with the application of magnetic field.

5.1 Computational domain and boundary conditions

The problem under consideration is shown in figure 5.1. Gas bubbles are blown into a pool with a liquid metal being at rest without gas flow. The gas injection is realized through a single orifice located at the centre of the container bottom. The fluid vessel is situated within a homogeneous DC magnetic field, which can be aligned in either vertical (longitudinal) or horizontal (transverse) direction. The calculations were performed using the same parameters and dimensions as stated in the respective experimental studies by [94, 95]. The authors investigated the bubble-driven flow inside a cylinder with electrically insulating walls. Through a single nozzle at the container bottom, Argon gas bubbles were injected into an eutectic GaInSn alloy covered by a 10 mm acid on the top. The fluid vessel had a diameter of 90 mm, and the height of the liquid column was 220 mm.

Figure 5.2 shows a typical mesh system used for a cylindrical column. Increasing the magnetic field strength, it is known that specific boundary layers occur at the container walls, so-called Hartmann layers $\delta = O(Ha^{-1})$ perpendicular to the field direction and side-layers $\delta = O(Ha^{-1/2})$ parallel to the field. The thickness of the Hartmann layer is defined as $\delta_H = R_0/Ha$. The numerical mesh must be accordingly adapted in order to provide a sufficient resolution of those layers, in particular the Hartmann boundary layers. The distance between the first node and the side face is 0.001 mm and 15 nodes in the Hartmann layer.

Boundary conditions:

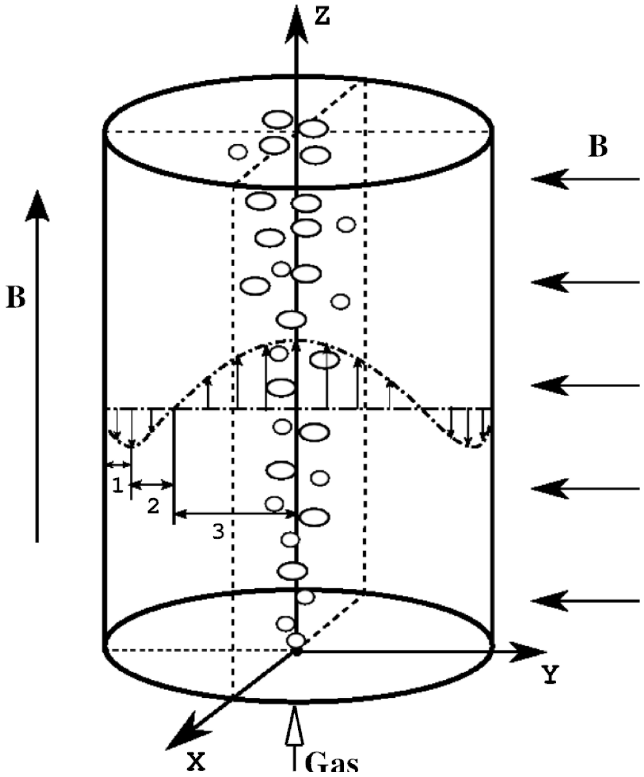
Z
B
B
1
2
3
Y
X
Gas

Fig. 5.1: Schematic view of the bubble-driven flow under consideration

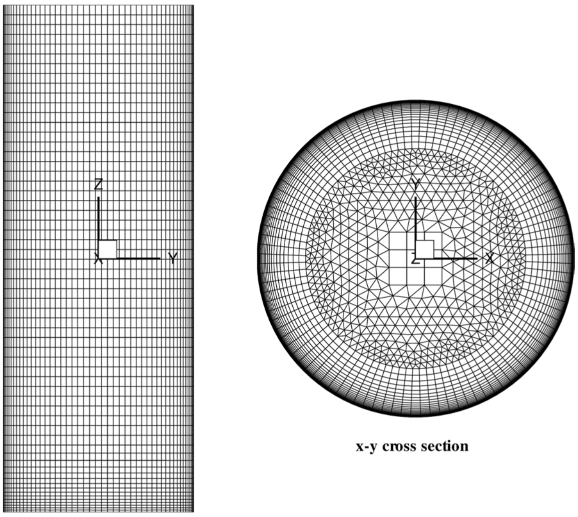
Z
X
Y
Y
Z
X
x-y cross section

Fig. 5.2: Exemplary mesh used for the simulations

- At the inlet, void fraction of gas is 1 and the gas flow rate (Q_G) is specified (0.33 cm^3/s, 0.83 cm^3/s, 3.67 cm^3/s).

- At the bottom-face and side-face, free-slip wall and no-slip wall are adopted for gas and liquid metal, respectively.

- Two types of outlet conditions are displayed in figure 5.3. The degassing outlet condition stands for the case of a completely filled container and a vanishing static pressure of the gas phase at the upper solid wall, whereas the opening outlet boundary condition stands for a free surface inside the container with a corresponding gas volume on top of the melt and gas phase is allowed to re-enter into container. Zero flux of the electric field is set on the top face.

- Electrically insulating boundary condition for the walls, which means that the current density normal to the walls is zero. At the presence of a strong magnetic field, MHD turbulence tends to be laminarized. However, the induced turbulence by bubbles can not be eliminated by the external magnetic field. Considering laminarization of MHD turbulence, a Low-Reynolds-Number method is used to resolve the details of the boundary layer profile by using very small mesh length scales in the direction normal to the wall (very thin inflation layers). In the CFX solver, it is implemented by Automatic Near-Wall Treatment.

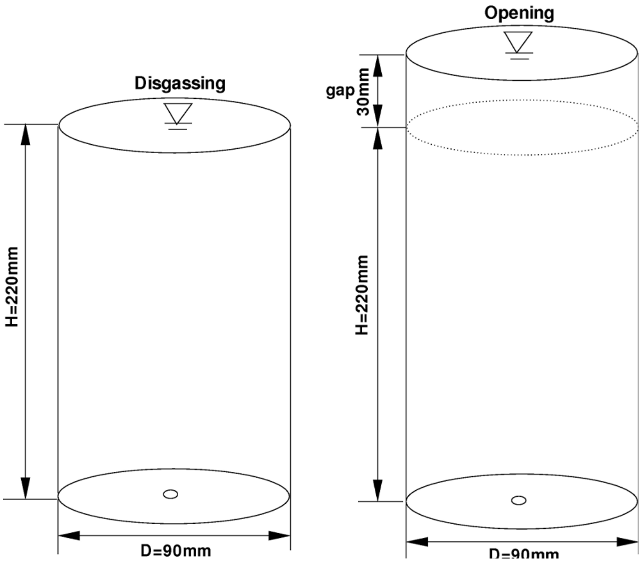

Fig. 5.3: Schematic representation of the liquid metal column showing two different types of outlet boundary conditions: degassing outlet condition (left) and opening outlet condition (right)

Furthermore, on the assumption that bubbles with mean equivalent diameter are injected through a single nozzle of diameter d_{in}, the breakup or coalescence of bubbles are neglected. The equivalent diameter of bubbles can be estimated by a relation proposed by [31]:

$$d_B = 1.25\left[6Q_G/\left(1.06\pi\right)\right]^{1/12}\left[\gamma/\left(\rho_L g^3\right)\right]^{1/12}\left(\rho_L/\rho_G\right)^{1/15}\left[d_{in}\left(Q_G^2/g\right)^{1/5}\right]^{1/6} \tag{5.1}$$

with the surface tension $\gamma = 0.533\ N/m$. In this work, calculations were carried out for gas flow rates Q_G of 0.33 cm^3/s, 0.83 cm^3/s and 3.67 cm^3/s leading to mean bubble diameters of 4.4 mm, 5.5 mm and 8.2 mm, respectively.

5.2 Results

5.2.1 Bubbly flow without magnetic field

At first, two types of outlet boundary conditions are compared for the case of a 0.83 cm^3/s gas flow rate without magnetic field. Contour plots of the time-averaged axial velocity at the longitudinal mid-center plane of the cylinder are shown in figure 5.4. The liquid-phase driven by bubbles ascends upwards at the core region and goes down in the buffer region. A boundary layer region exists close to the wall. Below the free surface, the strongest downward flow can be observed. The profiles of axial velocities of the liquid phase at the center line are plotted in figure 5.5 varying for the two different outlet boundary conditions. The velocity increases from the bottom, reaches a maximum at $z/H = 0.35$ and then reduces gradually with the increase of z/H in the case of a degassing outlet boundary condition. On the other hand, the velocity rises continuously for the opening outlet boundary condition except for the region close to the free surface. Obviously, the opening outlet boundary condition reproduces the experimental data much better than the degassing boundary condition. Therefore, the opening outlet boundary condition was used in all further simulations.

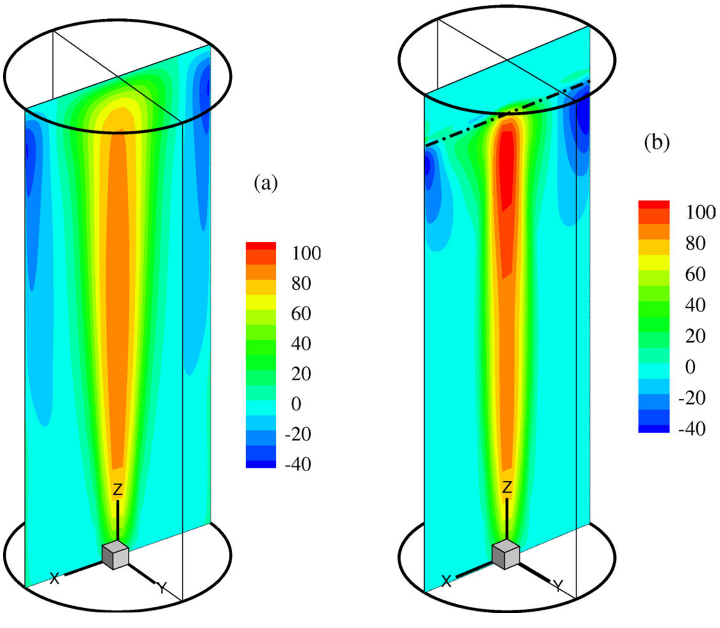

(a) degassing outlet (b) opening outlet

Fig. 5.4: Contour plots of the liquid vertical velocity at the vertical mid-plane, $Q_G = 0.83\ cm^3/s$

Next, the effect of bubble-induced turbulence on the flow was studied comparing the Sato bubble-induced turbulence model (named Sato model hereafter), and the source term modification model of bubble-induced turbulence (named correction model hereafter) which is mentioned in chapter 2. Corresponding profiles of axial velocity along the radius $r/R = 0.87$ are presented in figure 5.6. For both boundary conditions, the maximum of the downward flow can be observed beneath the free surface. The bubble-induced turbulence models make a better prediction than the case without BIT (bubble-induced-turbulent) model. The tendency of numerical results are in good agreement with the experiment except for the failure to capture the small counterrotating vortex in the lower corner. Moreover, the deviation of peek position and velocity amplitude are significant owing to the weighted-averaging of Euler-Euler approach.

Figure 5.7(a) shows axial velocity profiles along the axial direction at $r/R = 0.87$ for a gas flow rate of 0.33 cm^3/s. Both calculations of the Sato bubble-induced turbulence model and

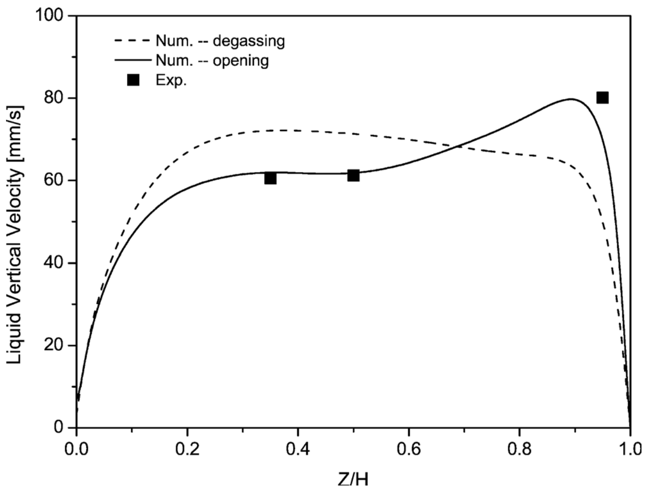

Fig. 5.5: Profiles of the axial liquid velocity for both outlet boundary conditions at $Q_G = 0.83\ cm^3/s$

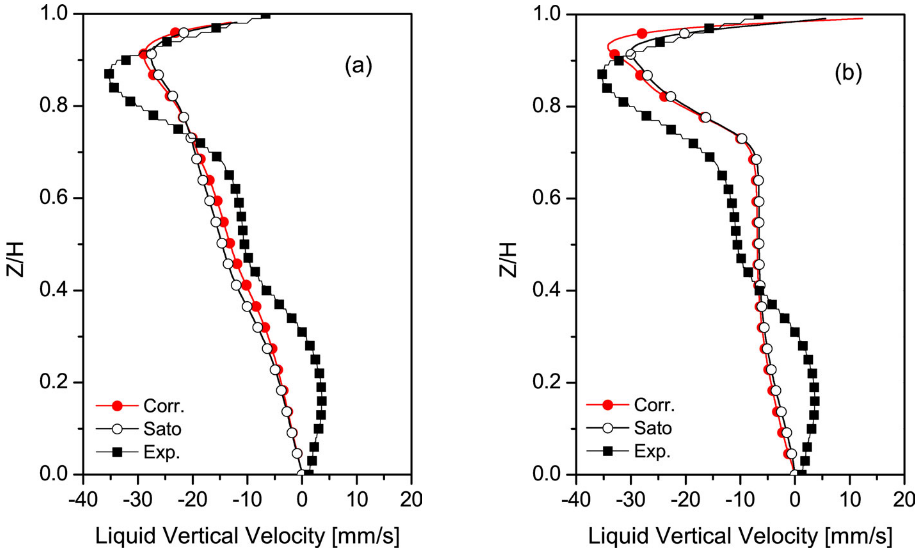

(a) degassing outlet (b) opening outlet

Fig. 5.6: Profiles of the vertical liquid velocity along a line at $r/R = 0.87$ for two turbulence models and two outlet boundary conditions at $Q_G = 0.83\ cm^3/s$

the source term modification model of bubble-induced turbulence are in agreement with measurements. The correction model captures the measured maximum downward flow below the free surface slightly better than the Sato model. The same is true for the case of the bubble column, as shown in figure 5.7(b), where the axial liquid-phase velocity distributions along the diameter at half height obtained with Sato and correction models are compared with measurements. The calculations are very close to the experimental data.

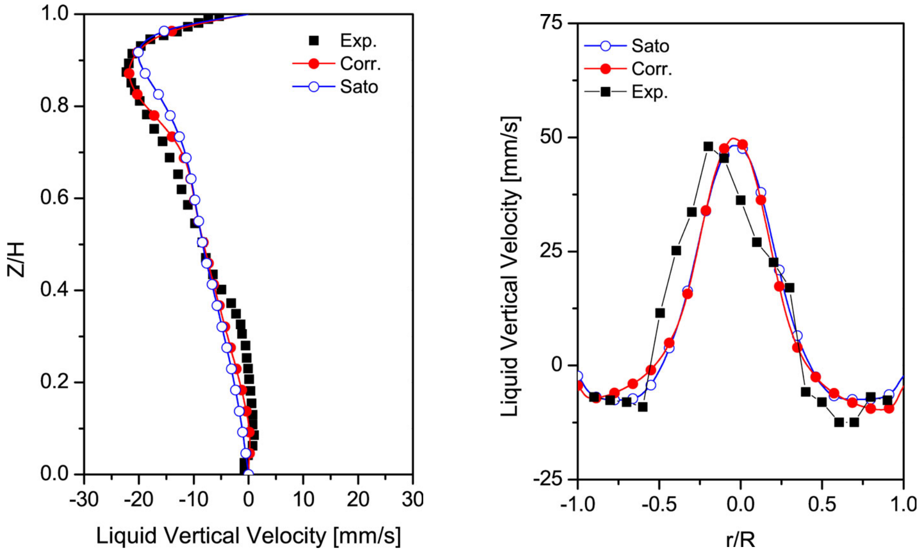

(a) $r/R = 0.87$ (b) $z/H = 0.5$

Fig. 5.7: Vertical and radial profiles of the vertical liquid velocity for two turbulence models calculated at $Q_G = 0.33\ cm^3/s$

5.2.2 Bubbly flow with longitudinal magnetic field

One of the usual purposes of an externally imposed magnetic field is stabilization of the flow and suppression of oscillatory instabilities. Figure 5.8 shows the contours of the time-averaged axial velocity at the longitudinal mid-center planes of the column in the presence of a longitudinal magnetic field. It is no surprise that the intensity of the bulk flow is suppressed by imposing the magnetic field. Compared to the case without magnetic field, the former strong recirculation zone was squeezed into a narrow region close to the bubble plume owing to the stretching effect along the magnetic field lines. The flow in the column remains of a single cell pattern independent of the magnetic field application.

Figure 5.9 illustrates the corresponding radial velocity distributions along the diameter at half height for two Hartmann numbers. The damping effect can be observed clearly. As shown in figure 5.9, the axial liquid velocity with two different bubble-induced turbulence models is compared with experimental data at a gas flow rate of 0.33 cm^3/s. Both predictions are close to the measurement except for the slight deviation of the velocity peak, which is probably caused by the highly nonuniform movement of bubbles. However, the deviation of velocity in the downward region (between wall and core upward flow) increases with the application of magnetic field in comparison figure 5.9 to figure 5.7.

5.2.3 Bubbly flow with transverse magnetic field

The transverse magnetic field causes a pronounced an-isotropy in the flow. Therefore, figure 5.10 shows the flow field in two half-planes oriented parallel and perpendicular to the magnetic field, respectively. Figure 5.10 depicts the velocity streamline with and without the

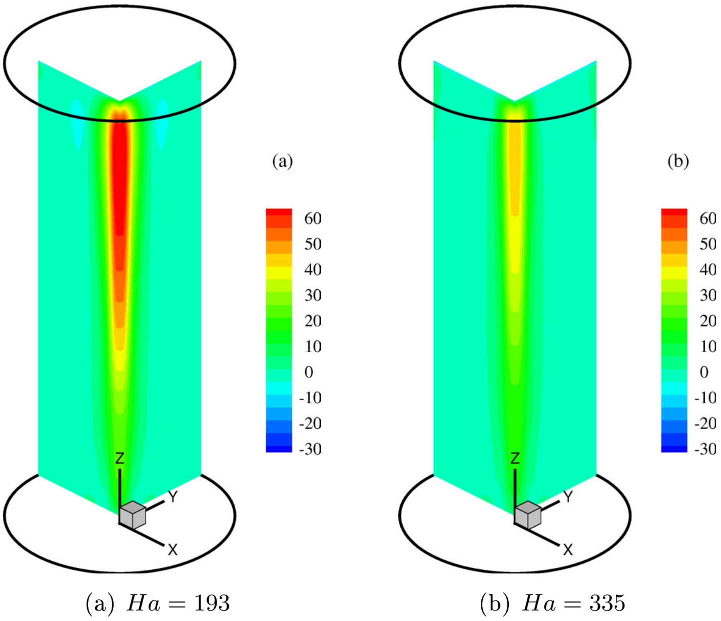

(a) $Ha = 193$ (b) $Ha = 335$

Fig. 5.8: Contour plots of the vertical liquid velocity obtained by the correction model for a longitudinal magnetic field at $Q_G = 0.33\ cm^3/s$

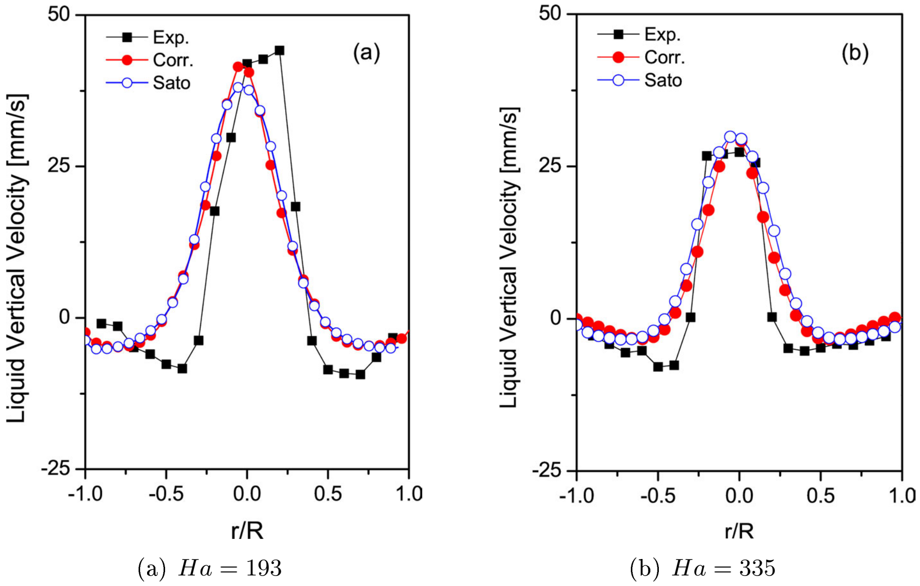

(a) $Ha = 193$ (b) $Ha = 335$

Fig. 5.9: Radial profiles of the vertical liquid velocity along the cylinder diameter at $z/H = 0.5$ for a longitudinal magnetic field at $Q_G = 0.33\ cm^3/s$

modification of the turbulence model for the MHD case (so-called α_μ effect) at $Ha = 271$ for two gas flow rates. To compare the mean flow from experimental results, the numerical results are obtained statistically by arithmetic mean method from 40 s to 120 s. As can be seen, the α_μ effect has a great impact on the flow pattern in MHD turbulence. The resulting flow structure can not be represented numerically without this modification. The α_μ effect was taken into account in all later calculations. In the plane parallel to the magnetic field, the liquid was enforced to ascend by the electromagnetic force. The global recirculation flow was broken and reconstructed into several vortices in the plane perpendicular to the magnetic field. The downward flow was somewhat intensified in the lower region of the bubbly column compared to the case without magnetic field. Typical distributions of velocity (green vector), Lorentz force (blue vector) and electrical current (brown line) on the cross-section at $z/H = 0.5$ are demonstrated in figure 5.11. Under transverse magnetic field, currents pass through the core of the jet and close in the Hartmann layer. The flow ascends in a narrow area along the magnetic field direction and descends in the other parts (see figure 5.11(b)). A similar phenomenon with respect to MHD flows has been discussed by Davidson (1995, 2001). However, the electric current distribute in the way of concentric circles (see figure 5.11(a)).

Another important issue is that the application of a transverse magnetic field causes the flow to become transient. As is shown in figure 5.12, the liquid velocity quasi-periodically moves up and down in the buffer region. As expected, the vortex is elongated along the direction of the magnetic field. This vortex stretching leads to a decrease of the radial length scale of the associated vorticity. As a consequence, the corresponding velocity is intensified due to the conservation of angular momentum. On the other hand, this process probably origins from the instability of the side-layer boundary (see figure 5.12(b)), where an inverse small eddy occurs in the vicinity of the wall. With the evolution of the inverse eddy, the flow structure was modified and separated. Consequently, the flow becomes transient and oscillating. Moreover, the gas-liquid slip velocity increases as a result of the damping effect of the magnetic field. This, in turn, continuously feeds the turbulence of the liquid-phase to counteract the damping effect in the core region of the bubble column.

Local velocity time series are shown in figure 5.13. The data were acquired at the position $r/R = 0.87, z/H = 0.5$ in the center-plane perpendicular to the magnetic field. Contrary to the global damping effect with the imposition of a longitudinal magnetic field, a significant oscillation can be observed for the application of a transverse magnetic field. Obviously, the local flow was reinforced in comparison to the case without magnetic field. The velocity amplitude varies with the intensity of the magnetic field and reaches a maximum at $Ha = 271$ in these calculations. For larger Ha the damping effect of the magnetic field dominates. As seen in figure 5.13 the numerical results are in good agreement with the experiments, except for the high frequency fluctuations due to the limitation of the Reynolds time-averaged turbulence model.

The time-averaged volume fraction of bubbles at the free surface are depicted in figure 5.14. Without magnetic field, the bubble plume shows isotropic distribution in the center-core. With magnetic field the dispersion of bubbles is suppressed and concentrated in the core. Increasing the magnetic field to $Ha = 271$, the distribution of bubbles has a tendency to anisotropy. The bubble dispersion is mainly suppressed in the direction parallel to the magnetic field which is closely related to the an-isotropic MHD turbulence under the influence of a transverse magnetic field.

The relationship between the total kinetic energy of the liquid in the cylinder and the Hartmann number is illustrated in figure 5.15. The total kinetic energy is obtained by means of volume integral of computation domain. For moderate Hartmann numbers, the total kinetic energy was surprisingly increased. Further increasing Hartmann number, the damping influence dominates and the total momentum decreases gradually.

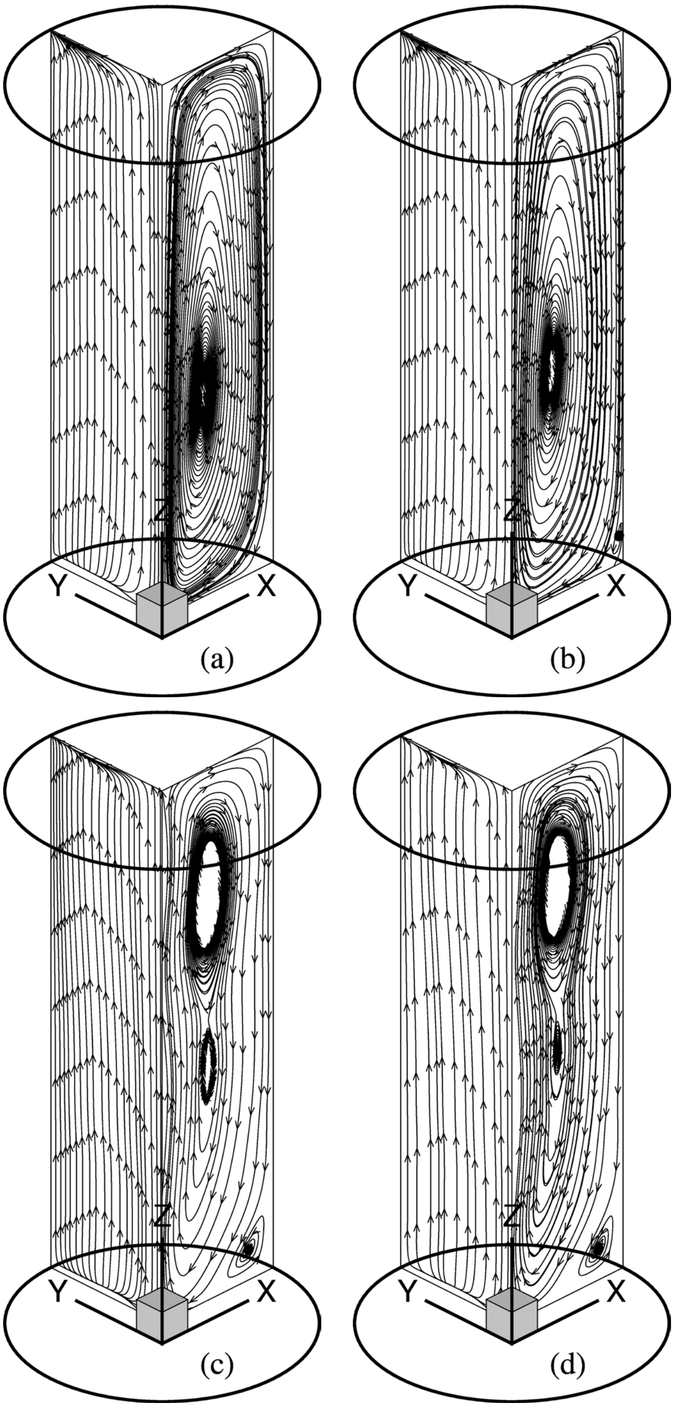

Fig. 5.10: Streamlines of the time-averaged liquid velocity in a transverse magnetic field for $Ha = 271$: (a and c) $Q_G = 0.83\ cm^3/s$, (b and d) $Q_G = 3.67\ cm^3/s$. (a and b) conventional turbulence model, (c and d) modified turbulence model taking into account the anisotropy coefficient as described in the text

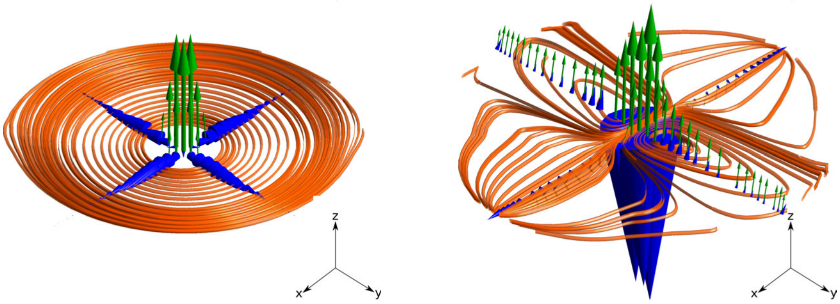

(a) $(0, 0, B_0)$ (b) $(0, B_0, 0)$

Fig. 5.11: Distributions of the electrical current density (streamlines) and the velocity (cones) over the cross section at $z/H = 0.5$

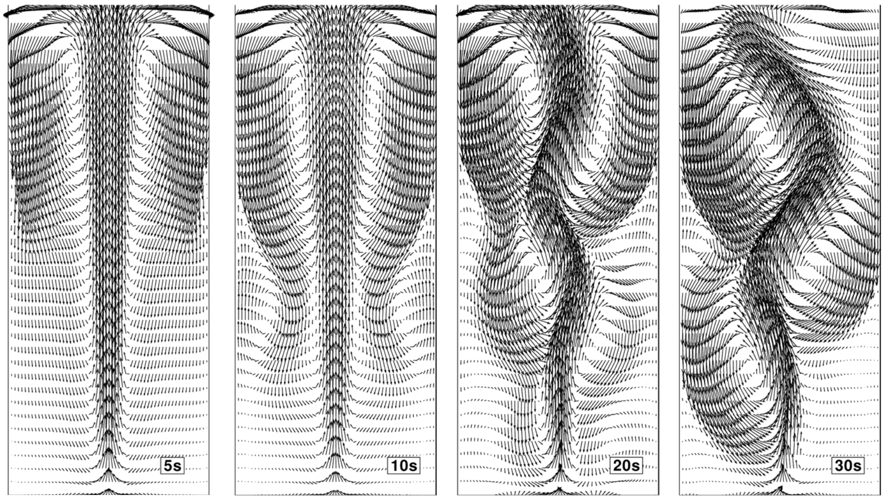

(a) (b) (c) (d)

Fig. 5.12: Vector plots of the liquid velocity at the center plane perpendicular to the direction of the transverse magnetic field for $Q_G = 0.83\ cm^3/s$ and $Ha = 271$

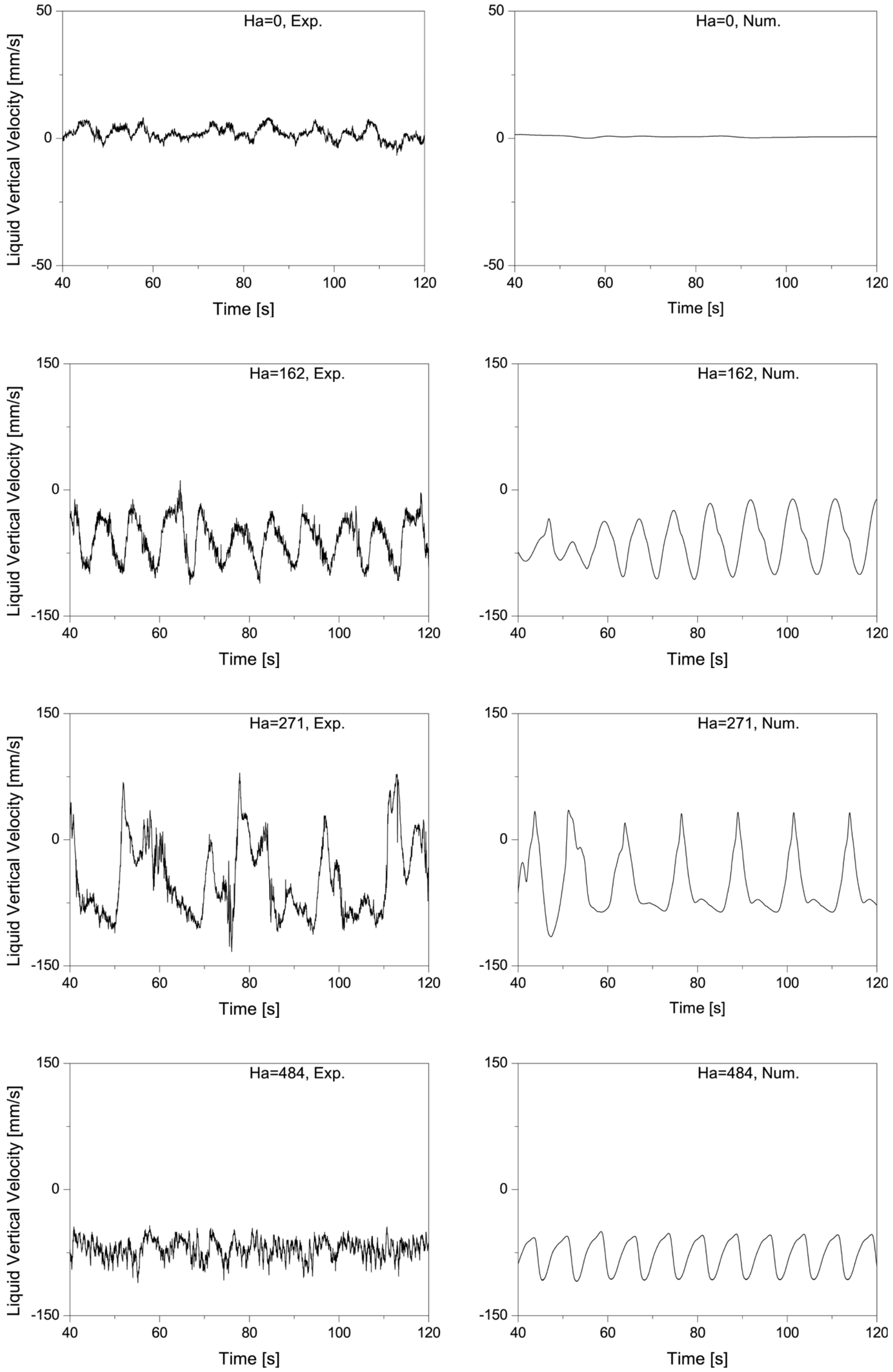

Fig. 5.13: Time series of the local liquid velocity for various Hartmann numbers ($Q_G = 3.67\ cm^3/s$, $r/R = 0.87$, $z/H = 0.5$)

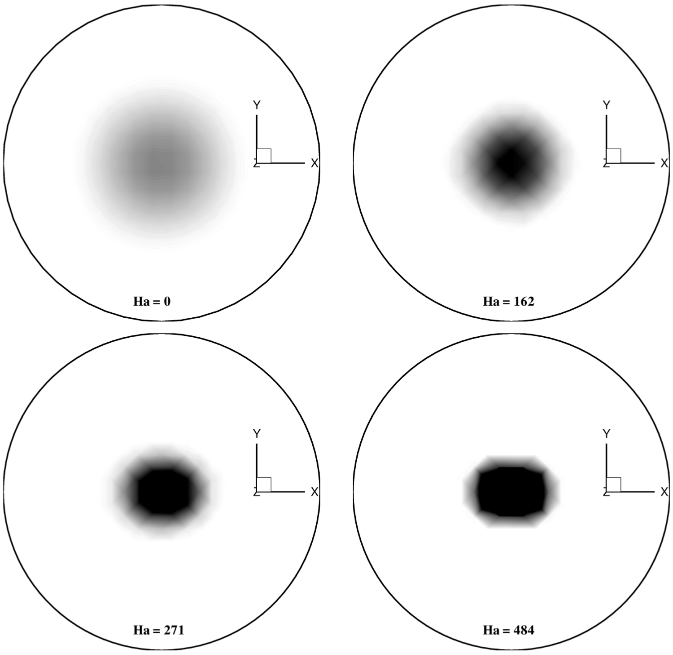

Fig. 5.14: Contour plots of the void fraction at the free surface in a transverse magnetic field at $Q_G = 0.83$ cm^3/s

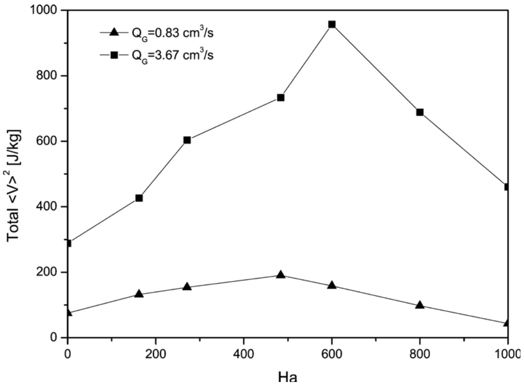

Fig. 5.15: Total kinetic energy of the liquid motion as a function of the Hartmann number

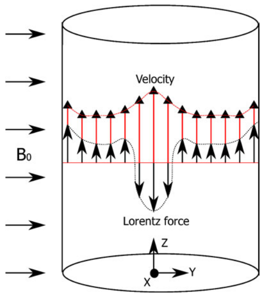

Fig. 5.16: Schematic drawing of the Lorentz force and the liquid velocity in the mid-plane parallel to the direction of the transverse magnetic field

5.3 Summary and discussion

The present chapter deals with numerical simulations considering a bubble-driven liquid metal flow in a cylinder exposed to a DC magnetic field. The calculations were carried out using the commercial flow solver CFX with the implemented Euler-Euler multiphase model. The turbulent flow was considered by a RANS-SST turbulence model, wherein the anisotropy variable as proposed by [89] was implemented in order to take into account the peculiar properties of the anisotropic MHD turbulence. The proper modeling of the MHD turbulence is still a challenge. Many studies were concerned with numerical and experimental investigations of MHD flows in a straight duct (see for instance [8, 67, 41, 58, 43]). Turbulent MHD duct flow in a transverse magnetic field becomes laminar if the applied field is sufficiently strong. The ratio Ha/Re turned out to be the relevant criterion for that phenomenon. Several studies report that the transition from a turbulent to a laminar flow occurs approximately at Re/Ha from 220 to 400. In our case considered here this ratio varies approximately between 16 and 42. Obviously, it could be concluded that the flow might be laminar, which is why the question arises whether our approach to use the RANS-SST turbulence model within the numerical calculations is appropriate.

The most striking feature of the experiment reported by [95] was the destabilization effect of the global flow due to the DC magnetic field. This phenomenon was verified by measurements of the local velocity in the bulk of the liquid. Depending on the gas flow rate and the Hartmann number different transient flow patterns were observed showing strong velocity oscillations with predominant frequencies. This finding appears to be contradictory with respect to the classical studies of the MHD duct flow and is a strong indicator that the relaminarization process of an originally turbulent flow by an applied DC magnetic field is not fully understood yet for flow configurations deviating from the standard duct flow. [19] showed that the installation of local turbulence promoters in form of a grid inside the duct can lead to turbulent MHD duct flows in the range of Re/Ha form 10 to 220. The rising gas bubbles may act as a kind of turbulence promoters, too. Moreover, the effect of a distinct agitation of the melt flow by a transverse DC magnetic field was also observed by [83] for the situation of a submerged jet.

The damping effect of a static magnetic field on the electrically conducting liquid is strongly dependent on the direction of the magnetic field with respect to the liquid recirculation. Our simulations demonstrate that the mean flow was significantly damped in case of a longitudinal magnetic field, whereas the application of a transverse magnetic field results in a rather complex flow structure of the liquid phase. The global flow recirculation loses its symmetry and is decomposed into two parts with respect to the centerplane parallel to the magnetic field. An ascending flow of the liquid metal is established in the narrow center region parallel to the magnetic field, whereas the recirculating downward flow is intensified in the other area, see figure 5.10. The schematic view in figure 5.16 shows the distribution of the Lorentz force along the center plane parallel to the magnetic field. In the buffer region, the Lorentz force accelerates the flow. In the core region, the bubble buoyancy is dominant to drive the flow upwards. Thus, the Lorentz force has essentially two effects in this bubble-driven flow: accelerating and damping. Velocity gradients along the magnetic field lines are reduced. At a moderate magnetic field, the accelerating effect becomes dominant so that the flow was intensified. As seen in figure 5.15, for a moderate magnetic field the total energy increases for increasing Hartmann number. If the Hartmann number reaches a certain value the damping effect becomes dominant, and the total energy starts to decrease with further increasing Hartmann number. The transverse field does not only cause a significant redistribution of the mean flow structure, it also gives rise to magnetically induced oscillations of the flow as shown in Figs. 5.12 and 5.13.

The correct reproduction of those phenomena can be considered as a challenge for corresponding numerical simulations. It turned out that the magnetic field action must be taken into account not only as the resulting Lorentz force, but in particular, it has also to be considered in the turbulence model. In this chapter we used the so-called anisotropy factor al proposed by [89]. We are aware about the fact that here we have only done the very first and simple step to achieve an appropriate model for such complex MHD flows. Nevertheless, the paper demonstrates that this approach gives a certain progress, because corresponding test calculations without and with this type of modified turbulence model demonstrated its significance to achieve a qualitative agreement with the experimental data.

Moreover, two types of outlet boundary condition were tested for bubbly flow simulations. In comparison to the experiments, both of them are able to obtain the correct global recirculation flow structure, but the opening outlet condition showed better agreement with the flow measurements from [95]. Therefore, the opening outlet boundary condition is recommended for the simulation of the bubble-driven flows considered here.

The analysis of this generic MHD two-phase flow case is considered as a necessary basis for simulations of more complex two-phase flow problems as they occur, for instance, in continuous casting processes with argon injection and the application of electromagnetic fields for flow control.

6 Two-phase flow in a continuous casting slab mold under influence of an external magnetic field

In steel continuous casting process, generally, Argon gas is injected to prevent SEN from clogging and to reduce the quantity of inclusions in molten steel by attaching. Therefore, an applicable two-phase model is required when the investigation of EMBr is made. Validation of the modified turbulence model on single and two-phase turbulence flow has been performed successfully as mentioned in Chapter 3 and 4. In this chapter, the effect of gas injection and EMBr is studied. Both the mono-dispersed model and a poly-dispersed particle model have been developed on the precondition that the gas phase is treated as bubbles. The mathematical models have been introduced in Chapter 2. Numerical simulations are performed by using ANSYS CFX on the hypnos cluster in HZDR.

6.1 Computational domain and boundary conditions

Figure 6.1 shows the full scale computational domain, which is divided into $\sim$ 2.2 million hybrid cells on the basis of Mini-LIMMCAST. At the inlet flow rate of the liquid metal is 0.1 l/s and the flow rate of argon gas is given by 500 *sccm*, where *sccm* denotes cubic centimeters per minute. In the poly-dispersed particle model, the gas phase is classified by ten groups in which the diameters of the gas phase vary from 0.1 mm to 10 mm. Size group is defined as equal diameter discretization, so that, d_i, the diameter of group i is calculated from:

$$d_i = d_{min} + \frac{d_{max} - d_{min}}{Nr}(i - \frac{1}{2}), \tag{6.1}$$

where Nr is the group number, and the bubble size and size fraction are listed in table 6.1.

Tab. 6.1: Bubble size and size fraction

Group	Diameter (mm)	Size fraction
Group 1	0.595	0.05
Group 2	1.585	0.05
Group 3	2.575	0.1
Group 4	3.565	0.1
Group 5	4.555	0.2
Group 6	5.545	0.2
Group 7	6.535	0.1
Group 8	7.525	0.1
Group 9	8.515	0.05
Group 10	9.505	0.05

The specifications of boundary conditions are:

1. Nozzle Inlet: the inlet velocity of molten steel was calculated by the flow rate ($0.1\ l/s$). Standard equations for fully-developed flow in a pipe were used to describe this velocity profile. The turbulent kinematic energy and the dissipation rate at the inlet are estimated by using the semi-empirical relations [35] $\kappa = 0.01u_{in}^2$ and $\varepsilon = 0.09\kappa^{1.5}/d_{nozzle}$, where d_{nozzle} is the hydraulic diameter of the submerged entry nozzle. The flow rate of gas was computed by the effective injection area and the volume ratio of molten steel to gas.

2. Meniscus: At the meniscus, a degassing boundary condition was specified, at which only the gas phase was allowed to escape. A zero-shear condition is specified for molten steel without considering the effect of mold flux.

3. Mold cavity outlet: normal gradients of all variables are set to zero. The opening pressure and direction is specified. Once the flow direction is into the domain, the pressure value is taken to be the total pressure based on the normal component of velocity. While it is leaving the domain, it is taken to be relative static pressure. At the outlet, the relative static pressure is set to zero.

4. Walls: a no-slip condition for liquid metal, free-slip condition for bubbles and Automatic-Near-Wall function is used for all walls.

5. Magnetic field: the magnetic field is static inhomogeneous and obtained from measurements, which is interpolated into ANSYS CFX as a 3D external magnetic field. For an electrically insulating boundary, the gradient of the electrical potential is zero at the wall. For an electrically conducting boundary, electric current is conserved through the interface between fluid domain and solid domain (shell). formula is given in Chapter 4.

Moreover, the Hartmann layer is considered by fining the mesh in the vicinity of the wide and narrow faces in the mold regarding the implementation of the external DC magnetic field. The location of special points and lines in the mold midplane is shown in figure 6.2.

6.2 Numerical Results

6.2.1 Mono-dispersed particle model

Among the gas-liquid flow parameters, the bubble diameter is one of the most influential parameters in predicting the void fraction distribution. Figure 6.3 displays the streamlines of the time-averaged velocity (left part) and the void fraction distribution of the gas phase (right part) varying with the bubble diameter without magnetic field. The overall streamline distribution presents a double-roll flow pattern for all the cases. As is shown in figure 6.3(a), most of the bubbles separate from the jets and ascend up in the upper recirculation zone in the mold. A small amount of bubbles follows the bulk-flow into the lower recirculation zone and some of them were entrapped in the lower large eddy in the case of 1 mm diameter bubbles. For increasing bubble size, the bubbles from SEN ports distribute mainly in the upper recirculation zone and concentrate in the vicinity of the SEN (figure 6.3(b)$-$(d)). The corresponding void fraction of bubbles on the free surface are plotted in figure 6.4. Obviously the bubbles widespread on the whole free surface in the case of $1mm$ diameter bubbles. The void fraction of bubbles agglomerates gradually in the vicinity of the SEN with the increases of bubble size.

On the other hand, the two eddies were restricted to the jet area and a plug-like flow pattern is obtained in the lower recirculation zone for the electrically conducting wall condition with EMBr ruler (figure 6.5). Differing from the case without magnetic field, all bubbles from SEN ports ascend towards the top free surface as a result of a reversed flow emerged in the upper

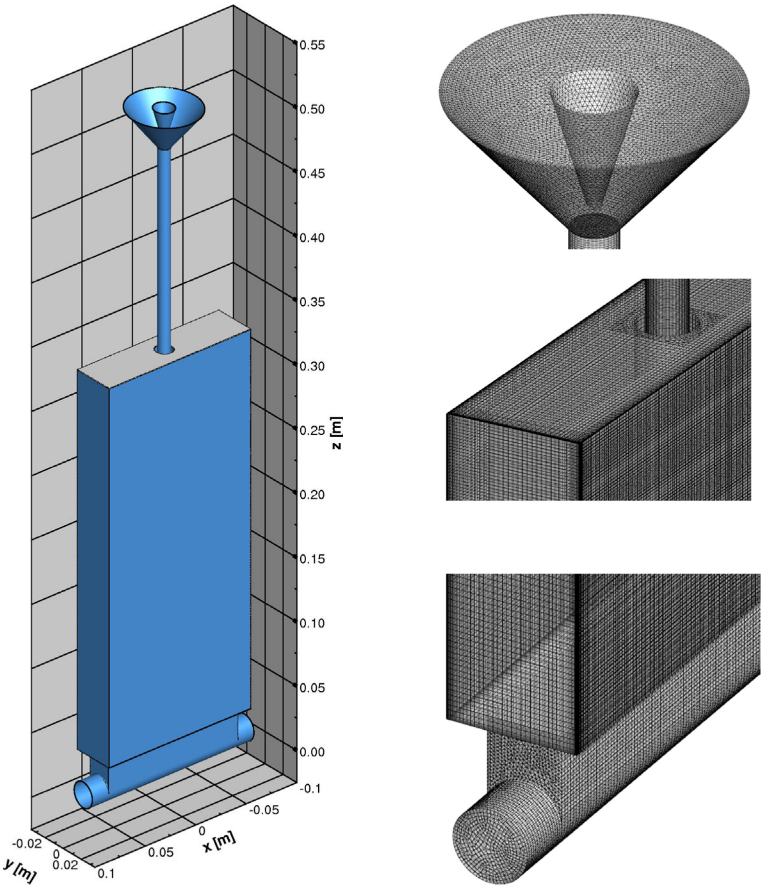
0.55
0.50
0.45
0.40
0.35
0.30
0.25
z [m]
0.20
0.15
0.10
0.05
0.00
-0.1
-0.05
0
x [m]
0.05
0.1
-0.02
0
0.02
y [m]

(a) Gemometry (b) Mesh

Fig. 6.1: Computational domain and mesh

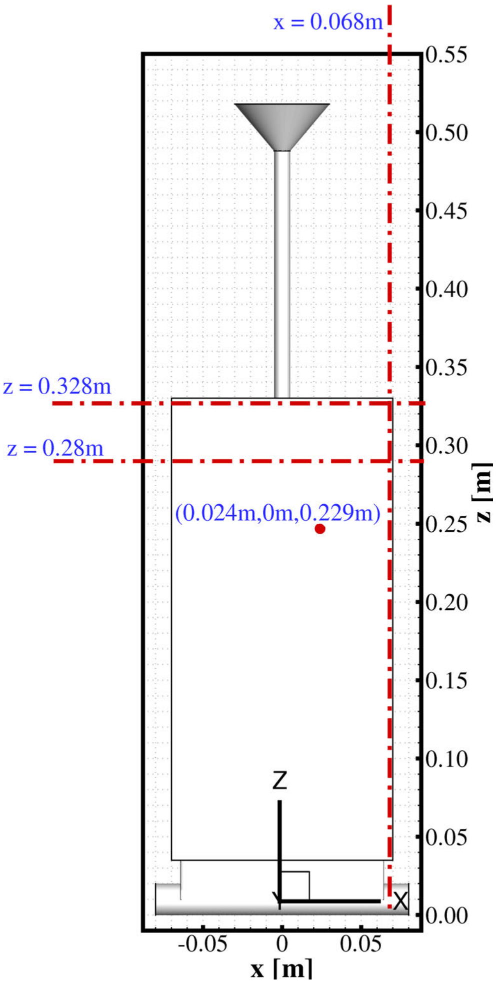
x = 0.068m
z = 0.328m
z = 0.28m
(0.024m,0m,0.229m)
Z
X
0.55
0.50
0.45
0.40
0.35
0.30
0.25
0.20
0.15
0.10
0.05
0.00
z [m]
-0.05
0
0.05
x [m]

Fig. 6.2: Location of special points and lines in the mold midplane across the wide face

recirculation zone (left parts of figure 6.5). As can be seen in figure 6.6, we can also observe the similar phenomenon that the void fraction of bubbles has a tendency towards shrinking in the vicinity of the SEN with the increases of bubble diameter.

Furthermore, a quantitative comparison of the horizontal velocity is performed. Figure 6.7 and 6.8 display time-averaged horizontal velocity plots on the top surface center line at $z = 0.328$ m with and without magnetic field. It is apparent from figure 6.7 that the injection of gas increases the surface velocity significantly, especially, for the case of large bubble size. The flow is oriented to the opposite under the influence of the magnetic field for the electrically conducting wall condition (see figure 6.8). In comparison to the case without gas injection, the surface flow is suppressed globally. Moreover, the velocity is reduced with decreasing the bubble size in the vicinity of the SEN. The corresponding time-averaged horizontal velocity distributions on a vertical centerline at $x = 0.068$ m are shown in figure 6.9 and 6.10. As can be seen in figure 6.9, the impinging intensity on the narrow face is strengthened remarkably compared to the case without gas injection and the change of bubble size has no significant influence. For the electrically conducting wall condition, the impinging intensity on the narrow face is reduced remarkably compared to the case without gas injection (see figure 6.10). In addition, the influence of bubble size on the impinging intensity is similar to that of the no magnetic field case.

6.2.2 Poly-dispersed particle model

In reality, the gas injected into the mold distributes non-uniformly with variation of the bubble size. Therefore, further numerical prediction will be performed using the inhomogenous MUSIG model. As described above, gas bubbles discharged from the SEN ports will separate from the jets. Large bubbles drift up quickly and most of them ascend in the upper recirculation zone. In addition, small bubbles float up slowly due to the influence of drag force and wake. Smaller bubbles can be subsequently carried by flowing downstream and are easily entrapped into the lower recirculation zone. Gas phase distributions varying with wall boundary conditions are shown in figure 6.11. It is clear that the gas plume is remarkably changed with the application of the magnetic field. For the case without magnetic field, the gas bubbles widespread in the upper recirculation zone (see figure 6.11(a)). In comparison to the case without magnetic field, the gas plume was more restricted to the SEN area under the influence of magnetic field (see figure 6.11(b) and (c)). In particular, gas bubbles are mainly concentrated in the vicinity of the SEN till they escape from the top surface for the case of electrically conducting wall (figure 6.11(c)).

The turbulent kinetic energy is one of the most important variables in gas-liquid flow, which is the ratio of the rms (root-means-square) of the turbulent velocity fluctuations and the mean velocity. The magnetic field also influences turbulence. Figure 6.12 presents the time-averaged distributions of turbulent kinetic energy in the mid-plane across the wide face. For the case of electrically insulating wall, the turbulent kinetic energy is slightly decreased in comparison to the case without magnetic field (figure 6.12(a), 6.12(b)). On the other hand, the turbulent kinetic energy is significantly reduced in case of an electrically conducting wall (figure 6.12(c)). Vortex cores for the different boundary conditions are shown in figure 6.13. The eddies in the mold cavity are oriented parallel to the direction of the external magnetic field. Due to Joule dissipation, some of the eddies are diminished (figure 6.13(b), 6.13(c)) compared to the case without magnetic field. Figure 6.14 displays the distributions of shear strain rate in the mold. As can be seen, the shear strain rate is intensified on the wide faces in the jet region with electrically insulating wall and remarkably reduced for the case with electrically conducting wall.

The corresponding time series of liquid metal velocity at one position in the jet zone is illustrated in figure 6.15. The braking effect is significant with the imposition of the external

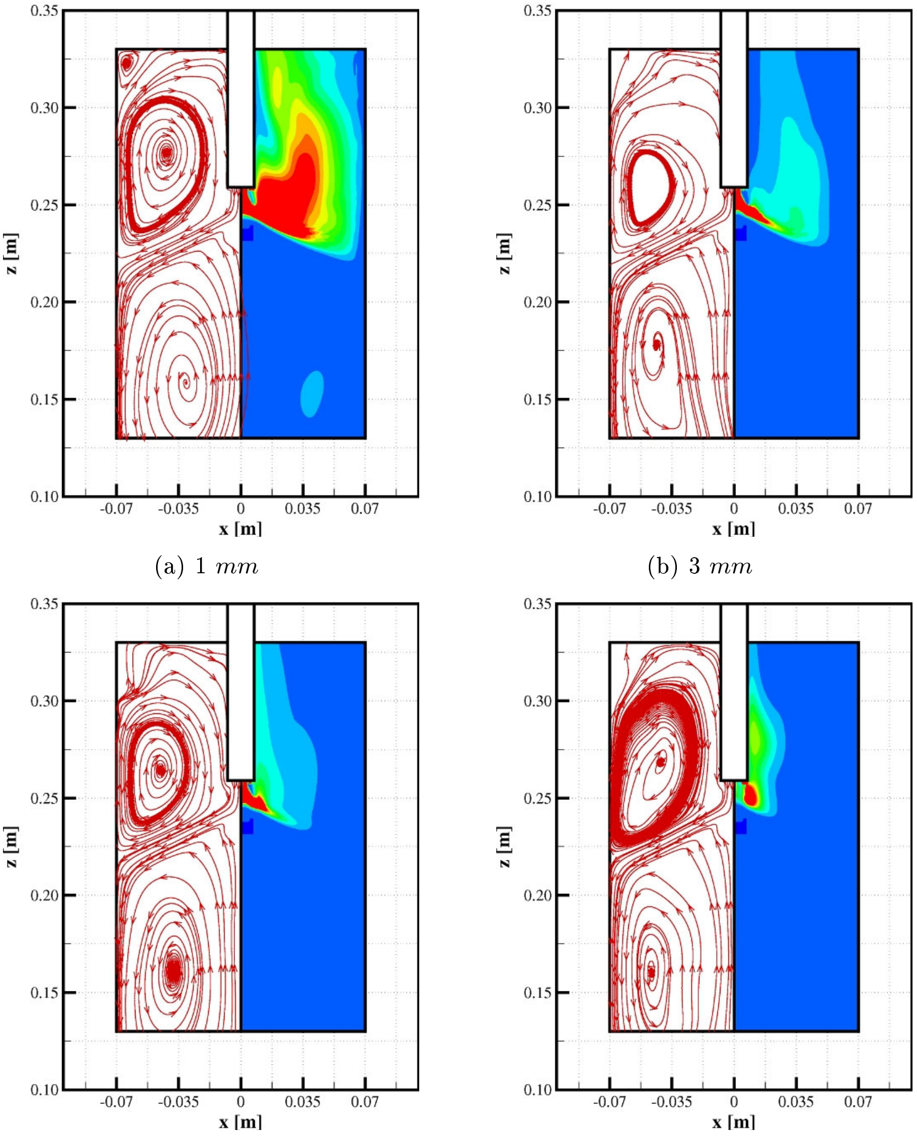

(a) 1 mm

(b) 3 mm

(c) 5 mm

(d) 7 mm

Fig. 6.3: Streamlines of time-averaged velocity and distribution of time-averaged bubble void fraction in the mid-plane parallel to the wide face for different bubble diameters, $B_0 = 0$

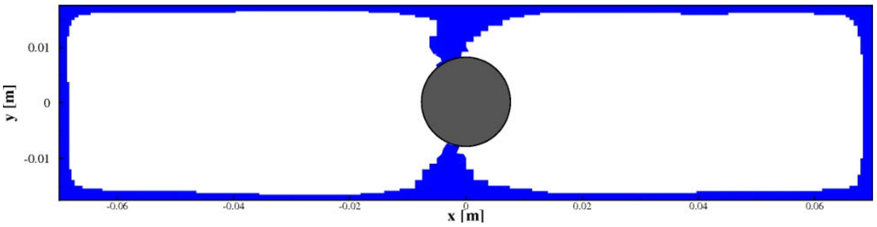

(a) $1mm$

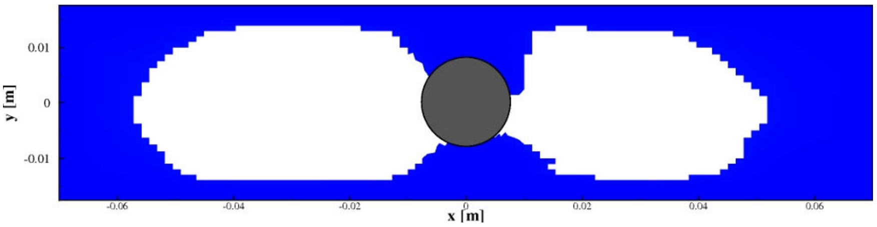

(b) $3mm$

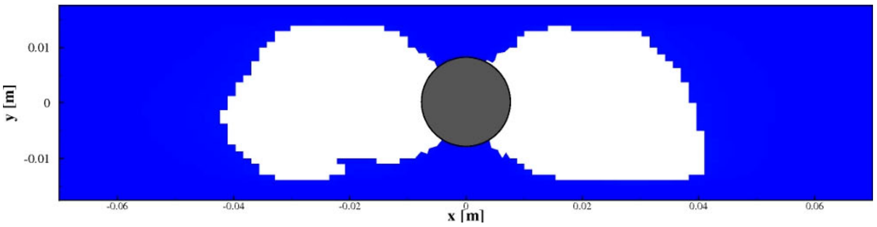

(c) $5mm$

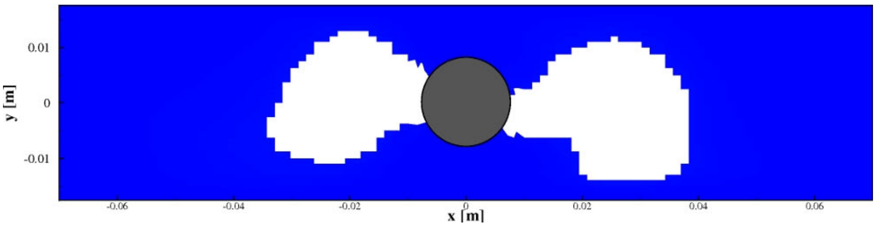

(d) $7mm$

Fig. 6.4: Escape location of bubbles from the top surface for different bubble diameter over time, $B_0 = 0$

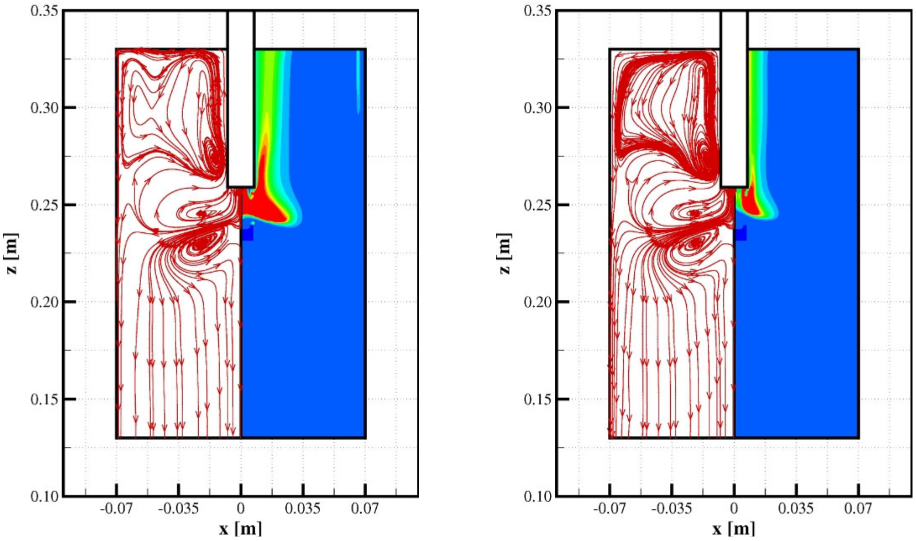

(a) $1mm$ (b) $3mm$

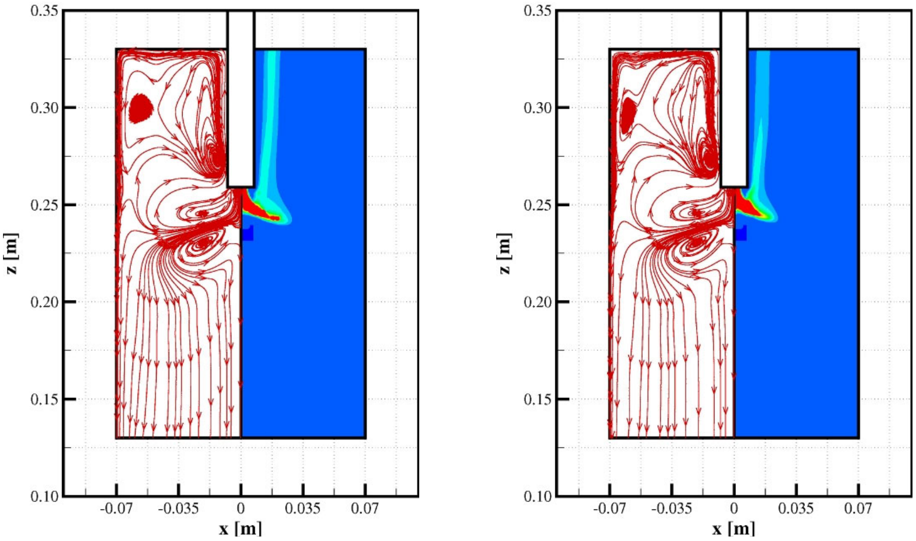

(c) $5mm$ (d) $7mm$

Fig. 6.5: Streamlines of time-averaged velocity and distribution of time-averaged bubble void fraction in the mid-plane parallel to the wide face for different bubble diameters. (electrically conducting wall, $B_0 = 0.31\ T$)

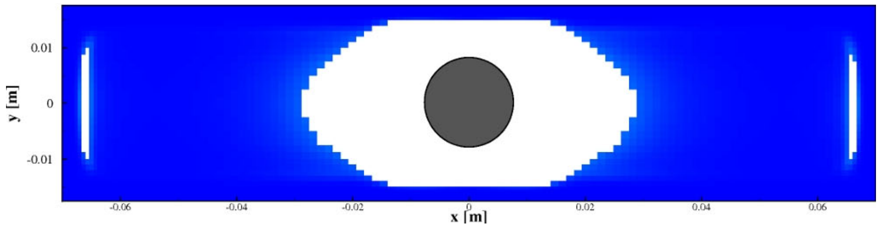

(a) 1 mm

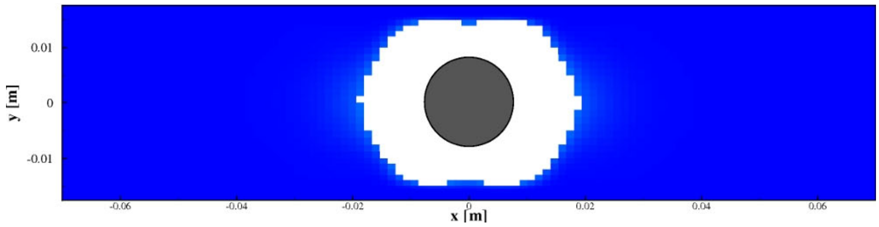

(b) 3 mm

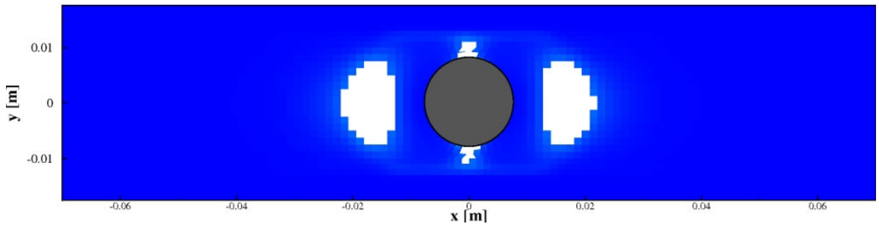

(c) 5 mm

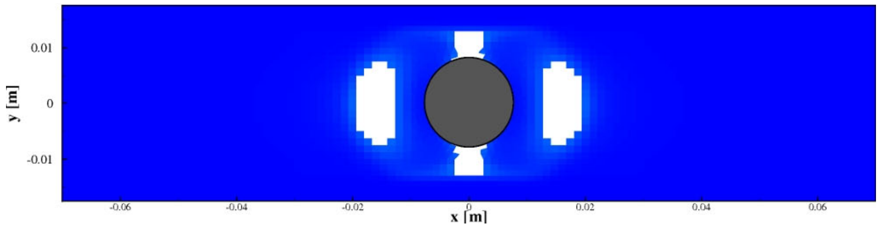

(d) 7 mm

Fig. 6.6: Escape location of bubbles from the top surface for different bubble diameter over time. (electrically conducting wall, $B_0 = 0.31\ T$)

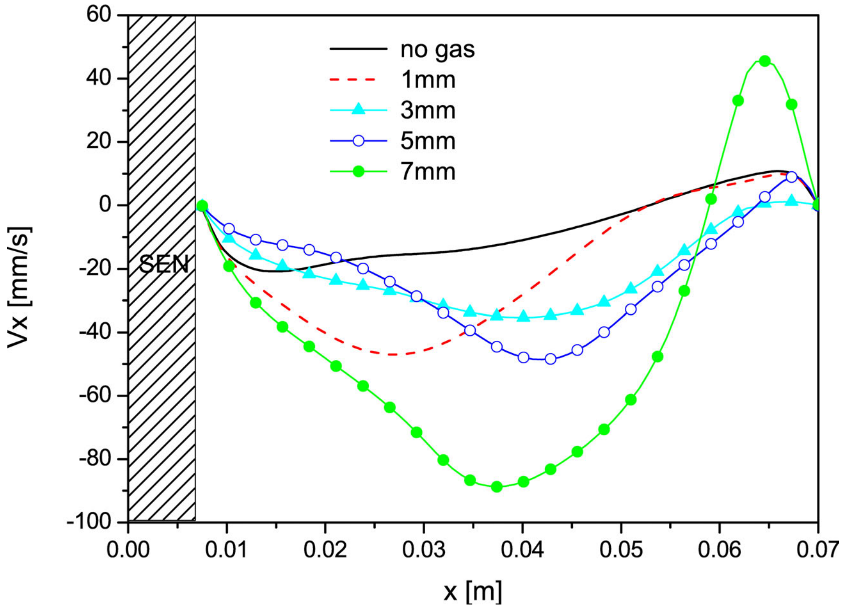

Fig. 6.7: Plot of horizontal velocity on a horizontal center line at $z = 0.328\ m$, $B_0 = 0$

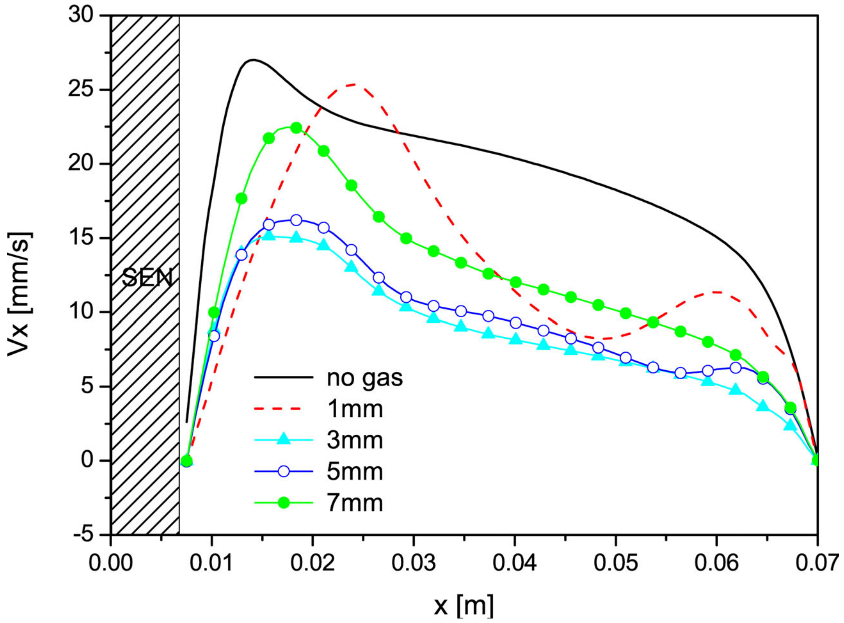

Fig. 6.8: Plot of horizontal velocity on a horizontal center line at $z = 0.328\ m$, $B_0 = 0.31\ T$, electrically conducting wall

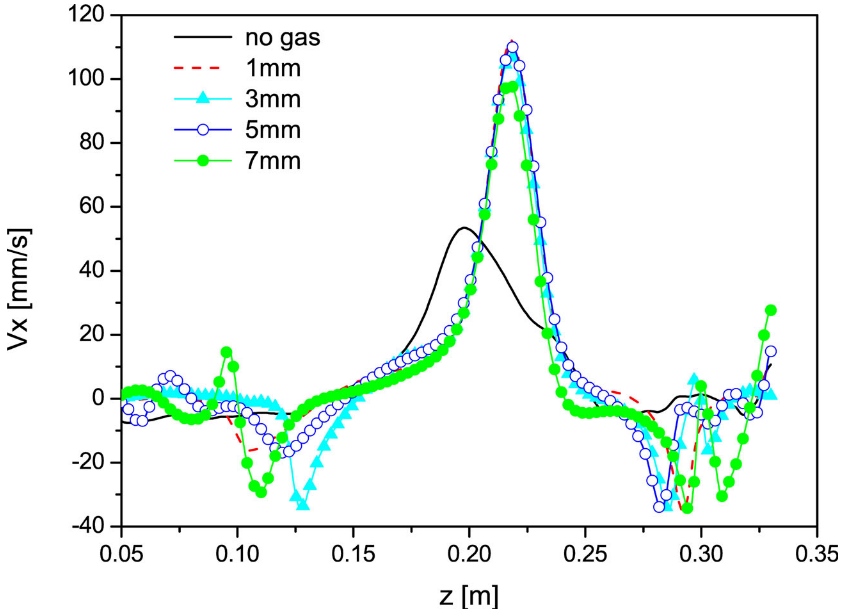

Fig. 6.9: Plot of horizontal velocity on a vertical center line at $x = 0.068\ m$, $B_0 = 0$

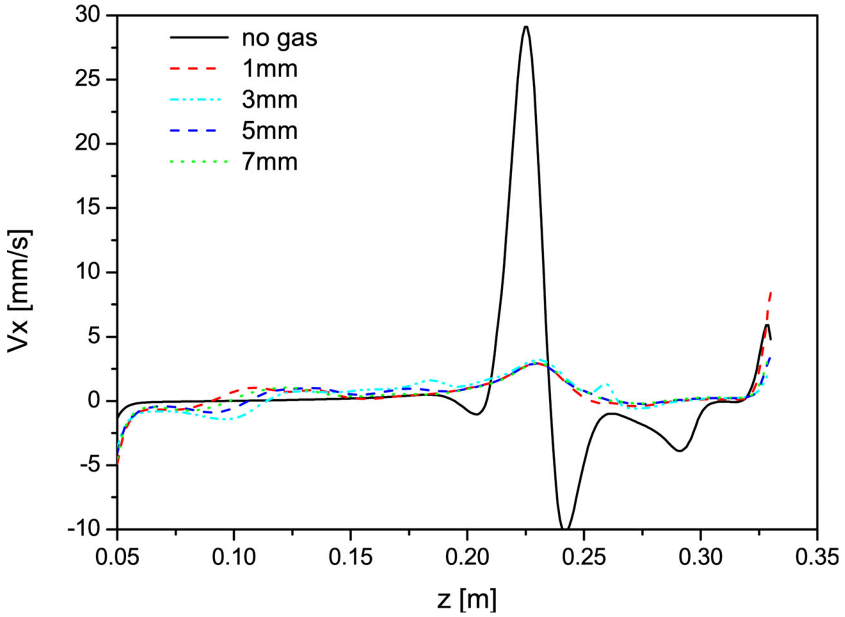

Fig. 6.10: Plot of horizontal velocity on a vertical center line at $x = 0.068\ m$, $B_0 = 0.31\ T$, electrically conducting wall

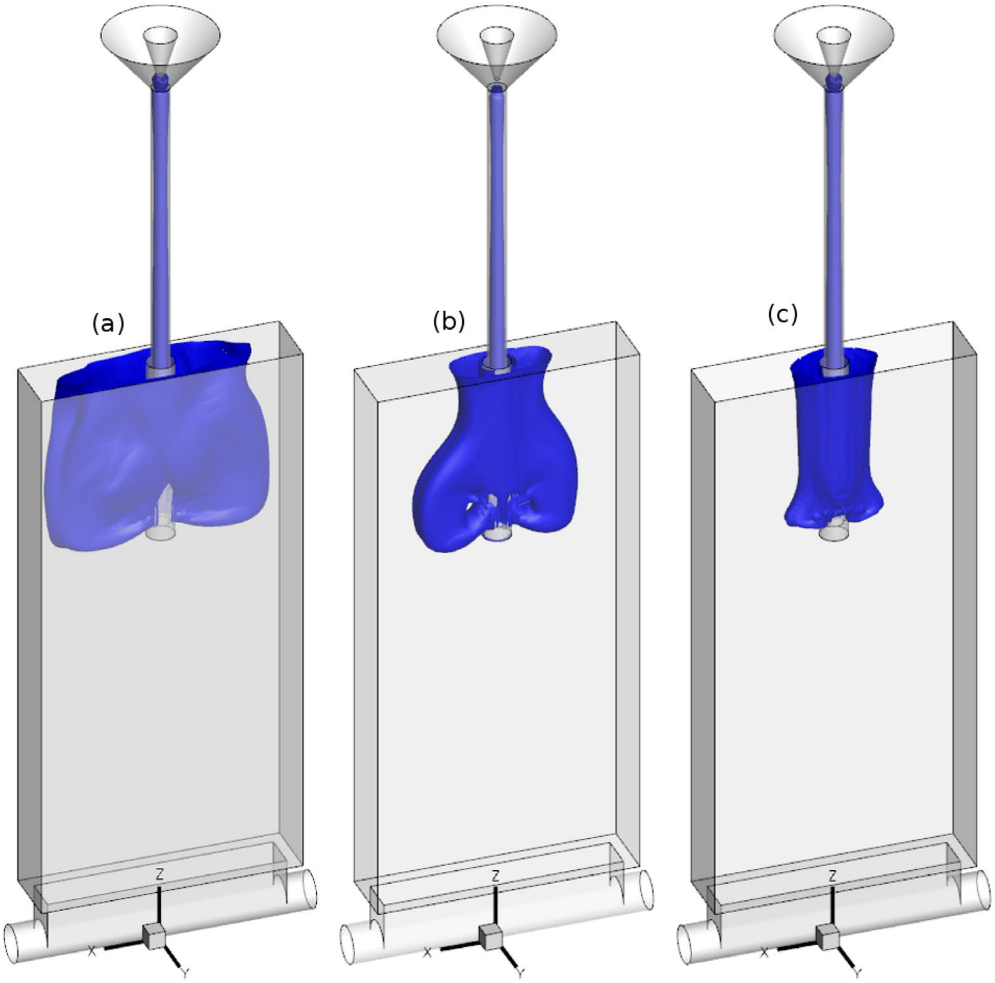

(a) $B_0 = 0$ (b) $B_0 = 0.31\ T$ insu. (c) $B_0 = 0.31\ T$ cond.

Fig. 6.11: 3d distribution of gas void fraction over time varying with electrical wall boundary conditions

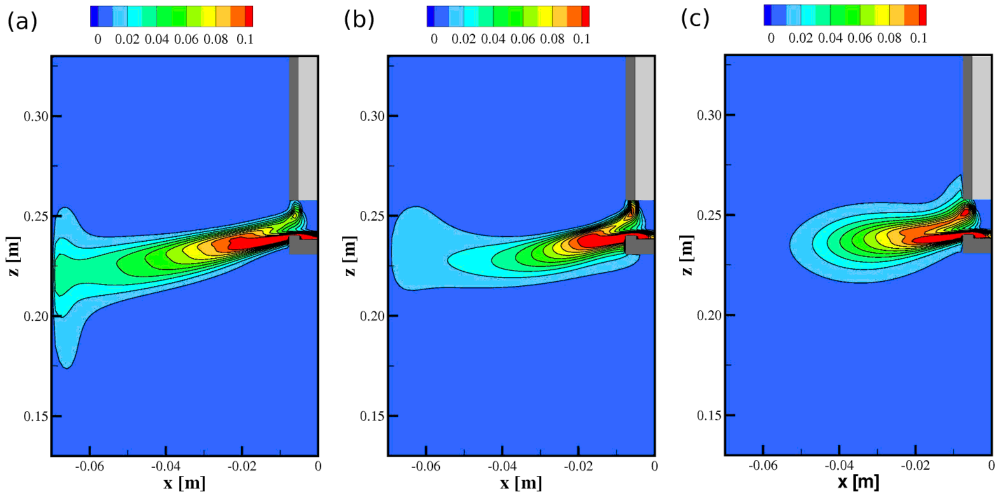

(a) $B_0 = 0$ (b) $B_0 = 0.31\ T$ insu. (c) $B_0 = 0.31\ T$ cond.

Fig. 6.12: Time-averaged contours of turbulent kinetic energy in the mid-plane across the wide face

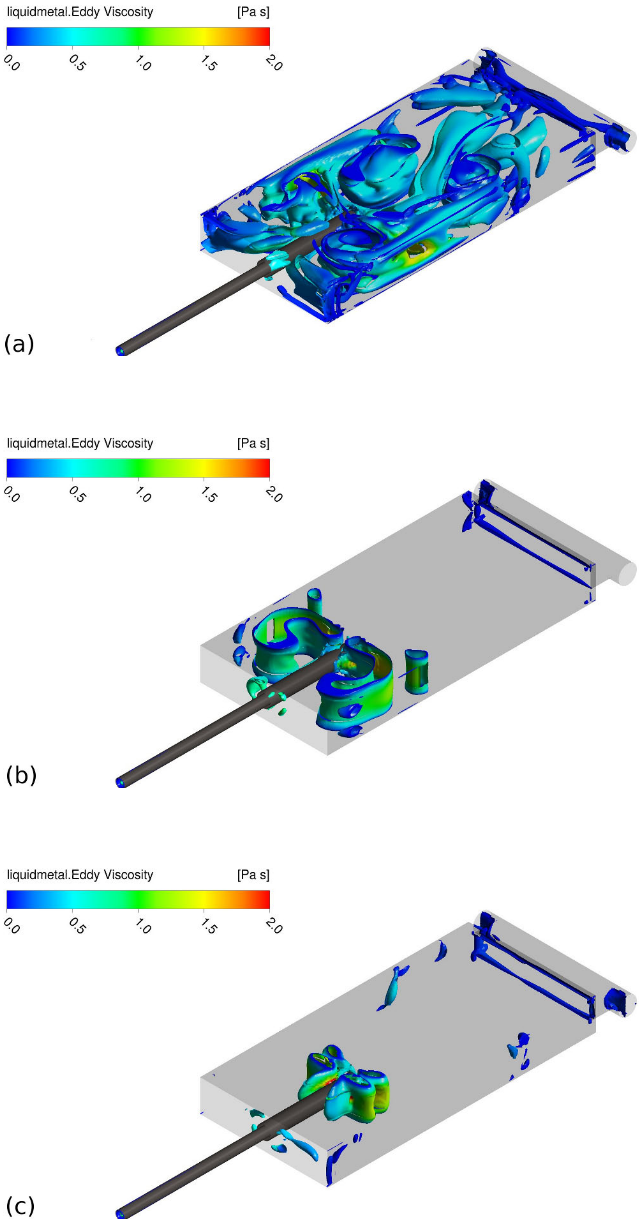
liquidmetal.Eddy Viscosity
[Pa s]
0.0
0.5
1.0
1.5
2.0
(a)
liquidmetal.Eddy Viscosity
[Pa s]
0.0
0.5
1.0
1.5
2.0
(b)
liquidmetal.Eddy Viscosity
[Pa s]
0.0
0.5
1.0
1.5
2.0
(c)

Fig. 6.13: Vortex cores for the different boundary conditions: a) $B_0 = 0$; b) $B_0 = 0.31\ T$ insulating wall; c) $B_0 = 0.31\ T$ conducting wall

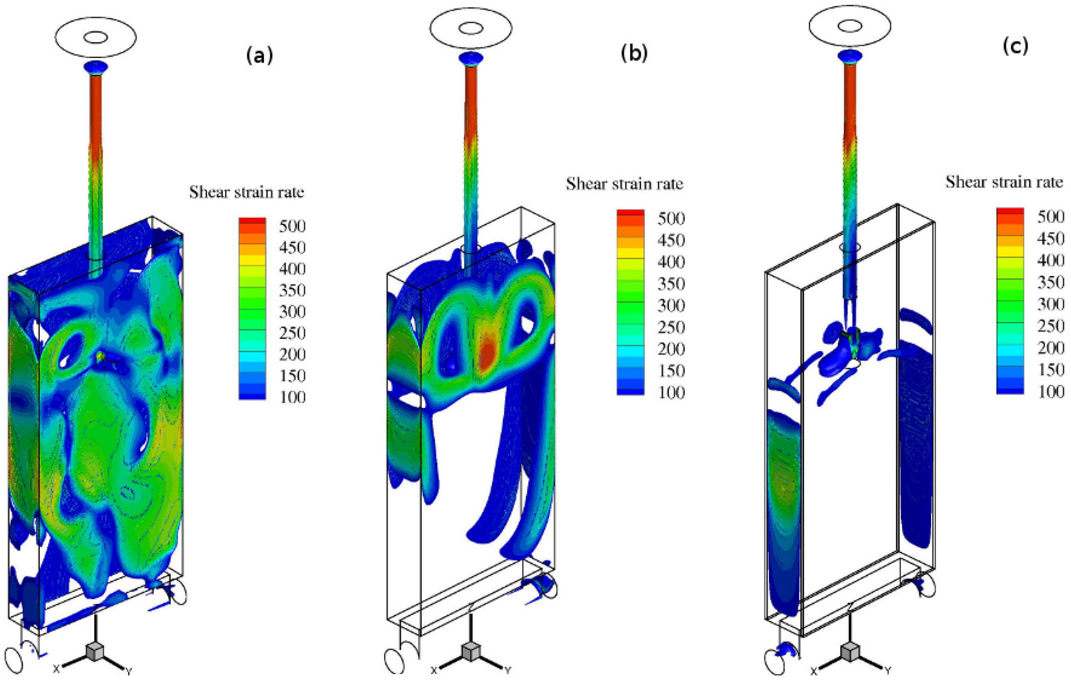
(a)
Shear strain rate
500
450
400
350
300
250
200
150
100
X
Y
(b)
Shear strain rate
500
450
400
350
300
250
200
150
100
X
Y
(c)
Shear strain rate
500
450
400
350
300
250
200
150
100
X
Y

(a) $B_0 = 0$ (b) $B_0 = 0.31\ T$ insu. (c) $B_0 = 0.31\ T$ cond.

Fig. 6.14: Shear strain rate for different boundary conditions

magnetic field. Obviously, the flow is unstable and asymmetric flow is observed for the case without magnetic field. Under the influence of magnetic field, the fluid flow tends to be oscillating for electrically insulating walls, whereas turbulence is strongly suppressed for the case of electrically conducting wall.

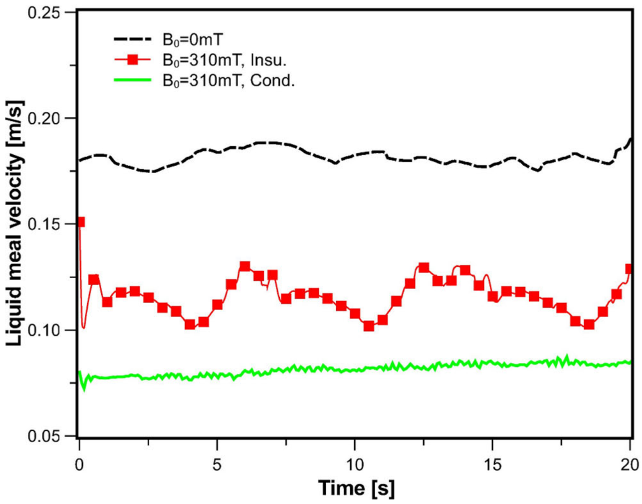

Fig. 6.15: Time series of liquid metal velocity at one position (0.024 m, 0, 0.229 m)

6.2.3 Poly-dispersed particle model for varying magnetic field strength

The right part of figure 6.16 depicts the distribution of the gas void fraction varying with magnetic field intensity. The gas phase injected into the liquid pool considerably accumulate in the upper region at the exit of the nozzle port. We can also observe that gas bubbles mainly float in the upper recirculation zone and finally escape from the top free surface. It is obvious that the magnetic field has a great influence on the distribution of the gas phase by pushing gas bubbles towards the SEN for increasing magnetic field.

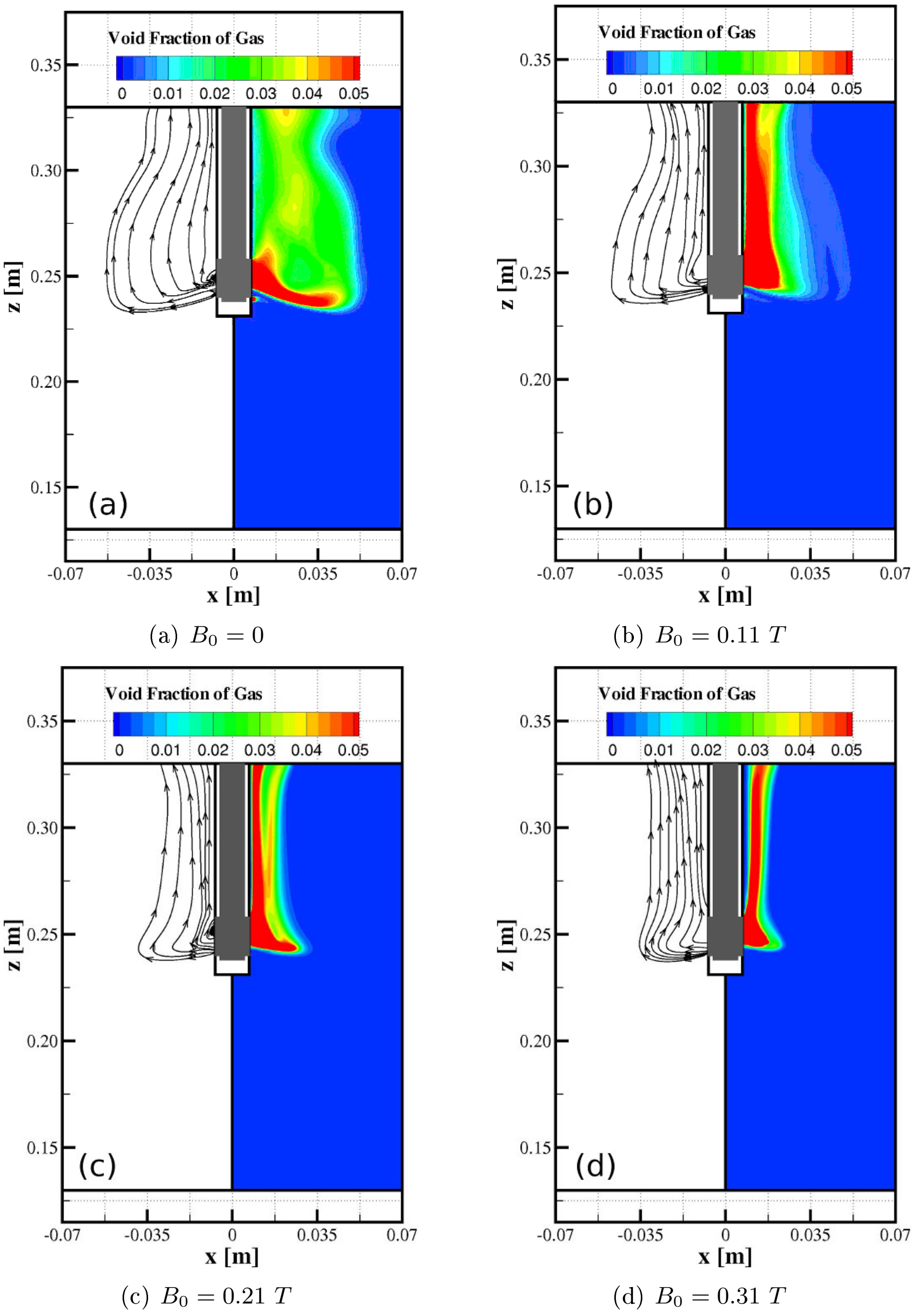

(a) $B_0 = 0$ (b) $B_0 = 0.11\ T$

(c) $B_0 = 0.21\ T$ (d) $B_0 = 0.31\ T$

Fig. 6.16: Distributions of time-averaged gas void fraction in the mid-plane across the wide face for electrically conducting wall (left parts: streamlines of bubbles)

Figure 6.17 shows the combined effect of gas injection and magnetic field on the flow pattern in the mold. As shown in figure 6.17, the external static magnetic field has a strong influence on the jet penetration. The penetration depth of the jet is remarkably decreased for increasing magnetic field and a plug-like flow pattern is obtained in the lower recirculation zone when the magnetic field approaches 0.21 T. In the upper recirculation zone, a reversed back flow is observed and, consequently, it assists in the ascending of gas bubbles. Comparing figure 6.17(d) to figure 6.5, the flow pattern in figure 6.17(d) is similar to those in figures 6.5(a-c). In addition, the jet flow is damped with the increase of the intensity of the magnetic flux.

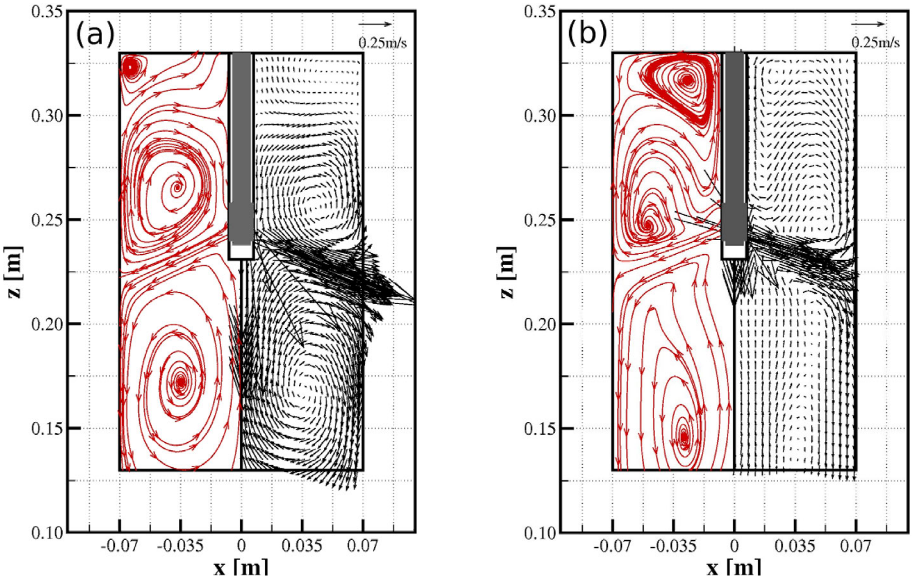

(a) $B_0 = 0$ (b) $B_0 = 0.11\ T$

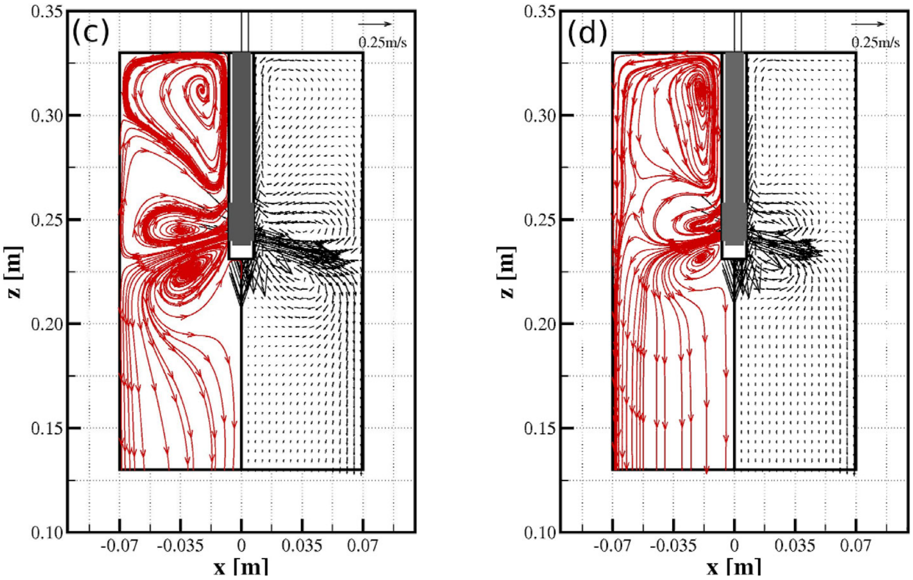

(c) $B_0 = 0.21\ T$ (d) $B_0 = 0.31\ T$

Fig. 6.17: Streamlines and distributions of time-averaged liquid metal velocity in the mid-plane across the wide face for electrically conducting wall

Figure 6.18 shows the distribution of the bubble size fraction on a horizontal centerline at $z = 0.28\ m$ without magnetic field. Two peaks show that bubbles widespread from the SEN to the narrow face and concentrate in the vicinity of the SEN and the narrow face. The bubble size fraction decreases with the increase of the bubble diameter. The distribution of the bubble size fraction is mainly in the range from Group 1 to 6. The relative distribution of bubble size fraction on a horizontal centerline at $z = 0.28\ m$ with a magnetic field of $B_0 = 0.31\ T$ is shown in figure 6.19. Owing to the reversed flow near the SEN (Figure 6.17), gas bubbles are mainly distributed in the vicinity of SEN where breakup and coalesce of bubbles took place. The relationship between bubble size fraction and bubble diameter has the same tendency as in the case without magnetic field. The distribution of bubble size fraction is mainly in the range from Group 1 to 5, which supports the similarity of the flow structure in figure 6.17(d) and figure 6.5.

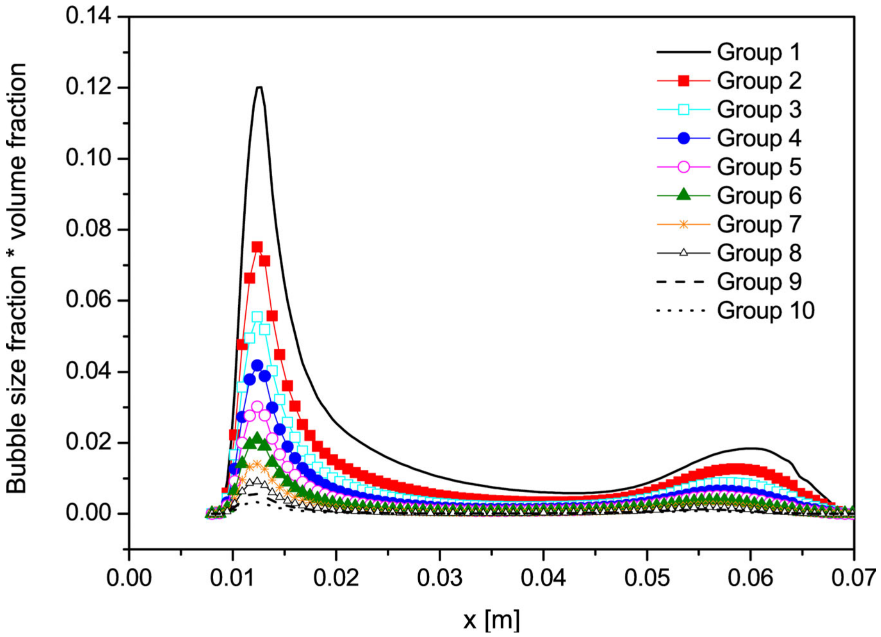

Fig. 6.18: Distribution of bubble size fraction on a horizontal centerline at $z = 0.28\ m$ without magnetic field

6.2.4 Influence of the electrical wall conductance ratio

The effect of the wall conductance ratio on the flow pattern in the mold is shown in figure 6.20 and 6.21 for the poly-dispersed particle model. The double-roll flow around the jets was restricted to the jet area. Meanwhile, a reversed flow emerged in the upper recirculation zone where the shape and position of eddies are dependent on the wall conductance ratio. In the lower recirculation zone, flow pattern displays a plug-like structure. The quantitative comparison of the liquid metal velocity was made on a vertical centerline at $x = 0.069\ m$ (see figure 6.21). The liquid metal velocity in the lower recirculation zone is larger than that in the upper recirculation zone. In particular, the liquid metal velocity was increased remarkably with the increases of the wall conductance ratio. It indicates that low in the region of the solidified front can be intensified at high wall conductance ratio, which may play a key role on the strand micro-structure and positive subsurface defects.

6.3 Discussion and summary

In a steel continuous casting process, generally, argon gas is injected in the mold through the SEN. In this chapter, the effects of gas injection and electromagnetic brake on the fluid flow in the mold were studied using both the mono-dispersed particle model and the poly-dispersed particle model. Simulation results show that the distribution of the gas phase is dependent on the bubble diameter by using the mono-dispersed particle model (see figure 6.3). Considering the effect of complex flow, injection method, heat transfer, etc. to the bubble size, the mono-dispersed particle model is obviously improper to simulate such case. However, the poly-dispersed particle model treats the gas phase as bubbles with different bubble diameters, thus providing a new way to simulate the two-phase flow in the continuous casting process. Comparing figure 6.16(a) (poly-dispersed particle model) to figure 6.3 (mono-dispersed particle model), the distribution of the gas phase presents pronouncing differences. The further

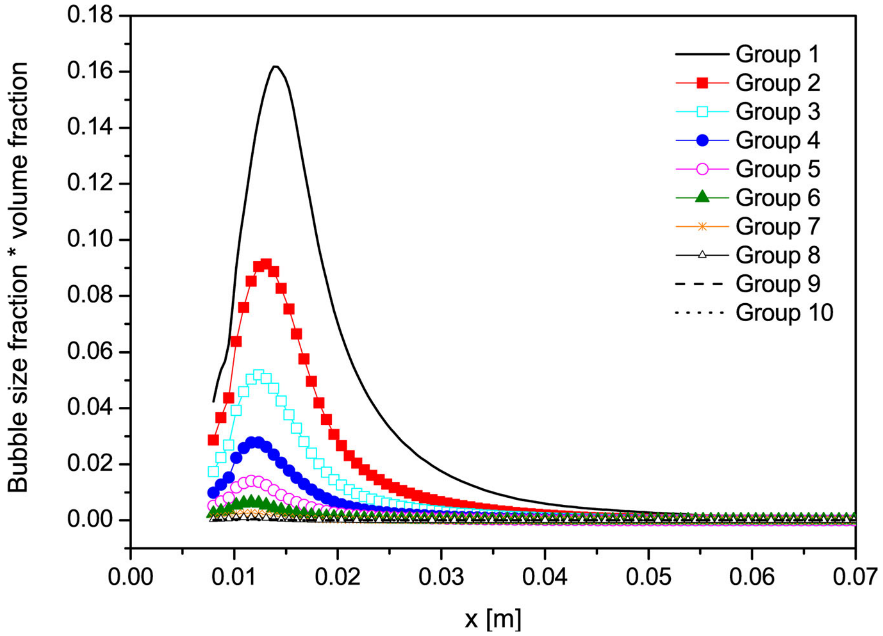

Fig. 6.19: Distribution of bubble size fraction on a horizontal centerline at $z = 0.28\ m$. (electrically conducting wall, $B_0 = 0.31\ T$)

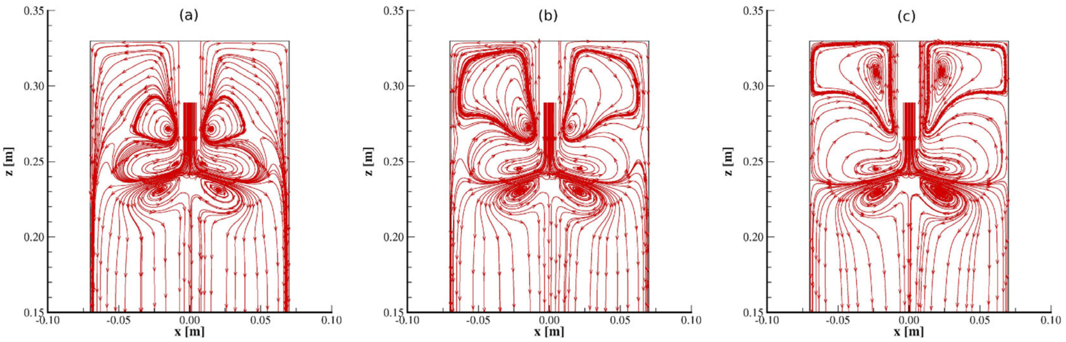

(a) $C_W = 0.0665$ (b) $C_W = 0.133$ (c) $C_W = 0.233$

Fig. 6.20: Time-averaged streamlines of liquid metal velocity in the mid-plane for different wall conductance ratio at $B_0 = 0.31\ T$

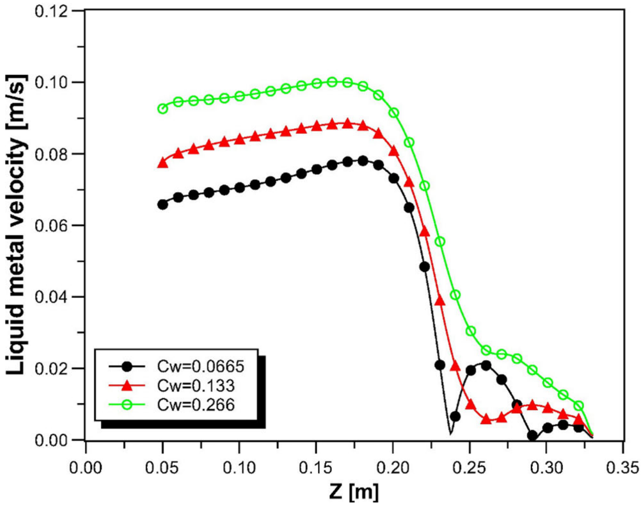

Fig. 6.21: Time-averaged liquid metal velocity along the vertical centerline at 1 mm to the narrow face for different wall conductance ratios

comparison was made, see figure 6.17(a) and figure 6.5, in the presence of an external magnetic field ($B_0 = 0.31\ T$, electrically conducting wall). It shows that the flow structure in figure 6.17(d) is closely similar to that in figure 6.5(b) and extremely different to that in figure 6.5(d). It indicates that the breakup and coalesce of bubbles play a great role in this complex flow. Moreover, the thickness of the solidified shell (related to the wall conductance ratio) has a great impact on the flow structure in the mold, see figure 6.20. In particular, the flow is intensified at the solidified front for increasing thickness of the solidified shell, see figure 6.21. To simulate the continuous casting process with EMBr, the effect of the solidified shell can not be neglected.

The overall results show that the gas injection and the magnetic field play an important role on the flow pattern. Moreover, to optimize the flow pattern in the industrial casting process, several crucial factors must be taken into account simultaneously. The conclusions are drawn as follows:

1. Simulation results show that the distributions of gas phase depend on the bubble diameter by using the mono-dispersed particle model. To deal with the bubble flow with different bubble diameters, the poly-dispersed particle model gives rise to more accurate predictions than the mono-dispersed particle model.

2. The flow pattern in the mold is sensitive to the strength of a static magnetic field and the wall conductance ratio. An improperly employed magnetic field may cause severe side-effects, such as additional large eddies or a deepening of the penetration depth. Considering the solidified shell in the mold cavity, the electrical wall boundary condition is of importance to be taken into account in order to get more accurate predictions.

3. Further work will concentrate on numerical simulations in comparison with liquid metal experiments considering gas injection and electromagnetic field application.

7 Summary

In general, the fluid flow in a metallurgical plant is highly turbulent and presents a complex coupling with heat transfer, phase transfer, chemical reaction, momentum transportation, etc. Owing to the complexity and limits of reliable measuring techniques, computational models of fluid flow are useful tools to study and quantify these problems. The overall objective is concentrated on investigating the effects of electromagnetic brake and gas injection on the fluid flow in a continuous casting slab mold numerically, and making verifications using data of the small Liquid Metal Model for Continuous Casting of steel (mini-LIMMCAST).

In the current work, a DC static magnetic field is implemented on a low meting-point liquid metal (GaInSn) to control the flow pattern in the mold cavity (mini-LIMMCAST) with a so called EMBr. The Hartmann boundary layer of thickness $\delta = O(Ha^{-1})$ is a well-known property of magnetodydrodynamic (MHD) flows with electrically insulating walls. Hartmann layers are numerically considered by refining the mesh near the wide and narrow faces in the mold. Numerical calculations were performed by means of the software package ANSYS CFX with an implemented RANS-SST turbulence model. One advantage is the possibility to use the SST $k-\omega$ model as a low-Re turbulence model without any extra damping functions. The SST formulation switches to a $k-\epsilon$ behavior in the free-stream region and thereby avoids the common $k-\omega$ problem that the model is too sensitive to the properties of the inlet free-stream turbulence. In addition, the SST $k-\omega$ turbulence model is considered to predict the fluid flow inside the boundary layers more accurately than the $k-\epsilon$ turbulence model provided that the nondimensional wall distance y^+ is less than 1.

The application of a strong DC magnetic field gives rise to a magnetic dissipation term called as Joule dissipation. The turbulent flow undergoes a reorganization as consequence of the conservation of angular momentum against the background of a continuous decay of turbulent kinetic energy. The nonisotropic nature of the MHD turbulence was taken into account by specific modifications of the turbulence model as proposed by [89].

The numerical results were validated by flow measurements at the mini-LIMMCAST facility. The comparison between our numerical calculations and the experimental results displays a good agreement; in particular, the peculiar phenomenon of an excitation of nonsteady, nonisotropic, large-scale flow perturbations caused by the application of the DC magnetic field is explained successfully. Another important result of our study is the feature that the electrical boundary conditions, namely the wall conductance ratio, have a serious influence on the mold flow while it is exposed to an external magnetic field.

Bibliography

[1] S.P. Antal, R.T. Lahey, and J.E. Flaherty. “Analysis of phase distribution in fully developed laminar bubbly two-phase flow”. In: *Int. J. Multiphase Flow* 7 (1991), pp. 635 –652.

[2] Worldsteel Association, ed. *Steel Statistical Yearbooks.* Worldsteel Association, 2010.

[3] H. Bai and B.G. Thomas. “Effects of clogging, argon injection, and continuous casting conditions on flow and air aspiration in submerged entry nozzles”. In: *Metall. Mater. Trans. B* 32 (2001), pp. 707 –722.

[4] H. Bai and B.G. Thomas. “Turbulent flow of liquid steel and argon bubbles in slide-gate tundish nozzles: Part I. Model developments and validation”. In: *Metall. Mater. Trans. B* 32 (2001), pp. 253 –267.

[5] H. Bai and B.G. Thomas. “Turbulent flow of liquid steel and argon bubbles in slide-gate tundish nozzles: Part II. Effect of operation conditions and nozzle design”. In: *Metall. Mater. Trans. B* 32 (2001), pp. 269 –283.

[6] K.E. Barret. “Duct flow with a transverse magnetic field at high Hartmann numbers”. In: *Int. J. Numer. Meth. Engng* 50 (2001), pp. 1893 –1906.

[7] M. Lopez de Bertodano. “Turbulent Bubbly Flow in a Triangular Duct”. PhD thesis. Ph. D. Thesis, Rensselaer Polytechnic Institute, Troy New York, 1991.

[8] E.C. Brouilette and P.S. Lykoudis. “Magneto-fluid-mechanic channel flow. I. Experiment”. In: *Phys. Fluids* 10 (1967), pp. 995 –1001.

[9] U. Burr et al. “Magnetohydrodynamic convection in a vertical slot with horizontal magnetic field”. In: *J. Fluid Mech.* 475 (2003), pp. 108 –113.

[10] R. Clift, J. R. Grace, and M. E. Weber. *Bubbles, Drops and Particles.* Ed. by New York. Academic Press, 1978.

[11] United States Steel Corporation et al., eds. *The making, Shaping and Treating of Steel.* US Steel, 1985.

[12] K. Cukierski and B.G. Thomas. “Flow Control with Local Electromagnetic Braking in Continuous Casting of Steel Slabs”. In: *Metall. Mater. Trans. B* 39 (2008), pp. 94 –107.

[13] P.A. Davidson. *An Introduction to Magnetohydrodynamics.* Cambridge University Press, 2001.

[14] P.A. Davidson. “Magnetic damping of jets and vortices”. In: *J. Fluid Mech.* 229 (1995), pp. 153 –186.

[15] N.G. Deen, T. Solberg, and B.H. Hjertager. “Large eddy simulations of the gas liquid flow in a square cross-sectioned bubble column”. In: *Chem. Eng. Sci.* 56 (2001), pp. 6341 –6349.

[16] M.T. Dhotre and J.B. Joshi. “Design of a gas distributor: three-dimensional CFD simulation of a coupled system consisting of a gas chamber and a bubble column”. In: *Chem. Eng. J.* 125 (2007), pp. 149 –163.

[17] D.A. Drew. “Averaged field equations for two-phase media”. In: *Stud. Appl. Math.* 50 (1997), pp. 133 –165.

[18] S. Eckert, G. Gerbeth, and O. Lielausis. “The behavior of gas bubbles in a turbulent liquid metal magnetohydrodynamic flow. Part I: Dispersion in quasi-two-dimensional magnetohydrodynamic turbulence”. In: *Int. J. Multiphase Flow* 26 (2000a), pp. 45 –66.

[19] S. Eckert et al. “MHD turbulence measurements in a sodium channel flow exposed to a transverse magnetic field”. In: *Int. J. Heat Fluid Flow* 22 (2001), pp. 358 –364.

[20] D.A. Ervin and G. Tryggvason. “The rise of bubbles in a vertical shear flow”. In: *J. Fluid Eng.* 19 (1997), pp. 443 –449.

[21] G.M. Evans and G.J. Jameson. “Hydrodynamics of a plunging liquid jet bubble column”. In: *Chemical Engineering Research and Design* 73(6) (1995), pp. 679 –684.

[22] G.M. Evans et al. “Gas dispersion through porous nozzles into down-flowing liquids”. In: *Chemical Engineering Science* 54 (1999), pp. 4861 –4867.

[23] R. J. Fruehan, United States Steel Co., and American Society for Metals, eds. *The making, Shaping and Treating of Steel.* AISE Steel Foundation, 1998.

[24] Y.M. Gelfgat, O.A. Lielausis, and E.W. Sherbinin. *Liquid Metal under the Action of Electromagnetic Forces.* Zinatne, Riga, 1976.

[25] P. Gherson and P. S. Lykoudis. “Local Measurements in two-phase liquid-metal magneto-fluid-mechanic flow”. In: *J. Fluid Mech.* 147 (1984), pp. 81 –104.

[26] H. Harada et al. “Effect of Magnetic Field Conditions on the Electromagnetic Braking Efficiency”. In: *ISIJ Int.* 41 (2001), pp. 1236 –1244.

[27] F.H. Harlow and P.I. Nakayama. *Transport of turbulence energy decay rate.* Tech. rep. Los Alamos Sicence Lab., LA-3854, 1968.

[28] J. Hartmann. “Theory of the laminar flow of an electrically conductive liquid in a homogeneous magnetic field”. In: *K. Dan. Vidensk. Selsk. Mat. Fys. Medd* 15(6) (1937), pp. 21 –28.

[29] J. Hartmann and F. Lazarus. “Experimental investigations on the flow of mercury in a homogeneous magnetic field”. In: *K. Dan. Vidensk. Selsk. Mat. Fys. Medd* 15(7) (1937), pp. 41 –45.

[30] A. Idogawa et al. “Control of molten steel flow in continuous casting mold by two static magnetic fields imposed on whole width”. In: *Mater. Sci. Eng. A* 173 (1993), pp. 293 –297.

[31] M. Iguchi and T. Chihara. “Water model study of the frequency of bubble formation under reduced and elevated pressures”. In: *Metall. Mater. Trans. B* 29 (1998), pp. 761 –775.

[32] A. Inoue et al. “Characteristics of flow and heat transfer in air-mercury two-phase stratified flow under a vertical magnetic field”. In: *Exp. Therm. Fluid Sci.* 8 (1994), pp. 46 –57.

[33] M. Ishii and N.Zuber. “Drag Coefficient and Relative Velocity in Bubbly, Droplet or Particulate Flows”. In: *AIChE J.* 25 (1979), pp. 843 –855.

[34] A. Freeman Major Jacob and J. Roy Christopher. “Verification and Validation of RANS Turbulence Models in Commercial Flow Solvers”. In: *50th AIAA Aerospace Sciences Meeting including the New Horizons Forum and Aerospace Exposition* 09 - 12 January (2012), AIAA 2012–0462.

[35] H.A. Jakobsen et al. “Modeling of vertical bubble-driven flows”. In: *Ind. Eng. Chem. Res.* 36 (1997), pp. 4052 –4074.

[36] H.C. Ji and R.A. Gardner. “Numerical analysis of turbulent pipe flow in a transverse magnetic field”. In: *Int. J. Heat Mass Trans.* 40 (1997), pp. 1839 –1851.

[37] W.P. Jones and B.E. Launder. “The Prediction of Laminarization with a Two-Equation Model of Turbulence”. In: *International Journal of Heat and Mass Transfer* 15 (1972), pp. 301 –314.

[38] S. Kenjeres and K. Hanjalic. “On the implementation of effects of Lorentz force in turbulence closure models”. In: *Int. J. Heat Mass Trans.* 21 (2000), pp. 329 –337.

[39] D.S. Kim, W.S. Kim, and K.H. Cho. “Numerical Simulation of the Coupled Turbulent Flow and Macroscopic Solidification in Continuous Casting with Electromagnetic Brake”. In: *ISIJ Int.* 40 (2000), pp. 670 –676.

[40] K. Kitamura and M. Hirata. “Turbulent heat and momentum transfer for electrically conducting fluid flowing in two-dimensional channel under transverse magnetic field”. In: *In: Proceedings of the 6th Int. Heat Transfer Conference, vol. 3. Toronto, Canada.* 1978.

[41] H. Kobayashi. “Large eddy simulation of magnetohydrodynamic turbulent duct flow”. In: *Phys. Fluids* 20 (2008), p. 015102.

[42] S.G. Kollberg, H.R. Hackl, and P.J. Hanley. “Improving Quality of Flat Rolled Products Using Electromagnetic Brake (EMBr) in Continuous Casting”. In: *Iron Steel Eng.* 73 (1996), pp. 24 –28.

[43] D.S. Krasnov et al. “Numerical study of the instability of the Hartmann layer”. In: *J. Fluid Mech.* 504 (2004), pp. 121 –183.

[44] E. Krepper et al. “Experimental and numerical studies of void fraction distribution in rectangular bubble columns”. In: *Nucl. Eng. Des.* 237 (2007), pp. 399 –408.

[45] E. Krepper et al. “The inhomogeneous MUSIG model for the simulation of polydispersed flows”. In: *Nuclear Engineering and Design* 238 (2008), pp. 1690 –1702.

[46] B. Li, T. Okane, and T. Umeda. “Modeling of molten metal flow in a continuous casting process considering the effects of argon gas injection and static magnetic-field application”. In: *Metall. Mater. Trans B* 31B (2000), pp. 1491 –1503.

[47] B. Li and F. Tsukihashi. “Effects of Electromagnetic Brake on Vortex Flows in Thin Slab Continuous Casting Mold”. In: *ISIJ Int.* 46 (2006), pp. 1833 –1838.

[48] B.W. Li et al. “Influences of casting speed and sen depth on fluid flow in the funnel type mold of a thin slab caster”. In: *Acta Metallurgica Sinica (English Letters)* 20 (2007), pp. 15 –26.

[49] D. Lucas, E. Krepper, and H.-M. Prasser. “Use of models for lift, wall and turbulent dispersion forces acting on bubbles for poly-disperse flows”. In: *Chem. Eng. Sci.* 62 (2007), pp. 4146 –4157.

[50] D. Lucas, H.-M. Prasser, and A. Manera. “Influence of the lift force on the stability of a bubble column”. In: *Chem. Eng. Sci.* 60 (2005), pp. 3609 –3619.

[51] D. Lucas and A. Tomiyama. “On the role of the lateral lift force in poly-dispersed bubbly flows”. In: *Int. J. Multiphase Flow* 37 (2011), pp. 1178 –1190.

[52] S. Luo. “Application of the MUSIG model to bubbly flows”. In: *AEA Technology* (1996), AEAT–1096.

[53] S.M. Luo and H. Svendsen. “Theoretical Model for Drop and Bubble Breakup in Turbulent Dispersions”. In: *AIChE Journal* 42 (1996), pp. 1225 –1233.

[54] P.S. Lykoudis and E.C. Brouillette. “MagnetoFluidMechanic Channel Flow. II. Theory”. In: *Phys. Fluids* 10 (1967), pp. 1002 –1007.

[55] N.A. McPherson et al. “Continuous casting refractories for improved operating and quality performance”. In: *Iron making and steel making* 17 (1990), pp. 43 –45.

[56] F.R. Menter. “Two-Equation Eddy-Viscosity Turbulence Models for Engineering Applications”. In: *AIAA Journal* 32(8) (1994), pp. 1598 –1605.

[57] K. Mohanarangam, T.V. Nguyen, and D.W. Stephens. “Evaluation of two-equation turbulence models in a laboratory-scale thickener feedwell”. In: *Seventh International Conference on CFD in the Minerals and Process Industries* 9-11 December (2009), pp. 1 –5.

[58] P. Moresco and T. Alboussierre. “Experimental study of the instability of the Hartmann layer”. In: *J. Fluid Mech.* 504 (2004), pp. 167 –182.

[59] Y. Mori, K. Hijikata, and I. Juriyama. “Experimental study of bubble motion in mercury with and without magnetic field”. In: *Winter Annual Meeting of ASME, Heat Transfer Division, New York, 5 December (ASME 76-WA/HT-65).* 1976.

[60] M.Prince and H. Blanch. “Bubble Coalescence and Break-Up in Air-Sparged Bubble Columns”. In: *AIChE Journal* 36 (1990), pp. 1485 –1499.

[61] J. Nagai et al. “Steel Flow Control in a High-Speed Continuous Slab Caster Using an Electromagnetic Brake”. In: *Iron Steel Eng.* 61 (1984), pp. 41 –47.

[62] A. Ramos-Banderas et al. “Dynamics of two-phase downwards flows in submerged entry nozzles and its influence on the two-phase flow in the mold”. In: *Int. J. of Multiphase Flow* 31 (2005), pp. 643 –665.

[63] R. Sanchez-Perez et al. “A physical model for the two-phase flow in a continuous casting mold”. In: *ISIJ Int.* 43 (2003), pp. 637 –646.

[64] R. Sanchez-Perez et al. “Dynamics of coupled and uncoupled two-phase flows in a slab mold”. In: *Metall. Mater. Trans. B.* 35 (2004), pp. 85 –99.

[65] Y. Sato, M. Sadatomi, and K. Sekoguchi. “Momentum and heat transfer in two-phase bubble flow. I. Theory”. In: *Int. J. Multiphase Flow* 7 (1981), pp. 167 –177.

[66] Y. Sato and K. Sekoguchi. “Liquid velocity distribution in two-phase bubbly flow”. In: *Int. J. Multiphase Flow* 2 (1975), pp. 79 –95.

[67] V. Shatrov and G. Gerbeth. “Marginal turbulent magnetohydrodynamic flow in a square duct”. In: *Phys. Fluids* 22 (2010), p. 084101.

[68] H. Shen et al. “Effect of electromagnetic brake on fluid flow in continuous slab casting mould”. In: *Int. J. Cast Metals Res.* 18 (2005), pp. 209 –213.

[69] Y.Y. Sheng and G.A. Irons. “Measurement and modeling of turbulence in the gas/liquid two-phase zone during gas injection”. In: *Metall. Trans. B* 24 (1993), pp. 695 –705.

[70] K. Shibasaki, K. Ueno, and T. Tagawa. “Computation of a rising bubble in an enclosure filled with liquid metal under vertical magnetic fields”. In: *ISIJ Int.* 50 (2010), pp. 363 –370.

[71] Y. Shimomura. “Statistical Analysis of Magnetohydrodynamic Turbulent Shear Flows at Low Magnetic Reynolds Number”. In: *J. Phys. Soc. Jpn.* 57 (1988), pp. 2365 –2385.

[72] S.M. Shin and I.S. Kang. “Effects of magnetic field on the shape of a bubble in a uniaxial straining flow”. In: *Int. J. Multiphase Flow* 28 (2002), pp. 105 –125.

[73] O. Simonin and P.L. Viollet. “On the computation of turbulent two-phase flows in Eulerian formulation”. In: *Proceedings EUROMECH 234 Conference, Toulouse, France.* 1998.

[74] B.L. Smith. “On the modelling of bubble plumes in a liquid pool”. In: *Appl. Math. Modell.* 14 (1998), pp. 67 –76.

[75] S. Smolentsev et al. “Application of the “K-e” model to open channel flows in a magnetic field”. In: *International Journal of Engineering Science* 40 (2002), pp. 693 –711.

[76] J. Sommeria and R. Moreau. “Why, how, and when, MHD turbulence becomes two-dimensional”. In: *J. Fluid Mech.* 118 (1982), pp. 507 –518.

[77] P.R. Spalart and S. R. Allmaras. “A One-Equation Turbulence Model for Aerodynamic Flows”. In: *La Recherche Aerospatiale* 1 (1994), pp. 5 –21.

[78] B. Sreenivasan and T. Alboussiere. “Evolution of a vortex in a magnetic field”. In: *Eur. J. Mech. B/Fluids.* 19 (2000), pp. 403 –421.

[79] T. Tagawa, G. Authie, and R. Moreau. “Buoyant flow in long vertical enclosures in the presence of a strong horizontal magnetic field. Part 1. Fully-established flow”. In: *Eur. J. Mech. B/Fluids.* 21 (2002), pp. 383 –398.

[80] T. Tagawa and H. Ozoe. “Enhancement of Heat Transfer Rate by Application of a Static Magnetic Field During Natural Convection of Liquid Metal in a Cube”. In: *J. Heat Trans.* 119 (1997), pp. 21 –25.

[81] K. Takatani. “Effects of Electromagnetic Brake and Meniscus Electromagnetic Stirrer on Transient Molten Steel Flow at Meniscus in a Continuous Casting Mold”. In: *ISIJ Int.* 43 (2003), pp. 915 –922.

[82] K. Takatani. “Mathematical modeling of incompressible MHD flows with free surface”. In: *ISIJ Int.* 47 (2007), pp. 545 –551.

[83] K. Timmel et al. “Experimental Investigation of the Flow in a Continuous-Casting Mold under the Influence of a Transverse, Direct Current Magnetic Field”. In: *Metall. Mater. Trans. B* 42B (2011), pp. 68 –80.

[84] K. Timmel et al. “Experimental Modeling of the Continuous Casting Process of Steel Using Low Melting Point Metal Alloys—the LIMMCAST Program”. In: *ISIJ Int.* 50 (2010), pp. 1134 –1141.

[85] A. Tomiyama et al. “Effects of Eötvös number and dimensionless liquid volumetric flux on lateral motion of a bubble in a laminar duct flow.” In: *Advances in Multiphase Flow. Elsevier, Amsterdam.* 1995.

[86] G.B. Wallis. “A simplified one-dimensional representation of two-component vertical fow and its application to batch sedimentation”. In: *Symposium on the interaction between yuids and particles. Institute of Chemical Engineers, London.* 20-22 June, 1962.

[87] Y. Wang and L. Zhang. “Fluid Flow-Related Transport Phenomena in Steel Slab Continuous Casting Strands under Electromagnetic Brake”. In: *Metall. Mater. Trans. B* 42B (2011), pp. 1319 –1351.

[88] R.M. Wellek, A.K. Agrawal, and A.H.P Skelland. “Shapes of liquid drops moving in liquid media”. In: *AIChE Journal* 12 (1966), pp. 854 –860.

[89] O. Widlund, S. Zahrai, and F.H. Bark. “Development of a Reynolds stress closure for modeling of homogeneous MHD turbulence”. In: *Phys. Fluids* 10 (1998), pp. 1987 –1996.

[90] D.C. Wilcox. *Turbulence Modeling for CFD.* Anaheim: DCW Industries, 1998.

[91] D.F. Wu and S.S. Cheng. “Effect of Sen Design on Surface Fluctuation and Solidifying Shell in Slab Mold and Its Optimization”. In: *Acta Metallurgica Sinica (English Letters)* 21 (2008), pp. 341 –350.

[92] S. Wu, J. Zhang, and Z. Li. “Mathematic Model of SEN Clogging During Continuous Casting of Steel”. In: *Journal of Iron and Steel Research, International* 17 (2010), pp. 6 –9.

[93] C. Zhang, S. Eckert, and G. Gerbeth. “Experimental study of a single bubble motion in a liquid metal column exposed to a DC magnetic field”. In: *Int. J. Multiphase Flow* 31 (2005), pp. 824 –842.

[94] C. Zhang, S. Eckert, and G. Gerbeth. “The flow structure of a bubble-driven liquid-metal jet in a horizontal magnetic field”. In: *J. Fluid Mech.* 575 (2007), pp. 57 –82.

[95] C. Zhang et al. “Modification of Bubble-driven Liquid Metal Flows under the Influence of a DC Magnetic Field”. In: *ISIJ Int.* 47 (2007), pp. 795 –801.

[96] L. Zhang et al. “Investigation of Fluid Flow and Steel Cleanliness in the Continuous Casting Strand”. In: *Metall. Mater. Trans. B* 38B (2007), pp. 63 –83.

[97] W. Zhang et al. “Effect of the depth of the submerged entry nozzle in the mold on heat, flow and solution transport in double-stream-pouring continuous casting”. In: *Journal of Materials Processing Technology* 209 (2009), pp. 5536 –5544.

[98] I. Zun. “The transverse migration of bubbles influenced by walls in vertical bubbly flow”. In: *Int. J. Multiphase Flow* 6 (1980), pp. 583 –588.